Tissue growth mechanics that shape plant organs

植物器官を形作る組織成長力学

Fujiwara, Motohiro

Laboratory of Theoretical Biology, Department of Biological Sciences,
Graduate School of Science, Osaka University

大阪大学大学院理学研究科　生物科学専攻　理論生物学研究室
藤原基洋

Contents

Abstract

多細胞生物の器官は個体間で同じ形を示す。器官の形は構成する組織の成長で決まる。植物は、細胞壁により細胞の隣接関係が固定され組織の流動性が低いので、細胞分裂や細胞伸長の方向と位置を制御して器官を形作る。実際に、細胞分裂の方向や位置が乱れた変異体では、根の形も崩れる。その細胞の分裂や伸長の方向と位置を制御する仕組みとして細胞にはたらく力学が注目されている。先行研究では、茎頂分裂組織において力の方向と細胞分裂や伸長の方向が対応することが示された。ただし、力のはたらきは細胞レベルの局所的な理解に限定されている。したがって、細胞の分裂や伸長による組織成長が、器官レベルでどのような力を働かせ器官を形作るのか理解は不十分である。この一因は、生体実験で器官レベルの力の測定が難しいことにある。そこで、私は現実の組織成長に則して器官の形作りを再現できる力学的な数理モデルを構築した。この数理モデルを用いることで、器官を形作る組織成長の規則とそこではたらく力を予測することができた。私の予測は実験との共同研究により定量的に検証された。

１つ目は根の先端形状の研究である(図 A)。根の先端は細胞分裂が活発に起こる根端分裂組織を含み、ドーム形状を示す。まず定量解析により、シロイヌナズナの主根と側根のドーム形状は、サイズと形の個体間でのばらつきが小さく同じであることを確認した。私は、統計的モデル選択を用いて、このドーム形状がカテナリー曲線と一致することを発見した。カテナリー曲線は、アーチ橋など建築物に見られる力学的に安定な形状である。次に、根が、どのような組織成長によりカテナリー曲線へと形作られるのか予測するために、側根原基(図 A)の発生を観察した。側根原基の輪郭を定量した結果、輪郭は発生前期では個体間でばらつきが大きかったが、発生後期ではばらつきが小さくなりカテナリー曲線となることがわかった。カテナリー曲線を生成する力学モデルは、両端を固定して、一方向で均一な重力によって垂れた紐である。この力学モデルと整合する組織成長として、以下の 2 つの発生過程の細胞の分裂や伸長が対応すると仮説を立てた。(1) 根の中心で一様かつ一方向に並層分裂や異方伸長する、および、 (2) 根の両端で分裂しない。私は側根原基の発生を模した数理モデルを構築し、これら 2 つの組織成長を導入することで、カテナリー形状の根が形成されることを示した。この時、カテナリー曲線を生成する一方向で均一な力が原基の表面全体にはたらいていた。一方で、これら 2 つの組織成長の異常をそれぞれ導入すると、ドーム形状が崩れることを示した。この数理モデルの予測は、分裂の領域が広がる *puchi* 変異体と分裂の方向が乱れる *aurora* 変異体を用いた遺伝子実験により実際にドーム形状が崩れることが検証された。これらの結果か

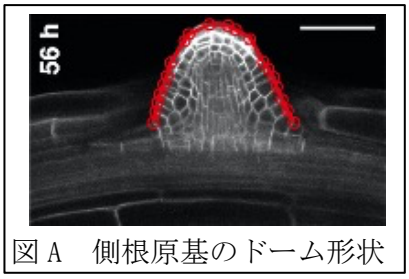

図 A　側根原基のドーム形状

ら、根の中心で一様かつ一方向に分裂して伸長する、および、根の両端で分裂しない、という２つの組織成長が、根をカテナリー曲線へと形作ることを明らかにした。

２つ目の根の維管束組織の研究である。シロイヌナズナの根の維管束は、中央一列に導管となる木部細胞が、端の上下に篩管となる篩部細胞が、その間に前形成層細胞があり上下対称性を示す(図 B)。木部と前形成層の成す組織境界周りでは、細胞形状と配置が境界に偏って並んで境界が滑らかになる(図 B)。細胞の配置換えが無い植物組織において、細胞種間で滑らかな境界を形成する組織成長の規則は理解されていない。野生型では、細胞分裂が滑らかな境界に対して上下対称で離れた篩部細胞周辺で局所的に起きる。まず、私は維管束成長を模して数理モデルを構築し、この分裂を導入することで滑らかな境界の形成を再現した。その時の細胞にかかる応力を数理モデルで計算すると、境界周辺では、篩部周りの離れた対称的な分裂パターンに対応した境界に向かう圧縮応力がかかることを予測した。予測したこの異方的な圧縮は、レーザーを用いて境界周辺の細胞を破壊する実験により実際に見られることが検証された。従って、篩部の境界遠方で局所的に分裂することで滑らかな境界形成を実現する規則であるという仮説が立つ。一方で、野生型に対し有意に境界が滑らかではない HAN 変異体では、非局所的な分裂が起きていた。HAN 変異体の非局所的な分裂を数理モデルに導入した結果、境界が滑らかではなくなった。そこで、HAN 変異体のどの場所での分裂異常が境界の滑らかさをなくしているのか、構築した数理モデルに非局所的な分裂を様々な場所で導入することで検証した。その結果、境界周辺での分裂により境界の滑らかさがなくなった。また、境界に対して対称な篩部細胞周りの分裂のうち片方のみに側方領域への広がりを導入し非対称にすると、境界の滑らかさがなくなった。この両方で、境界へ向かう圧縮応力が乱れていることを確認した。このことから、境界から離れて局在し対称な場所での分裂が滑らかな境界形成に必要な規則であることを予測し検証した。これらの結果から、遺伝子発現により制御された分裂パターンが、そのパターンと対応した異方的な圧縮応力を介して、境界を上下対称的に滑らかにすることを明らかにした。

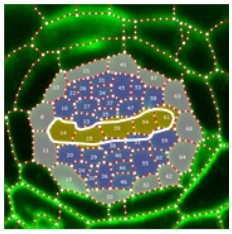

図 B　根の維管束の細胞配置(白線内が木部)

私は、植物器官の形作りの定量的な数理モデリングを通じて、器官を形作る組織成長の規則とそこではたらく力を予測し、実験で実証できる研究方法を確立した。

Publication List

1. *Fujiwara M., *Goh T., *Tsugawa S., Nakajima K., Fukaki H., and Fujimoto K., “Tissue growth constrains root organ outlines into scalable shape” Development (2021) 148, dev196253. doi:10.1242/dev.196253 (*Equal contribution)

I am preparing a submission of the contents in section 3 as follows:

2. *Fujiwara M., *Miyashima S., Matsushita K., Nakajima K., and Fujimoto K., “Distally localized and symmetric proliferation smoothens plant vascular tissue boundary” (*Equal contribution)

1. General Introduction

1.1. Tissue growth is indispensable for animal and plant organogenesis

Multicellular organs within the same species show the same shape with less individual variation. The organs consist of tissues of internal structures, and the tissue growth forms the organ. The fundamental challenge of developmental biology is to understand how tissue growth by the behavior of individual cells achieves the reproducibility of organ shape.

Tissue growth is characteristic of each organogenesis. For example, in the wing epithelium of fruit fly, a differential adhesion at the cell-cell interface positionally biases cell rearrangement, resulting in forming a straight boundary between cell populations (Dahmann et al., 2011). Such cell rearrangement has also been observed in spider embryogenesis during active cell division (Hemmi et al., 2018). In sea urchin gastrulation, cell contraction at the apical side promotes bending of the epithelium tissue that allows cells to inward into the embryo (Keller et al., 2003). Therefore, the local and fluid cell behaviors, such as cell contraction and rearrangement, primarily regulate tissue growth to determine animal organ shape (Dahmann et al., 2011; Lecuit et al., 2007).

On the other hand, plant tissue is less fluid where the cell wall prevents cell rearrangement, thereby fixing neighboring cell relations. Cell division and elongation are the main processes of plant tissue growth. For example, in shoot apical meristem, the position and direction of cell division form a new leaf primordium (Hamant et al., 2008). In leaf primordia, cell division at the proximal side, followed by cell elongation, results in leaf elongation (Kuchen et al., 2012). In roots, the direction of division and elongation at the root tip is strictly controlled to determine the cell layer (Wilson et al., 2013). These results suggest that control of the direction and position of cell division and elongation are indispensable for forming organs in less fluid plant tissue. The genetic mechanisms such as phytohormone-dependent controlling the direction and position of cell division and elongation have been extensively investigated. At the root tip, the auxin distribution causes the cell elongation and division that form the lateral root primordium (Péret et al., 2009). The orientation of the cortical microtubules at the surface of the plant cells also controls the direction of cell elongation. Therefore, reproducible plant organogenesis requires the precise control of cell division and elongation of tissue growth.

1.2. Cell behavior and the contribution of force for organogenesis

Cell shape and deformation are governed by cell mechanics, which explains how forces control the cell division and elongation of tissue growth. It is essential to understand what forces contribute to the regulation of tissue growth by molecular mechanisms to understand organ formation. The relationship between forces and cell behavior regulation has attracted attention (Kennaway et al., 2011; Bassel et al., 2014). In recent years, it has become possible to measure local cell deformation and estimate mechanical parameters (e.g., cell junction and surface tension, tissue stress) of tissue (Sugimura et al., 2016). Cell division and elongation cause stress around cells during tissue growth. The stress regulates the direction of cell division and elongation (Trinh et al., 2021). Molecular mechanisms linking force and cell growth include auxin efflux carrier PIN, which controls the flow of phytohormones auxin. Auxin flow affected the orientation of the cortical microtubules. This mechanism regulates cell division and elongation by controlling the cell wall extensibility (Heisler et al., 2010). The importance of forces acting on cells in the morphogenesis of plant organs is now well understood (Trinh et al., 2021). However, our understanding of the forces is limited to localized processes because it is difficult to measure the actual mechanics throughout the organ. Moreover, the forces that determine the shape of organs are limitedly understood. Therefore, mathematical models that recapitulate the mechanical tissue processes are useful to predict the forces loaded on organs.

1.3. Methods for predicting and verifying force loaded on organs

The models for the tissue mechanics have been developed to directly link cell behavior to tissue deformation and represent the forces from tissue growth (Farhadifar et al., 2007; Honda, 1983). The vertex model is one of the most useful models to understand how individual cell dynamics drive tissue deformation (Aliee et al., 2012; Hamant et al., 2008), and predict the underlying mechanical properties such as the differential adhesion and the mechanical stress loaded on each cell (Lee and Morishita, 2017). The predicted stress loaded on cells can be verified by using invasive experiments such as laser ablation and noninvasive ones such as atomic force microscopy (Sugimura et al., 2016). In laser ablation, the mechanical pressure can be indirectly measured by the deformation of the surrounding cells in response to the ablation for a target cell. However, the mechanical understanding has been limited to cell-level behavior and its effects on small cell populations, so it is lacking to understand the forces of tissue growth at the organ level. Therefore, I aimed to develop a more realistic mathematical model by introducing the quantitative data of developmental processes measured *in vivo* to estimate the forces of tissue growth.

1.4. Overview of plant root

Plant roots are essential organs for plant growth, taking nutrients and water from the outside and supporting the above-ground plant part. The root tip comprises root apical meristem (RAM) and root cap (Wilson et al., 2013). The RAM has a group of root stem cells with proliferating activity. Although a fraction of cells within RAM, called the quiescent centers, does not divide, these cells serve as a scaffold for the stem cells by signaling them to maintain their proliferative potential while preventing the surrounding stem cells from differentiation. The direction of cell division in the RAM is regulated, forming a multi-layered tissue structure. The root cap covers the RAM and is indispensable to protect RAM from the surrounding environment, such as soil. The vascular tissue at the inside of the root contains the conducting tissue that carries water and nutrients (Esau 1965). I focus on the shape of the root tip outlines and the vascular tissue boundary as the target tissue growth system. The detailed background of each is explained in Chapters 2 and 3.

1.5. The aim of my thesis

The present thesis aims to identify the tissue growth rule and mechanical forces that shape plant organs. In Chapter 2, I study the root tip shape. In Chapter 3, I study the root vascular tissue boundary. In both Chapters, I constructed a mathematical model by incorporating tissue growth measured *in vivo* and try to reproduce plant organ shapes quantitatively. Using the mathematical model, I predict the primary tissue growth and forces that determine the root shape. I further establish the research method combining quantitative analysis and mathematical modeling with experimental verification *in vivo*. The established research method allows me to identify the tissue growth and the mechanical forces for forming the organ shapes.

2. Tissue growth constrains root organ outlines into an isometrically scalable shape

Some figures in this thesis were obtained in collaboration with my colleagues, T. Goh and S. Tsugawa. I clarified their contribution in each caption.

2.1. Abstract

Organ morphologies are diverse but also conserved under shared developmental constraints among species. Any geometrical similarity in the shape behind diversity and the underlying developmental constraints remain unclear. Plant root tip outlines commonly exhibit a dome shape, likely to perform physiological functions, despite the diversity in size and cellular organization among distinct root classes and/or species. I carried out morphometric analysis of primary roots of ten angiosperm species and lateral roots (LRs) of *Arabidopsis* and found that each root outline is isometrically scaled onto a parameter-free catenary curve, a stable structure adopted for arch bridges. Using the physical model for bridges, I analogized that localized and spatially uniform occurrence of oriented cell division and expansion force the LR primordia (LRP) tip to form a catenary curve. These growth rules for the catenary were verified by tissue growth simulation of developing LRP development based on time-lapse imaging. Consistently, LRP outlines of mutants compromised in these rules were found to deviate from catenary curves. Our analyses demonstrate that physics-inspired growth rules constrain plant root tips to form isometrically scalable catenary curves.

2.2. Introduction

Plant root

Plant and animal organ forms (i.e. outline morphologies of organs) are defined by size and shape. Organ forms became diverse across species as a consequence of adaptation to various physiological and environmental conditions during evolutionary radiation (Darwin, 1859; Le Roy et al., 2019; Maugarny-Cales and Laufs, 2018; Salcedo et al., 2019; Tsukaya, 2018). However, organ forms share a conservative feature in each organ type (e.g. roots and leaves in plants, and beaks and wings in animals) (Houle et al., 2017; Wang and Clarke, 2015). As a typical example of similarity behind the diversity, organ outlines can collapse onto a single common shape across species by rescaling of individual size (e.g., cannon-bone of ox, sheep, and giraffe (Thompson, 1917); beak of songbirds (Abzhanov, 2017; Campas et al., 2010)). The scaling of songbird beaks is imposed by developmental programs shared among species (Abzhanov, 2017; Campas et al.,

2010; Fritz et al., 2014). While scaling of organ size (e.g. proportionality and allometry to body size) has been extensively studied (Niklas, 1994; Schmidt-Nielsen, 1984), quantitative assessments on the shape scaling and the underlying developmental constraints have been reported in limited cases as mentioned above.

The outline of plant root tips commonly exhibits a domed shape in angiosperms, despite diversities in size and cellular organization among species and/or in developmental processes among root classes (Clowes, 2000; Hamamoto et al., 2006; Heimsch and Seago Jr, 2008). The root tip plays a pivotal role in root growth by executing a wide variety of functions such as penetration, anchorage, gravity perception, and nutrient and water uptake (Eshel and Beeckman, 2013). The root tip mainly consists of the root apical meristem (RAM) and the surrounding root cap (Fig. S2.1A-C) (Kumpf and Nowack, 2015; Petricka et al., 2012). RAM organization is diverse across species, as exemplified by open and closed meristem (Clowes, 2000; Heimsch and Seago Jr, 2008), and the number of cell files and layers (Di Ruocco et al., 2018; Hamamoto et al., 2006; Mellor et al., 2019). Even within a given individual, there are several classes of developmentally distinct roots, such as primary roots (PRs), lateral roots (LRs) and adventitious roots (ARs). PRs are established during embryogenesis (Petricka et al., 2012; ten Hove et al., 2015), whereas LRs and ARs are post-embryonically initiated in existing roots and specific parts of the shoot, respectively (Fig. 2.1A) (Lavenus et al., 2013). While internal morphologies of PRs and LRs have been extensively studied at the level of cellular organization and shown to be largely conserved (Petricka et al., 2012), how their outline morphologies have converged into a seemingly similar dome shape and whether any mechanical impositions play a role to stabilize fixed root tip shapes, if any, remain unknown.

Lateral root development

LR primordia (LRP) development is a suitable model system to investigate the nature of tissue growth that governs the formation and maintenance of the root tip outlines (Goh et al., 2016; von Wangenheim et al., 2016). In *Arabidopsis thaliana* (Arabidopsis), LRP originates from the LR founder cells that are specified in the xylem pole pericycle in the differentiation zone (Lavenus et al., 2013; Norman et al., 2013). LR founder cells undergo multiple rounds of coordinated cell divisions and expansion to produce a dome-shaped LRP and emerges from the overlaying tissues to extend into the soil (Goh et al., 2016; von Wangenheim et al., 2016). Several factors, such as cell division rules arising from cell geometry and mechanical constraints by the overlaying tissues, have been reported to affect the LRP outline (Lucas et al., 2013; Vermeer et al., 2014; von Wangenheim et al., 2016).

Here, I performed morphometric analysis of the PR and LR tip outlines and revealed that they are highly reproducible in both size and shape within a given species and regardless of the root class. Statistical analyses showed that the outlines of different root classes and species were isometrically scalable (geometrically similar); by scaling the width and the height of root tips with an identical rate, the outlines commonly converge to a unique catenary curve. Simulations incorporating cell division and expansion rules drawn from time-lapse observation of LRP development identified tissue growth constraints as a major determinant for the geometry and mechanics of the isometrically-scalable root tip shape. The developmental constraints identified in this study govern the scalable diversity of root organ morphologies.

2.3. Materials and Methods

Plant materials and growth conditions

We used accession Col-0 as a wild type for analysis of root tip shape in *Arabidopsis*. For analysis of multiple species, I selected one monocot (*Allium fistulosum,* Welsh onion), three rosids (*Cucumis sativus,* cucumber; *Viola mandshurica,* violet; *Arabidopsis*), one caryophyllales (*Dianthus superbus,* pink), and five asterids (*Primula polyantha,* primrose; *Cosmos bipinnatus,* common cosmos; *Daucus carota,* carrot; *Antirrhinum majus,* snapdragon; *Nemophila menziesii,* nemophila). All seeds except for *Arabidopsis* were obtained commercially (Sakata seed corporation, Yokohama, Japan). *puchi-1* (Hirota et al., 2007), *aur1-2* (SALK_031697) and *aur2-2* (GK403B02; (Van Damme et al., 2011)) have been previously described. *35S::LTI6b-GFP* line (CS84762) was obtained from the *Arabidopsis* Biological Resource Center. Seeds were surface sterilized and sown on 1× MS medium solidified with 0.4% gellan gum containing 1% (w/v) sucrose or on *Arabidopsis* growth medium (Okada and Shimura, 1992) supplemented with 1% (w/v) sucrose and 1% (w/v) agar.

Imaging and image processing

For LR analysis, seven-day-old seedlings were fixed with 4% (w/v) paraformaldehyde for 30 min at room temperature, washed twice with phosphate-buffered saline (PBS), and then cleared with ClearSee solution including 0.2% (v/v) SCRI Renaissance 2200 (SR2200) for cell-wall staining (Kurihara et al., 2015; Musielak et al., 2015). Images were obtained with a Nikon C2 confocal microscope, with a 405-nm laser line for excitation of SR2200. For PR analysis, seedlings were grown for several days until the first LR appeared and then observed by a confocal microscope after staining with propidium iodide. Images were obtained with a Zeiss LSM710 confocal

microscope. Image segmentation was performed to detect shape and position of each cell using the Fiji plugin Tissue Analyzer (Aigouy et al., 2010).

For time-lapse observation of LRP development, 4-day-old seedlings (*35S::LTI6b-GFP*) grown vertically were transferred into a coverglass-bottom chamber (LabTek, Thermofisher) placed with a block of solid medium. Images of an identical primordium were obtained 6, 24, 30, 48 and 54 hours after gravistimulation with a Nikon C2 confocal microscope and processed with ImageJ software.

Determination of root tip outlines and unification of the coordinate system

We analyzed the vertical sections of the angiosperm PR tips (Figs. 2.1A, S2.1A-C and S2.5A) and *Arabidopsis* LR tips at different developmental stages (Fig. 2.1A). For both the PR and LR tips, we determined the outline from the positions of the cell junctions along the dome surface (Fig. S2.1D, E). For the PRs, we analyzed the region from root tip to the boundary between meristem and elongation zone except for sloughing root cap layer (red dotted box in Fig. S2.1D). The x- and y-axes were set parallel to the upper boundary at the opposite side of the tip and the proximal-distal axis of the dome, respectively. In order to compare different root tip outlines, it is necessary to objectively unify the coordinate system with setting the peak of the tip at origin. Therefore, we define the origin of the coordinate system by the following three steps (see also Fig. S2.1F): (1) the junction points on the outline were duplicated and turned by 180 degree (π radian); (2) the duplicated positions were translated to satisfy that the maximum y of the original one was equal to the minimum y of the duplicated one; (3) the origin of x- and y-coordinates were determined as the mean of x of all points and the minimal y of the original points, respectively. Given this unified coordinate system, the dome area and width at a height from the root tip are comparable (Fig. S2.1G).

Radial Fourier series expansion

The radial Fourier series expansion enables to characterize the shape of a closed curve using the radial information of the polar coordinate system (r_i, θ_i)derived from the cartesian coordinate system (x_i, y_i) (Hong et al., 2016). The closed curve of root tip outlines was prepared by the above-mentioned methods, (1) duplication and (2) translation, without loss of generality. In this set up, i denotes the label of all junction points including the duplicated ones (Fig. S2.1F) up to the total number of duplicated junction points ($i = 1, 2, \cdots, M;\ 0 \leq \theta_i \leq 2\pi$). The radial Fourier series expansion $r(\alpha)$ can be decomposed as,

$$r(\alpha) = r_0 + \sum_{n=1}^{N_f} [a_n \cos(2\pi n\alpha) + b_n \sin(2\pi n\alpha)]$$

$$= r_0 + \sum_{n=1}^{N_f} [c_n \cos(n(2\pi\alpha + \Phi_n))] \quad \text{(Eqn. 2.1)},$$

$$r_0 = \frac{T}{2\pi}\int_0^{2\pi} r(\alpha)\, d\alpha \quad \text{(Eqn. 2.2)},$$

$$a_n = \frac{T}{2n^2\pi^2}\sum_{i=1}^{M}\frac{\Delta r_i}{\Delta t_i}\left(\cos\frac{2n\pi t_{i+1}}{T} - \cos\frac{2n\pi t_i}{T}\right) \quad \text{(Eqn. 2.3)},$$

$$b_n = \frac{T}{2n^2\pi^2}\sum_{i=1}^{M}\frac{\Delta r_i}{\Delta t_i}\left(\sin\frac{2n\pi t_{i+1}}{T} - \sin\frac{2n\pi t_i}{T}\right) \quad \text{(Eqn. 2.4)},$$

where $\alpha(0 \le \alpha \le 1)$ denotes a continuous normalized perimeter along the outline. Φ_n and c_n denote the angular phase and the amplitude, respectively, of the *n*-th Fourier mode. Δt_i denotes the normalized perimeter at the point (r_i, θ_i). Δr_i denotes the radial distance between two successive junction points $N_f = 200$ in this study. In the explicit form, α is equal to t_i/T with the total perimeter of the outline *T* and Δt_i and Δr_i can be defined as,

$$\Delta t_i = t_{i+1} - t_i\,,\ t_i = \sum_{j=1}^{i}\sqrt{(x_{j+1} - x_j)^2 + (y_{j+1} - y_j)^2} \quad \text{(Eqn. 2.5)},$$

$$\Delta r_i = r_{i+1} - r_i \quad \text{(Eqn. 2.6)}.$$

The shape is characterized by normalized radial Fourier series expansion

$$r_{norm}(\alpha) = \frac{r(\alpha)}{r_0} = 1 + \sum_{n=1}^{N_f}\left[\frac{c_n}{r_0}\cos(n(2\pi\alpha + \Phi_n))\right] \quad \text{(Eqn. 2.7)},$$

to eliminate the influence of the size on the shape. For the normalized radial Fourier expansion $r_{norm}^{j}(\alpha)$ of the sample *j* ($j = 1,2,\cdots,K$) where *K* stands for the total number of samples, the sample average with continuous outline can be calculated as

$$\underline{r}_{norm}(\alpha) = \frac{1}{K}\sum_{j=1}^{K} {r_{norm}}^{j}(\alpha) \quad \text{(Eqn. 2.8)}.$$

An indicator of shape reproducibility $S_2^{1/2}$, representing normalized error of shape, can be evaluated by the root mean squared deviation from sample-averaged normalized shape

$$S_2^{1/2} = \sqrt{\frac{1}{2\pi}\int_0^{2\pi}\left(r_{norm}(\alpha) - \underline{r}_{norm}(\alpha)\right)^2 d\alpha} \quad \text{(Eqn. 2.9)},$$

where $S_2^{1/2} = \sqrt{S_2}$ as described previously with regards to sepal shape (Hervieux et al., 2017; Hong et al., 2016).

Statistical analysis of the dome shape

I fitted the outline of the dome to the following five functions: parabola ($y = a_1x^2$), catenary ($y = a_2\cosh(x/a_2) - a_2$), ellipse ($y = b_3 - b_3\sqrt{1 - x^2/{a_3}^2}$), hyperbola ($y = -b_4 + b_4\sqrt{1 + x^2/{a_4}^2}$), and cosine ($y = -a_5\cos(b_5x) + a_5$), where a_i (i = 1, 2, 3, 4, 5) and b_i (i = 3,

4, 5) are fitting parameters. The hyperbola has a common mathematical nature (i.e. conic section) to parabola and ellipse; catenary and cosine are mechanically stable functions under unidirectional force (Block et al., 2006; Lockwood, 1961) (Fig. 2.2B) and the Euler buckling (Timoshenko and Gere, 1961), respectively. Using these functions, I applied the non-linear least-squares (NLS) method (Moré, 1978) to each dataset of normalized cell junction positions on the outlines of multiple LRP samples at each developmental stage and PR samples from each species. I evaluated the positional variation of the dome outline among samples on the basis of the sample standard error (SSE) of the y-coordinate (height) from these functions defined by

$$\text{SSE} = \sqrt{\Sigma(y_{data} - y_{function})^2/(n-1)} \qquad \text{(Eqn. 2.10)},$$

and the Akaike-Information Criterion (AIC) defined by

$$\text{AIC} = 2k - 2\ln(L) \qquad \text{(Eqn. 2.11)},$$

which is the number of parameters in the model k (one for parabola and catenary, and two for the other three functions) minus the natural logarithm of the maximum likelihood L (Akaike, 1974; Burnham et al., 2002; Sakamoto et al., 1986). The AIC is one of the most popular and statistically rigorous criteria, since the AIC of the best-fit function takes the minimum value. I computed ΔAIC defined as the difference in AIC between a given model function and the lowest AIC model function. Thus, the fitting function for which ΔAIC = 0.0 is the best model, whereas models with larger ΔAIC values are not as good. Generally, models with ΔAIC < 2.0 have the potential to be the best model, and those with ΔAIC < 7.0 cannot be easily rejected (Burnham et al., 2002). I performed NLS-fitting and AIC calculation with the R interface using the minpack.lm package (Elzhov et al., 2015). S. Tsugawa performed the cross-validation test which is one of the model validation techniques, providing us how robustly the model will predict the data set without overfitting or selection bias (Hong et al., 2016). In the test, a part of the data points (referred to as the testing set) is validated based on the rest of the data points (referred to as the training set). In our case, the training set was 99% of the junction points which were randomly selected, whereas the testing set was the remaining 1%. The model validation was evaluated by the mean squared error (MSE) between the fitting function from the training set and the testing set. Applying this process to different training set i with different random seeds for N times, the final validation is performed by

$$\text{the averaged MSE} = \sum_{i=1}^{N} \frac{mse_i}{N} \qquad \text{(Eqn. 2.12)}.$$

Formulation of tissue-mechanical simulations

The cell vertex model is useful for simulating the mechanical deformation of cells in tissues based on the forces acting on each cell, in which the cell configurations are described as polygons that have vertices that form cell junction subjected to mechanical force (Farhadifar et al., 2007; Honda, 1983). Cells change their shape based on the force balance represented as mechanical energy E with dimensionless time and mass. The model is represented here by the ordinary differential equations of the position vector $\vec{r}$ of each vertex:

$$\frac{d\vec{r}}{dt} = F_{area\ elasticity} + F_{tension} = -\frac{dE}{d\vec{r}} \quad \text{(Eqn. 2.13)},$$

$$E = \sum_n c(A_n - A_0)^2 + \sum_{ij} \beta_{ij} L_{ij} \quad \text{(Eqn. 2.14)}.$$

The area elasticity $F_{area\ elasticity}$ is exerted on a vertex i by the cell face n to which the vertex i belongs, while the area of cell A_n approaches the target area of A_0 with normalized strength of the elasticity. The tension $F_{tension}$ is exerted on a vertex i by the connecting edges between vertices i and j, where $F_{tension}$ increases as the edge length between vertices i and j (L_{ij}) increases, depending on the cell-wall extensibility β_{ij}. For all cells, we set c=1 μm^{-2}, β_{ij} = 0.002 μm for horizontal edges, and β_{ij} = 0.004 μm for vertical edges, which reproduced the average cell area and cell aspect ratio of *Arabidopsis* wild-type cells in LRP at developmental stage IV (Goh et al., 2016). In addition, plant cells undergo plastic deformation by the irreversible cell growth, which has been formulated by multiplication of the excess turgor pressure over yield stress and the cell wall extensibility of cell edge (Lockhart, 1965). In the present model, the plastic deformation was formulated by the irreversible increase of the target area of cells, as described in detail below, instead of the edge length in the Lockhart model (Lockhart, 1965). We integrated the cell vertex model numerically using the Euler method and confirmed that the obtained results were not greatly influenced by the choice of the temporal discretization size dt.

Cell division and expansion in simulations

For the initial condition of the vertex model, 20 cells were arranged horizontally (only 8 to 12 cells at the central region shown in Figs. 2.4, 2.5, S2.7, S2.8); the four cells (dark and light blue in Fig. 2.4E) among the eight at the center subsequently divided, but the others did not divide (white in Fig. 2.4E) during the wild-type simulation. For the boundary conditions, the vertices at the basal end of the tissue could be displaced horizontally but not vertically (i.e. fixed at y = 0) to mimic the high stiffness of the adjacent parental xylem cells, whereas those at the apical end were displaceable in any direction. Below 40 μm of the LRP height, those at the apical end are adjacent to an imaginal cell to mimic the overlaying parental cells with vertical thickness 36 μm (A_0 = 36

μm × 20 cells × 14 μm/cell = 10,080 μm^2; grey in Figs. 2.4, 2.5, S2.8). All the vertices at both ends in the horizontal direction were fixed (at x = -140 μm and x = 140 μm, respectively).

During the stages with one to four layers, the timing and orientation (periclinal/anticlinal) of cell divisions were set following the typical division rules in wild-type LRP (Goh et al., 2016; von Wangenheim et al., 2016). First, two central cells (dark blue in Fig. 2.4E) simultaneously underwent periclinal division. Second, these four central cells underwent anticlinal division while two flanking cells (light blue cells, Fig. 2.4E) immediately outside those four cells simultaneously underwent periclinal division. Third, the eight central cells (dark blue in Fig. 2.4E) synchronously underwent two periclinal divisions, although cells at the outer layer divided a little earlier than cells at the inner layer of *Arabidopsis* LRP (Goh et al., 2016; von Wangenheim et al., 2016). The cell division plane was assumed to pass through the geometric center of the dividing cell with a small rotational variation in the periclinal/anticlinal direction, which followed the Gaussian distribution with the s.d. of 0.1 degree. Cells (dark and light blue in Fig. 2.4E) followed linear growth in wild-type LRP (Goh et al., 2016); immediately after the previous division event, the target area A_0 was initially set as an average of 56 μm^2 in cells, and temporally linearly increases with $\frac{dA_0}{dt} = 7.2\mu\text{m}^2/\text{hour}$. The cell division occurred when the cell area A_n (Eqn. 2.14) became twice that of the initial target area, with a variation following a Gaussian distribution with an s.d. of 5.6 μm^2. New target area A_0 was set to half of A_n before the division event. After the four layers stage, cells (dark blue in Fig. 2.4E) were additionally divided until the cell numbers identical to wild-type stage VII LRP (Goh et al., 2016; von Wangenheim et al., 2016), where cell expansion and division cycle were the same as the above, whereas the division plane was set to the short axis of the mother cell with a rotational variation following a Gaussian distribution with an s.d. of 0.1 degree.

To recapitulate the anisotropic growth of provascular bundle cells (Fig. 2.4A, D, right panel), we introduced rapid anisotropic expansion of the two central basal cells (magenta in Fig. 2.4E) by linearly increasing A_0 with $\frac{dA_0}{dt} = 21.6\ \mu\text{m}^2/\text{hour}$ and the same division cycle as the above, and decreasing β_{ij} of the vertical cell edge (β_{ij} = 0.002 μm at the end of four layers to β_{ij} = 0.0005 μm at the end of provascular cell expansion) over time, while keeping β_{ij} = 0.002 μm of the horizontal cell edge.

2.4. Results

Reproducible size and shape of root tip dome in *Arabidopsis*

PR and LR tips of Arabidopsis share an apparently common dome shape with a nearly perfect rotational symmetry (Figs. 2.1A, S2.1A). In order to quantitatively evaluate the shape of Arabidopsis root tips, we captured longitudinal optical sections of the tips of PRs, mature LRs (longer than 5 mm as measured from the primary root surface), and young emerged LRs (less than 200 μm as measured above; Fig. 2.1A; Materials and Methods). Root tip outlines were delineated semi-automatically by marking the positions of cell-cell junctions along the outer surface of the outermost cell layer (red points in the right panels of each root class in Fig. 2.1A), and then projected to the spatial coordinate (x, y) (Fig. S2.1D-G; Materials and Methods). The size and shape of the extracted outlines were apparently reproducible within each root class (Fig. 2.1B). First, we quantified the size reproducibility based on the coefficient of variation (CV, i.e., the standard deviation divided by the mean). The CV was within a range of a few percent for LRs (4–7% for dome area, Fig. 2.1C; and 3–6% for dome width, Figs. S2.1G and S2.2), whereas slightly larger for PRs (7–4% for dome area, Fig. 2.1C; 5–11% for dome width, Fig. S2.2). We then assessed shape reproducibility irrespective of the size by normalizing the root tip outlines (Hervieux et al., 2017; Hong et al., 2016). An indicator of shape reproducibility, which was represented by the root mean squared error between the normalized outlines of individual root tips and their average (Eqn. 2.9 in Materials and Methods; Fig. 2.1D), was found within a range of 1–3% (Fig. 2.1E). Taken together, our analysis indicated that Arabidopsis PR and LR tips are highly reproducible in both size and shape.

Tip dome outlines of PRs and LRs fit to a catenary curve and its essentially-equivalent curve, a catenary-closest ellipse

The reproducibility of root outline shapes (Fig. 2.1) prompted us to examine which mathematical function accurately represents the dome shape. We assessed which of the five representative curves, an ellipse, parabola, hyperbola, cosine, or catenary, best fits the root tip outlines (Fig. 2.2A; Materials and Methods for statistical analysis). Although the outlines of RAM and shoot apical meristem have been previously fitted to ellipse (Colombi et al., 2017) and to parabola (Leiboff et al., 2016; Leiboff et al., 2015), respectively, whether these outlines could better fit to other dome-shaped functions with a common mathematical nature (hyperbola) or a mechanical stability (cosine (Timoshenko and Gere, 1961) and catenary (Block et al., 2006; Lockwood, 1961) (Fig. 2.2B)) has not been investigated. The ellipse and catenary functions were found to fit equally well to the outline data of PRs, emerged LRs, and mature LRs of Arabidopsis, and fit significantly

better than the other three functions (the sample standard error [SSE] in Fig. 2.2C left and Fig. S2.3 left; averaged mean squared error [MSE] of cross validation, Fig. 2.2C right and Fig. S2.3 right; the Akaike-information criterion in Fig. S2.3 middle). Interestingly, the fitted ellipse and catenary functions were found to superimpose each other within the range of the root tip width (Fig. 22.A). Indeed, this characteristic ellipse had the highest similarity to the catenary among any ellipses at a level that could be nearly identical in shape (Fig. S2.4A-J) so as to be hereafter referred to as catenary-closest ellipse. These indicate that catenary and catenary-closest ellipse are essentially equivalent functions best-fitting to the root tip outlines of both Arabidopsis PR and LR.

Isometric scaling unifies dome outlines of the root tips of diverse root classes and plant species into a single common shape

The catenary parameter a is the reciprocal of the curvature of the dome controlling its sharpness (Fig. 2.3A, left panels; $y = a\cosh(x/a) - a$), and works as a factor of the isometric scaling (i.e. geometric similarity); by scaling both x- and y-coordinates with catenary parameter a, catenary curves commonly converge to the parameter-free catenary function ($Y = \cosh(X) - 1$, $X = x/a$, $Y = y/a$; Fig. 2.3A, right panels). The catenary parameter a also works as the isometric scaling factor to the catenary-closest ellipse as well, since each fitted value of ellipse parameters ($a_{ellipse}$ and $b_{ellipse}$; $y = b_{ellipse}(1-(x/a_{ellipse})^2)^{0.5}$) were both proportional to that of catenary parameter a among Arabidopsis PR and LR samples (Fig. S2.4K, L). The isometric scalability of the fitted functions by catenary parameter a predicts that of the root tip outlines. Strikingly, the isometric scaling of each sample using its own fitted catenary parameter a (Fig. 2.3B) successfully normalized differences of the individual size among PR and LR samples (Fig. 2.3C, left panel), so that all root outlines commonly converged to the parameter-free catenary function (Fig. 3C, right panel). These results verified the isometrically scalable nature of Arabidopsis PR and LR.

To further examine the isometric scaling of dome-shaped outlines across diverse species, we analyzed the PRs of eight additional eudicot and one monocot species (Figs. 2.3B, D left panel and S2.5A). Regardless of their morphological diversity (i.e. size and aspect ratio of the dome, the number of ground-tissue layers, and the structure around the quiescent center such as the open or closed meristem; Fig. S2.5B, C) (Clowes, 2000; Heimsch and Seago Jr, 2008), the root tip outlines of all these species fitted to the catenary curve and the catenary-closest ellipse to a similar extent (averaged MSE in Fig. S2.6). The fitted value of catenary parameter a reflected the species-specific dome size (Figs. 2.3B and S2.4K, L). Moreover, the rescaled PR outlines by the fitted catenary parameter a converged universally to the parameter-free catenary curve (Fig. 2.3D, right

panel) as in Arabidopsis PRs and LRs. These results indicate that the dome outline diversity of various angiosperm PRs as well as Arabidopsis LRs universally emerge from the isometric scaling by the species- and root class-specific catenary parameter *a*.

Tissue growth rules underlie self-organized formation of the catenary-curved geometry in Arabidopsis LRs

The dome shape of LR emerges from a developmental process (Goh et al., 2016; Lucas et al., 2013; Vermeer et al., 2014; von Wangenheim et al., 2016). Both young emerged LRs and mature LRs had almost identical values of the catenary parameter *a* (Fig. 2.3B), suggesting that the formation of the isometrically scalable dome shape is completed before the LR emergence. We further found that the dome outlines fit well to a catenary curve consistently from early (LRP dome height $10 < h < 30$, stage II - V), late ($30 < h < 50$, stage VI - VII), and emerged LRP (dome height $50 < h$, emerged, Fig. 2.4A-C), judged by the same level of averaged MSE as those of emerged LRs (Figs. 2.4C and S2.3). The value of catenary parameter *a* of LRP decreased with developmental progression, and eventually reached those of emerged LRs (Fig. 2.4B).

In order to gain insights as to what developmental processes contribute to the formation of the isometrically scalable dome and its maintenance, it is useful to refer to a developmental model of catenary curve, i.e., a free-hanging chain stably forming with its own weight when its ends are supported (Fig. 2.2B, left panel) (Block et al., 2006; Lockwood, 1961), though, to our knowledge, a model for the catenary-closest ellipse has not been described so far. To this end, we performed tissue growth simulations of LRP development by focusing on the catenary-curved geometry.

We used the vertex model for mechanical deformation of cells (Materials and Methods; (Farhadifar et al., 2007; Hamant et al., 2008; Honda, 1983; Uyttewaal et al., 2012)) by incorporating tissue growth rules of LRP (i.e. the rate and orientation of cell division and expansion) obtained from the previously reported time-lapse imaging of wild-type LRP development (Fig. 2.4A, D, E; Materials and Methods) (Goh et al., 2016; von Wangenheim et al., 2016). Briefly, in the early phase where a four-layered primordium (stage I to IV) is formed, one anticlinal and three periclinal divisions occurred synchronously in the central region of a primordium (dark blue cells, Fig. 2.4D, E) and one periclinal division occurred in the flanking region (light blue cells, Fig. 2.4D, E), whereas no division occurred at the periphery of the primordium (white cells, Fig. 2.4D, E). In later phases, anisotropic cell expansion occurred locally at the central bottom cells (pro-vascular cells shown in purple, Fig. 2.4D, E), and the LRP subsequently emerged through the overlaying cells (Goh et al., 2016; von Wangenheim et al.,

2016). Importantly, simulations incorporating the tissue growth rules quantitatively reproduced the catenary-curved geometry of a growing LRP dome (Fig. 2.4E). Even in the absence of overlaying cells at the earlier stages, the catenary-curved dome develops in simulations (Fig. S2.7A), though the shape reproducibility was less pronounced than those produced in the simulations with overlaying cells (Fig. S2.7A-C). These results recapitulate the decrease of the catenary parameter *a* along the course of LRP development (Fig. 2.4B), with similar or even higher degree of fitness as compared with those observed *in vivo* (Fig. 2.4C).

Tissue growth rules of LRP account for the mechanics of a catenary curve formation in Arabidopsis

Catenary-curved hanging chains and bridges (Fig. 2.2B) are load-bearing structures which follow the mechanical equilibrium between gravity (i.e., vertical and uniform force distribution) and tangential tension on the chain (Fig. 2.4F-H) (Block et al., 2006; Lockwood, 1961). Geometrical similarity between catenary chains and LRP domes prompted us to examine whether tissue growth behaviors in LRP accounts for the mechanics of their catenary curves. To this end, we decomposed the force along the dome outline into the vertical and the tangential components (red and black arrows, respectively, in Fig. 2.4I, lower panel) at the mechanical equilibrium during the tissue growth simulations. The vertical force was uniform at the central domain but sharply decreased to zero in the peripheral region of the primordium (Fig. 2.4I, upper panel). The tangential force was the lowest at the dome center and increased toward the peripheries with inverse proportionality to the cosine of the tangential angle (Fig. S2.7D). The spatial distribution of vertical and tangential forces on the LRP outlines was consistent with that of the gravity and tangential tension of catenary chains, respectively (Figs. 2.4I and S2.7D). Thus, our simulations also support tissue growth behavior of LRP for the mechanics of catenary curve formation.

The mechanical and geometrical features of growing LRP (Fig. 2.4A-E, I) agreed with those assumed for a hypothetical catenary chain of extending length (Fig. 2.4F-H), whose (1) both ends are fixed resulting in the sharp boundary of force distribution while (2) its outline length increases under gravity. This consistency suggests that (1) the sharp boundary and (2) unidirectional and uniform force distribution are necessary for the formation of a catenary-curved LRP dome. The two elementary candidate rules of tissue growth are (1) periclinal divisions of the cells at the central domain of LRP and the lack of cell division at the peripheral edge of LRP, and (2) spatially uniform occurrence of unidirectional (i.e. anisotropic) tissue growth via periclinal divisions and/or cell expansions at the central domain (Fig. 2.4D, E).

Sharp boundary of periclinal cell division rate was required for catenary curve formation

To examine whether (1) the periclinal divisions of the cells at the central domain and the lack of cell division at the peripheral edge is indispensable for catenary curve formation, we first perturbed distribution of cell division rates within an LRP in simulations. In addition to the naturally occurring situation where a single cell layer with low periclinal cell division rate constitutes a sharp boundary separating rapidly dividing central region from mitotically quiescent outer region (Fig. 2.4D, E), we also simulated a hypothetical situation where multiple cell files with low periclinal cell division rate were assumed between the central and peripheral regions (light blue cells in Fig. 2.5A) to make a shallow gradient of division rate (Fig. 2.5A). In the latter case, the simulated dome outline became more extended towards the periphery than the normal situation ($30 < h$ at $|x| > 40$ in Fig. 2.5B) and deviated from the catenary curve even after incorporating the anisotropic cell expansion (Fig. 2.5C). This deviation became further exaggerated when more cell files with low division rate were assumed (shallower gradient model, Fig. S2.8A, B, D). Additionally, the spatial distribution of vertical force was less uniform and continuously decreased from the central to the peripheral domain (Fig. S2.8F-G, left panel). On the other hand, increasing the number of cell files with high division rate at the central domain (dark blue cells) to make a sharper boundary resulted in the outline that can be robustly fitted to a catenary curve with a larger value of the catenary parameter (increasing central zone model, Fig. S2.8C, E). These simulations predicted that the sharp boundary of cell division rate at the flanking region is required for the catenary curve formation.

We experimentally verified the requirement of the sharp boundary of cell division rate by using the Arabidopsis *puchi-1* mutant defective in a gene encoding an auxin-inducible AP2/EREBP-type transcription factor PUCHI (Hirota et al., 2007) (Fig. 2.5D). The *puchi-1* lost the sharp boundary due to the extra periclinal divisions at the flanking region significantly increasing the number of cell files to more than one cell layer as compared with one in wild type, whereas that with more than two cell layers did not increase (Fig. S2.9A, B) (Hirota et al., 2007). This defect specifically increased the number of cell layers at the flanking region, substantiating the shallow gradient of periclinal division rate assumed *in silico* (Fig. 2.5A). Intriguingly, the emerged LRP dome of the *puchi-1* mutant appeared to be more tail-extended (Fig. 2.5D), and thereby deviated from a catenary curve (i.e. averaged MSE higher than that of wild type in Fig. 2.5E). The consistency between the dome outlines of the *puchi-1* mutant *in vivo* and the simulations of shallow gradient *in silico* confirmed that the sharp boundary of division activity at the flanking region of LRP is required for the catenary curve formation.

Anisotropic and uniformly-distributed tissue growth contributes to catenary curve formation

To examine if (2) the spatially uniform occurrence of periclinal division is indispensable for the formation of the catenary-curved dome shape, we randomized the cell division orientation in simulations (Fig. 2.5F). The dome outline became less symmetric in the bilateral axis as seen for the displacement of the dome tip from the center, and thereby deviated from a catenary curve ($h < 30$ in Fig. 2.5F-H). The spatial distribution of vertical forces was accordingly less uniform (Fig. S2.8F-G, right panel).

We experimentally verified the requirement of the anisotropic tissue growth arising from the periclinal cell division by using the Arabidopsis *aur1 aur2* mutant where the two AURORA kinases genes indispensable for correct positioning of cell division plane in the LRP were disrupted simultaneously (Van Damme et al., 2011). In the *aur1 aur2* mutant, division-plane orientation (angle), especially that at the foot of the LRP, was significantly more variable than that in wild type (at the central domain of stage V in Figs. 2.5I and S2.9A, C) (Van Damme et al., 2011; von Wangenheim et al., 2016), substantiating the simulation with randomized division orientation described above (Fig. 2.5F). In the early stages (stage II and V in Fig. 2.5I), the *aur1 aur2* mutant consistently lost bilateral symmetry in their LRP outline, resulting in the deviation from a catenary curve (significantly higher MSE than that of the wild type; $h < 30$ in Fig. 2.5J). The consistent defects in the dome outlines between the *aur1 aur2* mutant and the simulations with randomized cell division orientation confirmed that anisotropic and uniformly-distributed tissue growth arising from the periclinal division was required for the catenary curve formation. Importantly, the fitness of *aur1 aur2* mutant root tip outline to a catenary curve improved as LRP developed and became similar to that of wild type ($30 < h$ in Fig. 2.5I, J). This observation further supports the hypothesis that the anisotropic cell expansion at the central domain, which occurs in both wild-type and *aur1 aur2* LRP (Figs. 2.4D, E and 2.5F, I), promotes (2) the anisotropic tissue growth and hence the catenary curve formation.

2.5. Discussion

Isometric scaling of plant root tip morphologies into a universal catenary curve

It has long been acknowledged that organ morphologies are conservative while being diverse among species depending on survival strategies and adaptation to the environment. Despite the morphological diversity of root tip in size (width) and internal cellular organization (Fig. S2.5) (Clowes, 2000; Hamamoto et al., 2006; Heimsch and Seago Jr, 2008), our morphometric analysis

revealed that the outlines of ten angiosperm species PRs and Arabidopsis LRs commonly fitted to a catenary curve and its essentially equivalent curve, a catenary-closest ellipse (Figs. 2.2A, S2.3, S2.4 and S2.6). The catenary curve is seen in free-hanging chains and bridges (Fig. 2B), which has several interesting features in mathematics, physics and architecture; (1) the shape is represented by a simple mathematical function with a single catenary parameter ($y = a \cosh(x/a) - a$)), (2) stably formed under gravity in a free-hanging chain, and (3) widely used in various architectures for its structural stability.

Each outline shape of root tip across root class and species is surprisingly represented by a single catenary parameter a (Fig. 2.3B, lower panels), which is the reciprocal of the dome curvature (Fig. 2.3B, upper panels) and also the tangential tension divided by the vertical force per unit length (Fig. 2.4H), representing both geometry and mechanics. From a mathematical interpretation, the catenary parameter works as a factor of an isometric scalability; i.e., each catenary curve is able to superimpose on universal parameter-free catenary curve via transforming equally on x- and y-coordinates with the catenary parameter (Fig. 2.3A). By the isometric scaling, indeed, any root tip outlines superimposed to the parameter-free catenary function (Fig. 2.3C-D). Other known examples of conservative organ outlines (e.g., skull of humans; cannon-bone of ox, sheep and giraffe (Thompson, 1917); beak of songbirds (Abzhanov, 2017; Campas et al., 2010)) superimpose among neighboring species via affine transformations which allow to transform the outlines on x- and y-coordinates with different rate and/or different directions of deformation (Campas et al., 2010; Fritz et al., 2014; Thompson, 1917)). This indicated that the isometric scalability of plant root tip outlines is a previously undescribed highly constrained solution for the conservative morphologies and suggested underlying constraints during the development.

The isometric scalability also mathematically ensures the reproducibility of the rescaled outline shape (Fig. 2.3A). This is distinct from a recently reported mechanism of the shape reproducibility within species via spatiotemporal averaging of variable cell growth during organogenesis (Hong et al., 2016). Despite the distinct mechanisms for the reproducibility, the shape of Arabidopsis PR and LR tips were highly reproducible (1–3% in Fig. 2.1D, E) in a level similar to Arabidopsis sepals ($\simeq$ 5%) (Hong et al., 2016). To date, morphological diversity among species (Abzhanov, 2017; Thompson, 1917) and shape reproducibility within a given species have been studied rather independently (Hervieux et al., 2017; Hong et al., 2016; Hong et al., 2018). The isometric scalability adequately achieves both diversity and reproducibility, recapitulating the conservative feature of organ morphologies. The general methodology established in this study (Fig. 2.3) provides a way to unravel the isometric scalability in other biological shapes.

Developmental constraints for the formation and maintenance of canary-curved dome

The geometry and mechanics of growing LRP (Fig. 2.4A-E, I) are consistent with those of a hypothetical catenary chain of extending length (Fig. 2.4F-H), which stably forms under (1) the sharp boundary and (2) unidirectional and uniform force distribution such as gravity. These mechanical consistencies proposed developmental constraints for the formation of catenary-curved dome; (1) unidirectional (i.e. anisotropic) tissue growth localized at the central domain of LRP and the lack of growth at the peripheral edge of LRP, and (2) spatially uniform occurrence of the anisotropic tissue growth via periclinal divisions and/or cell expansions at the central domain (Fig. 2.4D, E). Assuming these two tissue growth rules successfully recapitulated the spatial distribution of the force field that is predicted for the catenary-curved chain (Fig. 2.4G-I). The first constraint, (1) localized occurrence of the anisotropic tissue growth, was verified using Arabidopsis *puchi-1* mutant, which lost the sharp boundary due to the extra periclinal divisions at the flanking region (Figs. 2.5D and S2.9A, B) resulting in a tail-extended dome shape deviated from a catenary curve (Fig. 2.5D, E). The cell divisions in the peripheral regions of LRP are strongly repressed by the locally-expressed genes represented by *PUCHI*, and this restriction plays critical roles to define the organ boundaries and organ outgrowth (Hirota et al., 2007; Lavenus et al., 2015; Torres-Martinez et al., 2019; Trinh et al., 2019). Our findings further demonstrated the importance of the peripheral region for outline morphology of LRP. The second constraint, (2) spatially uniform occurrence of anisotropic tissue growth, was verified using Arabidopsis *aur1 aur2* mutant, in which the division-plane orientation was varied (Figs. 2. 5I and S9A, C). Less symmetric dome shape deviated from a catenary curve during the early LRP stages indicated the necessity of the uniform occurrence of periclinal divisions. On the other hand, developmental convergence of the LRP outlines to the catenary curve from later stage onwards also supports the significance of uniform occurrence of the anisotropic cell expansion which was normal in this mutant (Fig. 2.5I). These constraints are also consistent with the notion obtained in the previous studies; a small set of cell division rules reflecting cell geometry promotes periclinal divisions in the growing LRP (von Wangenheim et al., 2016). Additionally, upon LRP emergence, mechanical constraint from the overlaying tissues affects the LRP shape and its reproducibility perhaps through controlling potential growth pattern (Figs. 2.4E and S2.7A-C) (Lucas et al., 2013; Vermeer et al., 2014). Taken together, we proposed that the spatiotemporal regulation of tissue growth at the central or peripheral region under the control of specific sets of regulators (Lavenus et al., 2015; Torres-Martinez et al., 2019) is the developmental constraints for the catenary-shaped root tip in the LRP development.

The catenary parameter is stabilized around the emergence stage of LRP development, where the RAM is established in preparation for successive cell proliferation to extend LRs (Figs. 2.4A-C and S2.1B, C) (Goh et al., 2016; von Wangenheim et al., 2016), and further maintained in the matured LRs (Fig. 2.3B). Interestingly, previously-reported growth simulations based on LR and PR cell geometries predicted that a localized and uniform occurrence of anisotropic tissue growth at RAM was required for maintaining organ outline morphology as well as the cellular organization (Hejnowicz, 1984; Nakielski and Lipowczan, 2013; Szymanowska-Pułka et al., 2012), and the cellular geometry within root tip of embryo is the mechanical constraint on tissue growth (Bassel et al., 2014). We hypothesized the tissue growth rules of RAM might fulfill the developmental constraint for catenary-shaped dome formation through anisotropic growth via oriented cell divisions and expansion and for maintaining a largely constant width. Furthermore, the structural feature of RAM is essentially conserved across vascular plants under the control of shared regulatory mechanisms (Huang and Schiefelbein, 2015). Therefore, it will be interesting to study in future whether (1) the localized and (2) spatially uniform occurrence of anisotropic tissue growth are shared constraints for the maintenance of a catenary curve across the root classes and species. Underpinning of the constraints by the cell wall extensibility and the turgor pressure of individual cells may be also predicted in future, if the formulation proposed by Lockhart (Lockhart, 1965) and the elasto-plastic cell deformation (Geitmann and Ortega, 2009; Ortega, 1985) are to be incorporated into the present vertex model.

The catenary curve becomes a 3D dome surface when it is rotated (around y-axis) as seen in the root tip with a rotational symmetry (Fig. S2.1A), and such 3D shapes are also used in architectures of various sizes and materials (e.g., St. Paul's Cathedral (Heyman, 1998) and snow igloo (Handy, 1973)). 3D root tip shapes have been previously shown to affect penetration ability of roots into soil in wheat (Colombi et al., 2017), or into a hard medium in Arabidopsis (Roue et al., 2020). In addition, an engineering approach using soft robots suggested that plant root tip morphology governs the penetration stress and efficient elongation in soil (Mishra et al., 2018). Our simulations indicated that the mechanical force produced by the tissue growth was uniformly distributed on the surface of the catenary-curved root tips (Figs. 2.4G-I, S8F-G). This finding encourages us to step further to a future challenge to test whether the force produced by the interaction between the root tip and soil is also uniformly distributed onto the entire tip surface, and thereby contributes to the efficient penetration of roots to soil.

2.6. Figures

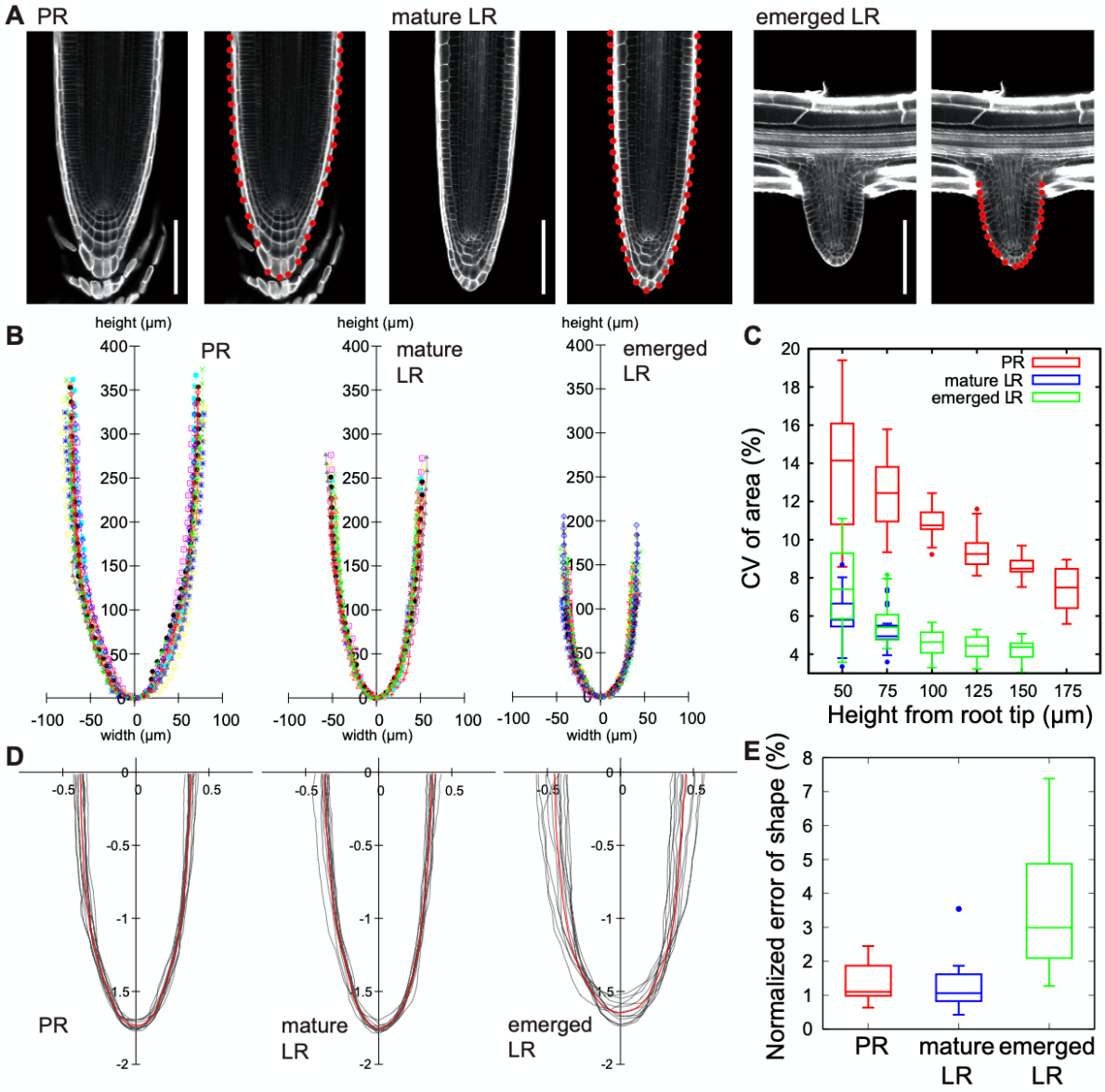

Fig. 2.1. Reproducible size and shape of root tip outlines in Arabidopsis

(A) Longitudinal confocal sections of a PR, a mature LR, and an emerged LR. Cell walls were stained with SR2200. Red points indicate cell junctions on the dome outline. Scale bar = 100 μm.

(B) Reproducibility of root tip size. Outlines of multiple samples from each root class were superimposed with different colors. Points indicate cell junctions on the outline.

(C) Reproducibility of root tip area. Root tip areas measured on the median longitudinal section up to the indicated heights from the root tip. Size reproducibility is indicated by coefficient of variation (CV (%) = (s.d. of area) x 100 / (mean of area)). Higher CV of PR than that of LR is likely attributable to phase differences of root cap sloughing among samples.

(D) Reproducibility of root tip shape. Outlines of multiple root samples were normalized by the radial Fourier series expansion method (Material and Methods) and superimposed (grey). Median outlines are shown in red.

(E) A graph showing shape reproducibility indicator (Eqn. 2.9) of tip outlines for distinct root types. The upper and lower hinges, the middle lines and the error bars of the box plots in C and E represent the 25th, 75th, and 50th (median) percentiles, and s.d., respectively. (B)-(E) are drawn from identical data sets (n = 12 [PR], n = 12 [mature LR], n = 11 [emerged LR]).

The samples in A were prepared and imaged by T. Goh.

The ellipse estimates in D and E were performed by S. Tsugawa.

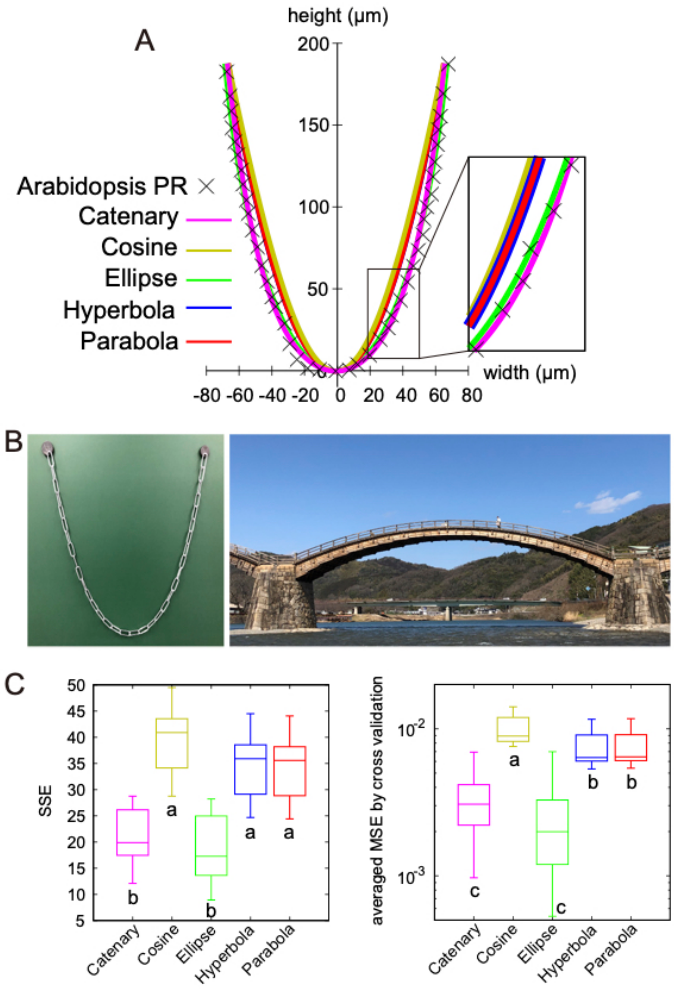

Fig. 2.2. Catenary is an isometrically scalable function and the best-fit model for root tip outlines.

(A) Non-linear least-squares (NLS) fitting of a representative Arabidopsis PR outline with five geometrical functions (catenary, cosine, ellipse, hyperbola, and parabola).

(B) Examples of catenary curves in architectures: a chain hanging with its both ends fixed under gravity (left panel) and the Kintai wooden bridge in Yamaguchi prefecture, Japan (right panel).

(C) Sample standard error (SSE) between PR sample dome outlines (n = 12) and the indicated curve function (left panel). The averaged MSE by cross validation between PR sample dome outlines (n = 12) and the indicated curve function (right panel; Eqn. 2.12). Different letters (a, b, c) denote statistically significant differences ($P < 0.05$) among means by Tukey's honestly significant difference (HSD) test. The upper and lower hinges, the middle lines and the error bars of box plots represent the 25th, 75th, and 50th percentiles, and SD, respectively.

The cross validation and Tukey's honestly significant difference test in C was performed by S. Tsugawa.

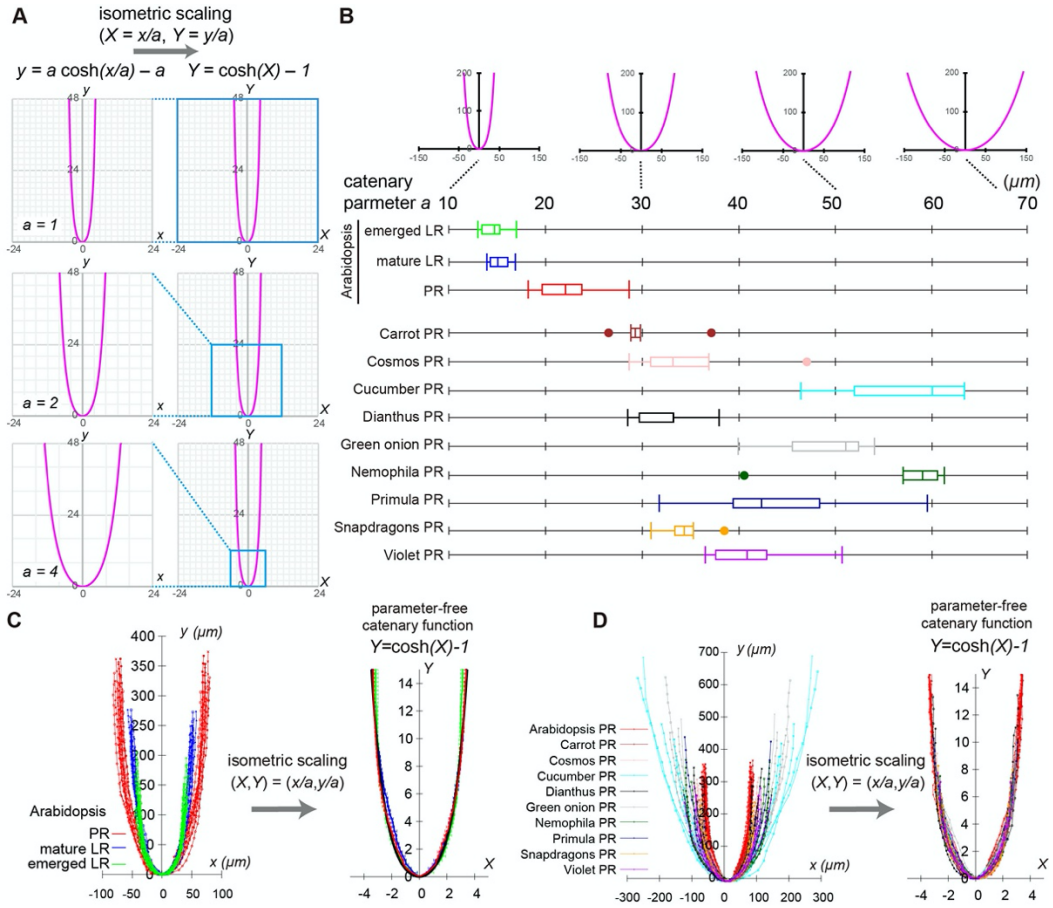

Fig. 2.3 Isometrically scalable root tip outlines to a parameter-free catenary curve.

(A) Isometric scalability of catenary function. Catenary curves ($y = a\cosh(x/a) - a$) with $a = 1$, 2 and 4 (left panels) are isometrically scalable into a parameter-free catenary function ($Y = \cosh(X) - 1$, $X = x/a$, $Y = y/a$, right panels).

(B) Catenary curves with a = 10, 30, 50 and 70 (upper panel). Catenary parameter a of root tip outlines quantified by NLS method (bottom panel). Arabidopsis PR, mature and emerged LR outlines (n = 12 [PR], n = 12 [mature LR] and n = 11 [emerged LR]), and PR of nine angiosperm species (n = 5 for each species) were analyzed. The fitted value of a indicated high reproducibility in Arabidopsis (CV of a ~14% in PR, ~7.2% in mature LR and ~8.5% in emerged LR), consistently with the level of size reproducibility (CV of root tip area in Fig. 2.1C), and was on average 50% larger in the PR than in the LR. The right and left hinges, the middle lines and the error bars of box plots represent the 25th, 75th, and 50th percentiles, and s.d., respectively.

(C, D) Outlines of Arabidopsis PRs and LRs (left panel in C) and ten angiosperm species PRs (left panel in D) were isometrically scalable to a parameter-free catenary curve using distinct catenary parameter a (respective right panels). Samples in C and D are identical data sets to B. Sample sets of Arabidopsis PRs, mature LRs and emerged LRs shown in B and C are identical to those used in Fig. 2.1B.

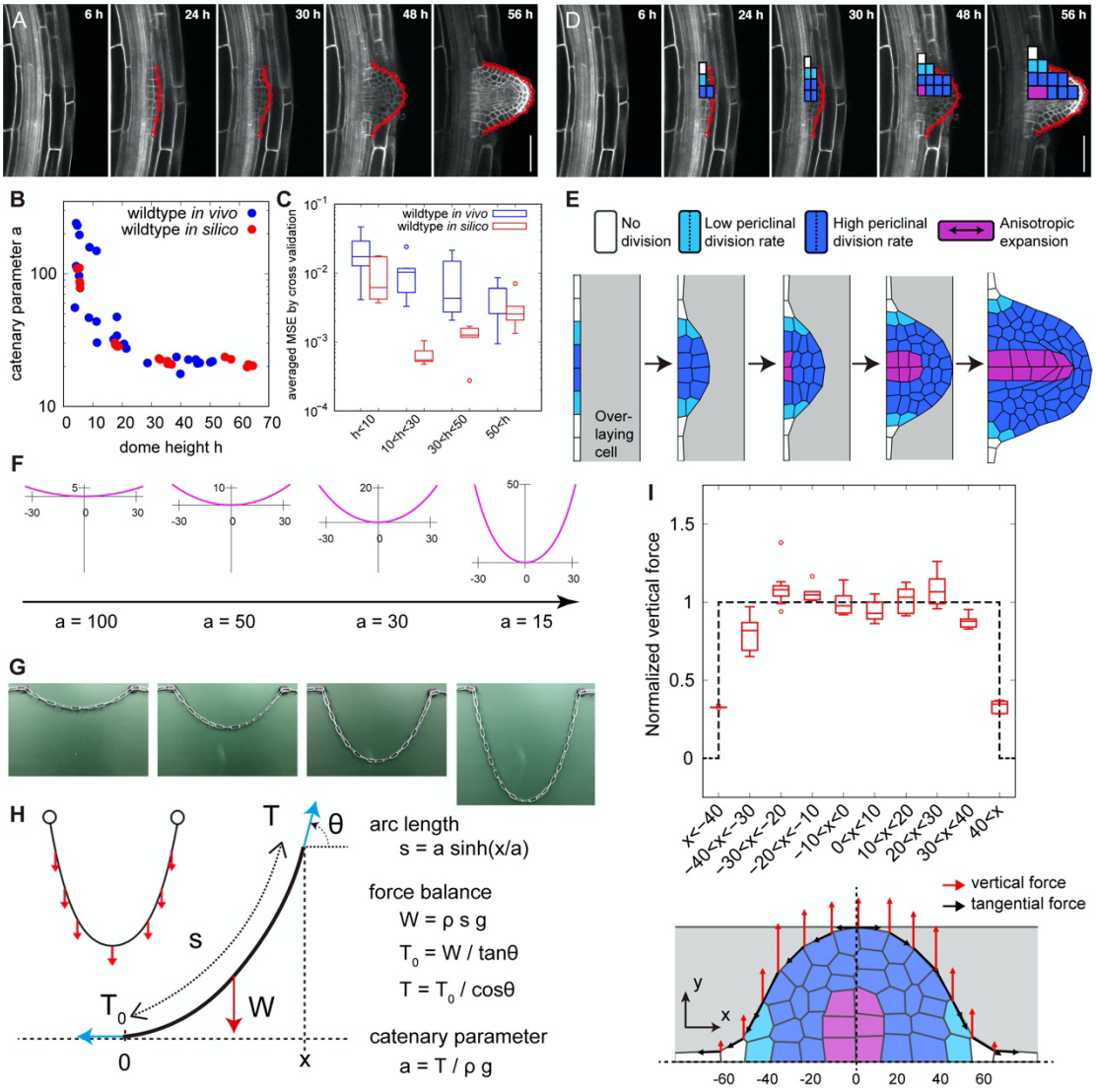

Fig. 2.4. Geometry and mechanics of catenary-curved dome during LRP tissue growth

(A) Longitudinal confocal sections from a time-lapse imaging of a developing Arabidopsis LRP visualized using *35S:Lti6b-GFP* (a plasma membrane marker). The elapsed time (h) after gravistimulation for inducing LRP development is indicated in each panel. Red lines indicate LRP dome outlines. The scale bar indicates 50 µm.

(B) A graph of catenary parameter *a* (y-axis) plotted against dome height *h* (x-axis) of growing LRP outlines quantified by the NLS method.

(C) Cross validation test (Eqn. 2.12) of *in vivo* and *in silico* LRP outlines fitted with catenary function. Shown are averaged MSE (y-axis) against the dome height *h* (x-axis) *in vivo* (blue, n = 10 [h < 10], n = 10 [10 < h < 30], n = 10 [30 < h < 50], n = 10 [50 < h]) and *in silico* (red, n = 5 for each dome height range, h < 10, 10 < h < 30 and 30 < h < 50).

(D) Rules of cell divisions (white: no division, light blue: single division, deep blue: three consecutive divisions), and anisotropic cell expansion in the proximodistal direction (magenta: presence, other colors: absence) observed in the LRP development *in vivo*.

(E) Tissue-mechanical simulation from a flat primordium to dome formation during LRP development with a mass of overlaying cells (grey). Cells division and expansion rules (colored-coded as in (D)) were incorporated into the simulation. See also Movie S1.

(F) Catenary curves of different parameter values a with its width (x-axis) roughly equal to that of an actual LRP (Fig. 2.4A).

(G) Catenary curves formed by the chains of increasing length with fixed ends under gravity.

(H) Mechanics of catenary curve; The gravity works as vertically uniform force W on the chain, and is balanced with the tangential tension T at the mechanical equilibrium. s, a, x, ρ, g, and θ denote chain outline length, catenary parameter, x-coordinate of the catenary chain, mass density, the gravitational acceleration, and the angle from horizontal x-axis, respectively. ρg represents the gravitational (vertical) force per unit length.

(I) Distribution of vertical force (red arrows) and tangential force (black arrows) on dome outlines after cell expansion in five representative simulations (bottom panel shows a representative outcome). The magnitude of vertical force normalized by its spatial average over the dividing zone (dark blue and light blue cells in the bottom panel) plotted as a function of x-coordinate along the dome width (upper panel). Error bars denote SD of five independent simulations. The upper and lower hinges, and the middle lines of box plots in C and I represent the 25th, 75th, and 50th percentiles, respectively.

The samples in A were prepared and imaged by T. Goh. The box plots in C and I were performed by S. Tsugawa.

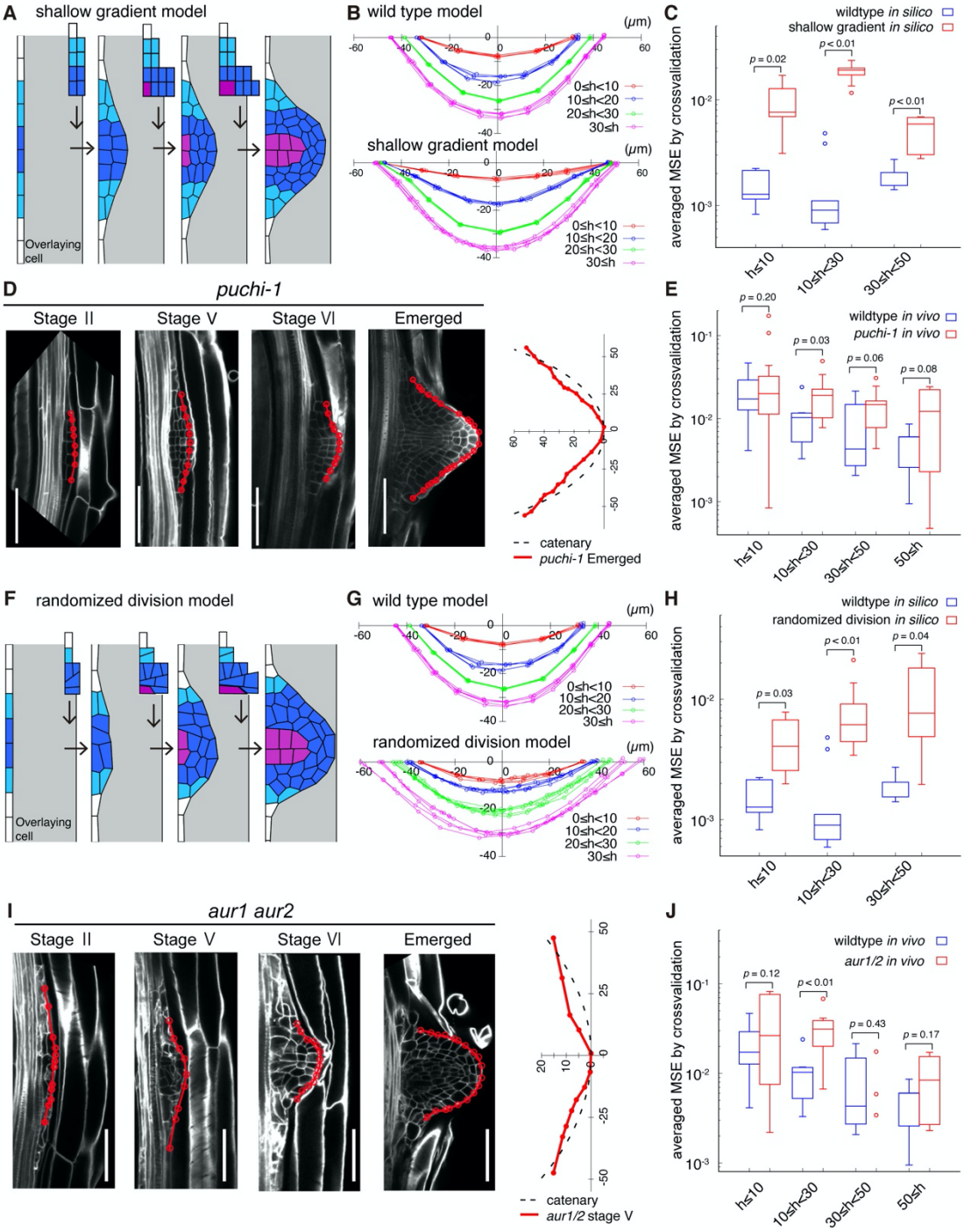

Fig. 2.5. Localized periclinal cell divisions of LRP determine its dome shape

(A, F) Simulation of (A) the shallow gradient model assuming supernumerary cells in the flanking region (light blue), and (F) the randomized division model assuming randomized cell division orientation in the central domain (dark blue). Division and expansion rules of remaining cells were left unchanged from those used in Fig. 2.4E. Panels from left to right correspond to LRP shapes observed *in vivo* at h < 10, 10 < h < 20, 20 < h < 30 and 30 < h < 50. See also Movie 1.

(B, G) Dome outlines during the *in silico* simulation of the shallow gradient model (B) and the randomized division model (G). The dome outlines of wild-type templates are derived from Fig. 2.4E. Colors denote root dome height (μm).

(C, H) Averaged MSE from the cross-validation test (Eq. 12) with catenary curve in case of simulations (*in silico*) of wild-type template (blue), the shallow gradient model (red in C; $n = 5$ for each dome height range, $h < 10$, $10 < h < 30$ and $30 < h < 50$), and the randomized division model (red in H; $n = 5$ for each dome height range, $h < 10$, $10 < h < 30$ and $30 < h < 50$). Welch's t-test was performed.

(D, I) Longitudinal confocal sections of LRP at different developmental stages in *puchi-1* (D) and *aur1 aur2* (I) mutants (left panels), and their dome outlines plotted in the cartesian coordinate together with an imaginary fitted catenary curve (dotted black line) (right panels). Cell walls were stained with SR2200 (white). Red lines and circles indicate LRP dome outlines and cell junctions, respectively. Scale bars indicate 50 μm.

(E, J) Averaged MSE from the cross-validation test with catenary curves for Arabidopsis LRP of wild type (blue), *puchi-1* (red in E; $n = 21$ [$h < 10$], $n = 9$ [$10 < h < 30$], $n = 9$ [$30 < h < 50$], $n = 7$ [$50 < h$]), and *aur1 aur2* mutants (red in J; $n = 9$ [$h < 10$], $n = 10$ [$10 < h < 30$], $n = 3$ [$30 < h < 50$], $n = 4$ [$50 < h$]). Welch's t-test was performed. The upper and lower hinges, the middle lines and error bars of box plots in C, E, H and J represent the 25th, 75th, and 50th percentiles, and SD, respectively. Date sets for wild type used in C, E, H, J were identical to those in Fig. 2.4C.

The samples in B and I were prepared and imaged by T. Goh.

The box plots and Welch's unpaired, one-tailed t-test in C, E, H and J were performed by S. Tsugawa.

2.7. Supporting figures

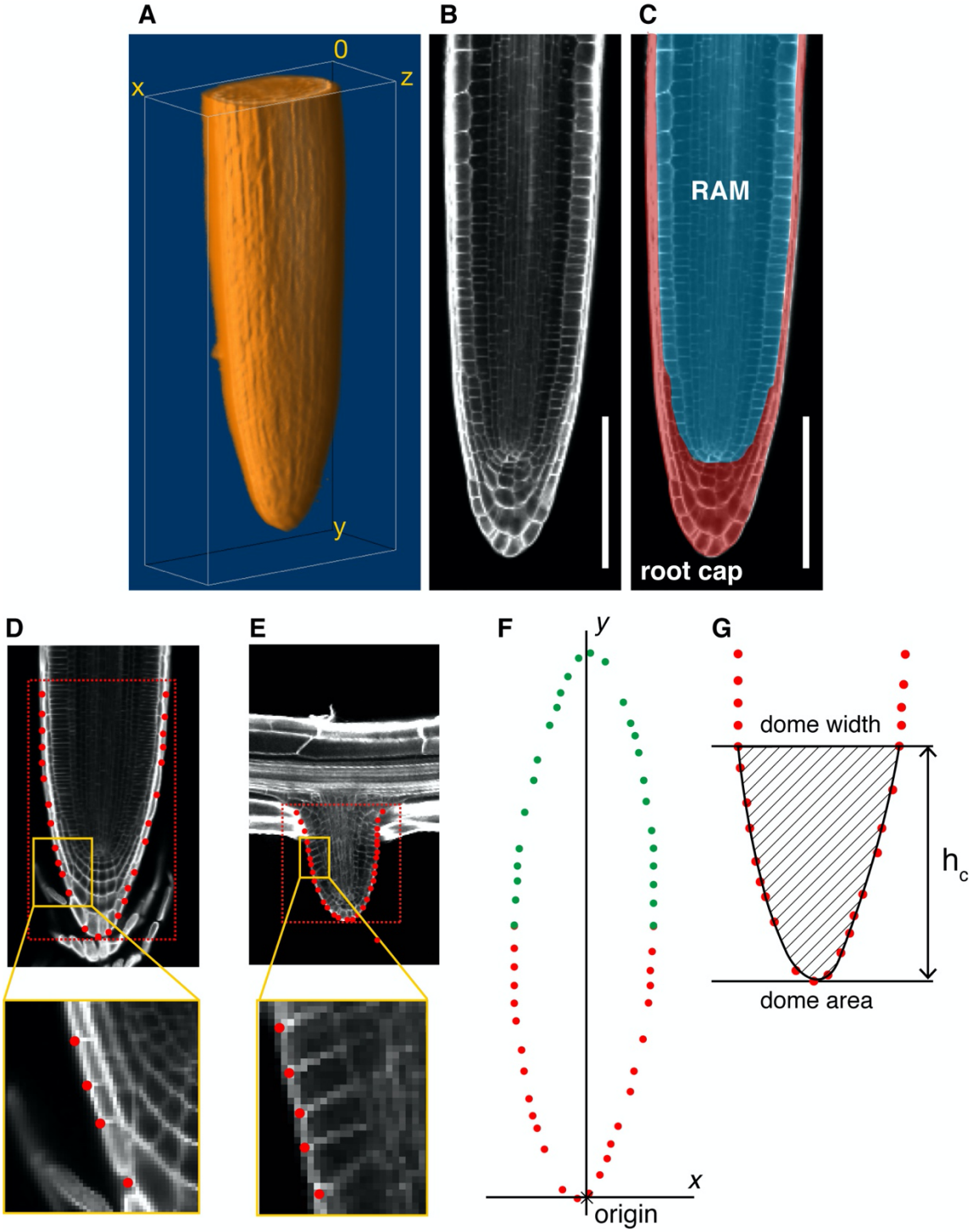

Fig. S2.1. Determination of root dome outlines and unification of the coordinate system.

(A) 3D view of a mature LR (lateral root).

(B, C) Raw image of a vertical section of a mature LR (B). The root tip is composed of RAM (root apical meristem; blue region) and a root cap (red region) (C). Scale bars indicate 100 µm.

(D, E) Root tip outlines of a PR (primary root; D) and an LR (E) were determined from the cell junction positions on the dome outlines (red points, enlarged figure in bottom panel). Red dotted boxes denote the region of interest, which ranged from the root tip to the boundary between the proliferation and elongation zone (D) and to the vascular cells of parent roots (E).

(F) Unification of the coordinate system (see Material and Methods). Red points indicate the original positions on the root tip outline, and green points indicate the points duplicated and turned by 180 degree. The origin of x- and y- coordinates were determined as the mean of x of all points and the minimal y of the original points.

(G) Illustration of how to measure the dome width and area (shaded region) up to the indicated height h_c from the root tip.

The samples in A, B, C, D and E were prepared and imaged by T. Goh.

The unification of the coordinate system in F and G were performed by S. Tsugawa.

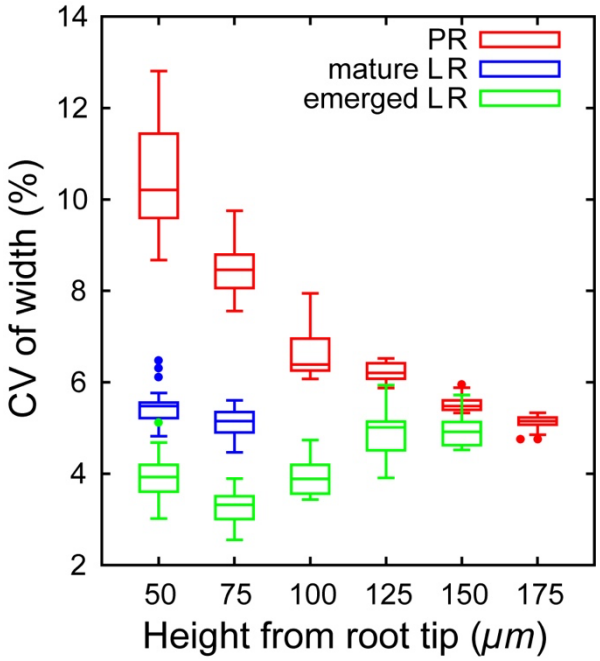

Fig. S2.2. Size reproducibility of root tip width.

Root tip dome width measured on the median longitudinal section up to the indicated heights from the root tip. Root tip width measured on the median longitudinal section up to the indicated height from the dome tip (25 μm steps). The size reproducibility is indicated by the coefficient of variation (CV (%) = (SD of width) x 100 / (mean of width)). The lower and upper hinges, the middle lines and the error bars of box plots represent the 25th, 75th, and 50th percentiles, and SD, respectively. Data sets were identical to those of Fig. 2.1 B-E.

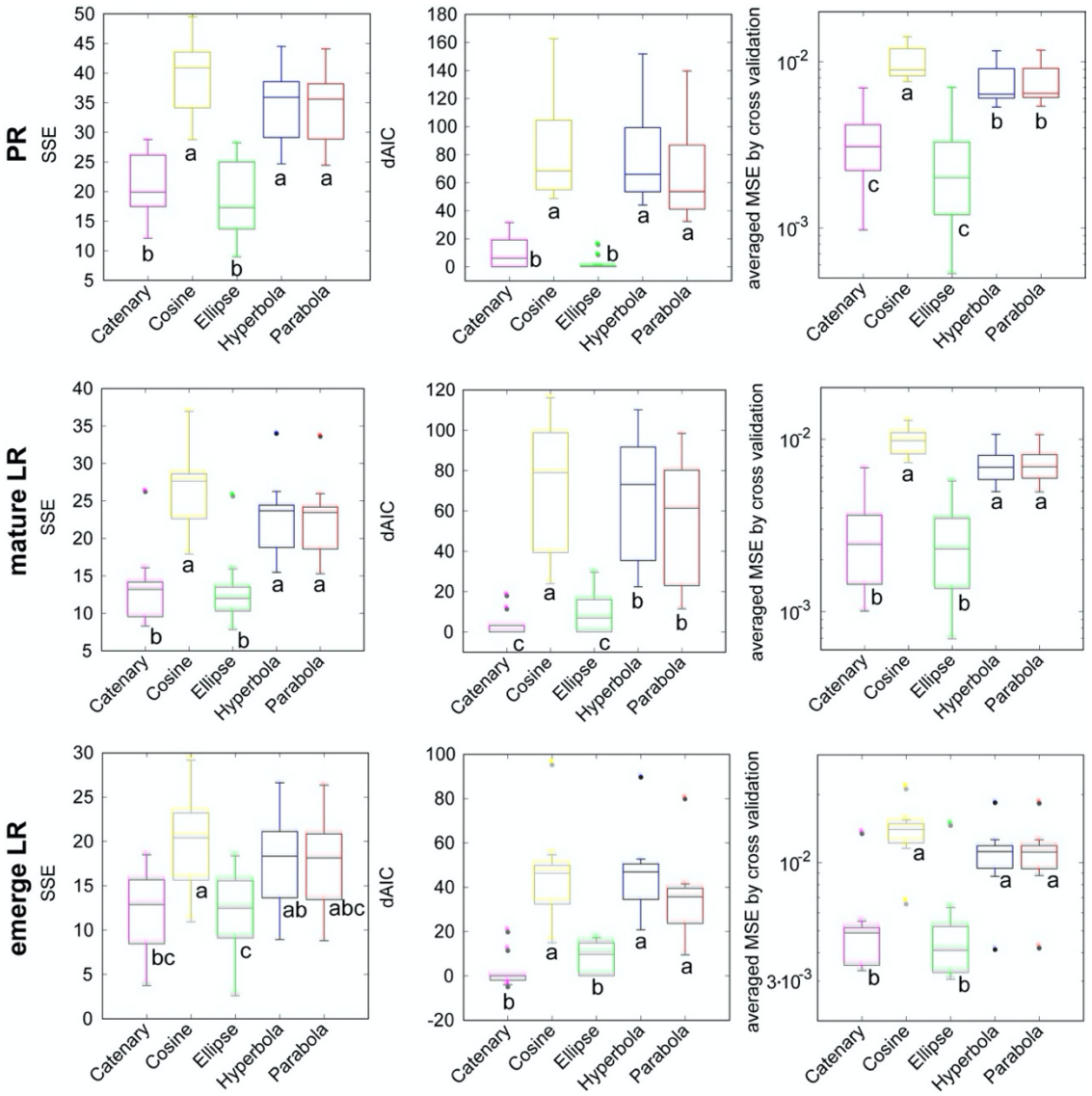

Fig. S2.3. Statistical model selection of best-fitting model of the root tip outlines of Arabidopsis using SSE, ΔAIC (Akaike information criterion) and average MSE (mean squared error).

SSE (left panels), ΔAIC (central panels), and average MSE by cross validation (right panels) between the dome outlines and the five model functions. SSE and average MSE for PRs were identical with Fig. 2.2C, E, respectively. The lower and upper hinges, the middle lines, and the error bars of box plots represent the 25th, 75th, and 50th percentiles, and SD, respectively. Sample numbers are n = 12 (PR), n = 11 (mature LR), and n = 12 (emerged LR). See Material and Methods for definition of SSE, ΔAIC and MSE. Different letters (a, b, c) denote statistically significant differences ($P < 0.05$) among means by Tukey's honestly significant difference (HSD) test.

The cross validation and Tukey's honestly significant difference test in C was performed by S. Tsugawa.

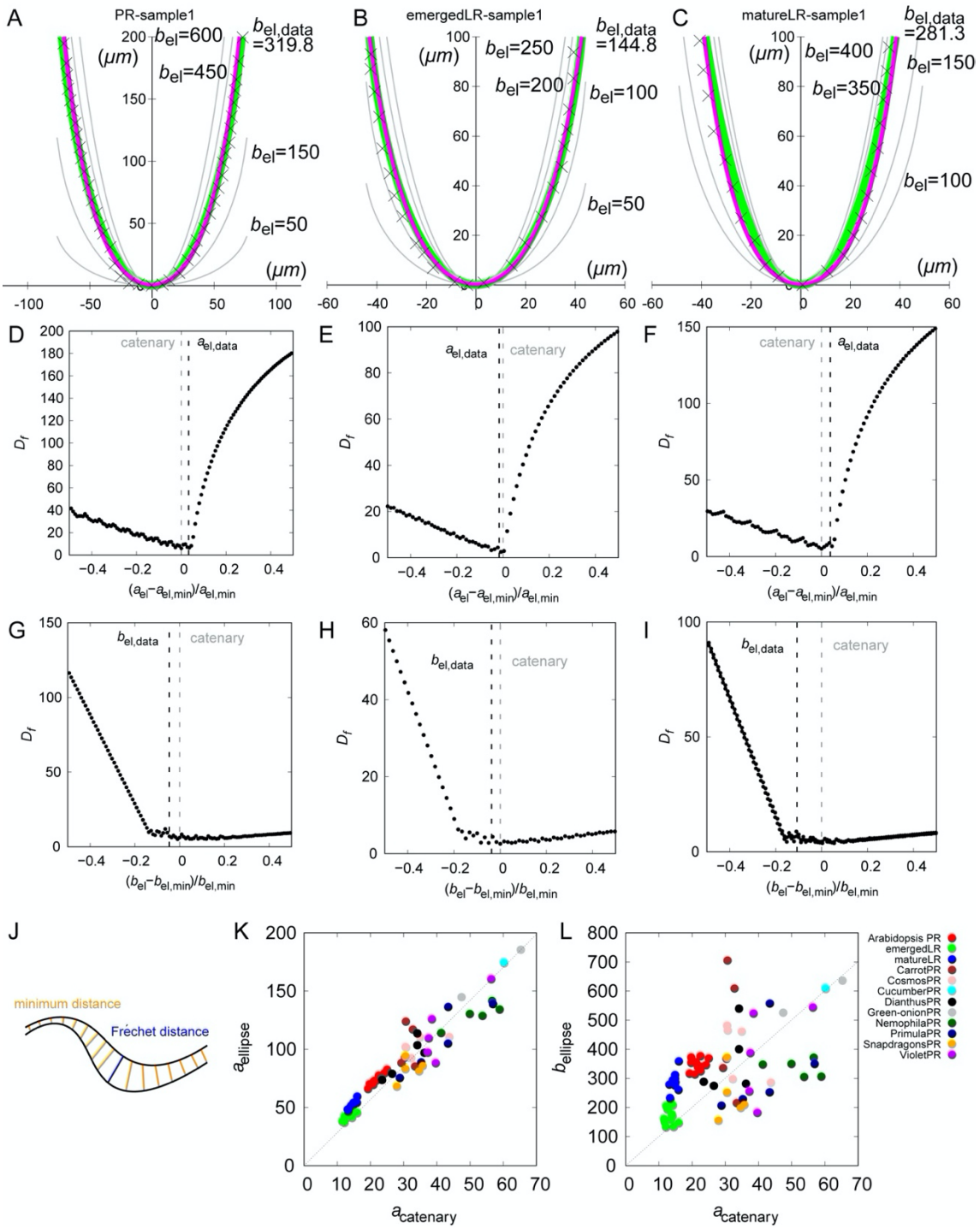

Fig. S2.4. Quantitative comparison of the catenary and ellipse functions

(A-C) The fitted function of a catenary (magenta) and an ellipse (green) to a sample of a PR (A), an emerged LR (B) and a matured LR (C). Grey lines indicate ellipses ($y = b_{ellipse} - b_{ellipse}$

$\sqrt{1 - x^2/a^2_{ellipse}}$) with different values of the ellipse parameter $b_{ellipse}$ (abbreviated as b_{el}) given the fitted value of the other ellipse parameter $a_{ellipse}$ ($a_{ellipse}$ = 78.0 [A], = 45.0 [B] and = 50.1 [C]; abbreviated as a_{el}), demonstrating that the fitted ellipse is apparently closest to the fitted catenary among the ellipses. Data points (X) represent root tip outlines identical to those in Fig. 2.1A.

(D-J) We quantitatively evaluated the closeness using the bottleneck distance between two different curves (J), known as the Fréchet distance given by $D_f = inf_{\alpha,\beta} \max_{t\in[0,1]} \{d(catenary(\alpha(t)), ellipse(\beta(t)))\}$, where d denotes distance function; α and β denote reparametrization of [0, 1] to a catenary and an ellipse, respectively, within the range of the plant root sample width. Fréchet distance was numerically measured by discretizing t into 200 equi-spaced samples. We revealed that the fitted ellipse (black dashed line) was almost closest to the fitted catenary curve (grey dashed line) among any ellipses given the fitted value of $b_{ellipse}$ (abbreviated as $b_{el.data}$; D-F) or $a_{ellipse}$ (abbreviated as $a_{el.data}$; G-I), for all samples of PRs (D, G), emerged LRs (E, H) and matured LRs (F, I). $a_{el.min}$ and $b_{el.min}$ denote the parameters of the closest ellipse indicating the global minimum of Fréchet distance, whereas the multiple local minima and maxima in the order of ± 1 are due to numerical errors.

(K, L) The fitted values of $a_{ellipse}$ (K) and $b_{ellipse}$ (L) were proportional to the fitted catenary parameter $a_{catenary}$ among PR and LR samples, i.e., $a_{ellipse} = 2.84a_{catenary}$ and $b_{ellipse} = 10.0a_{catenary}$, respectively (grey dotted line). This proportionality enabled us to parametrize the ellipse by $a_{catenary}$ alone via substituting the proportionalities: $y = 10.0a_{catenary}\sqrt{1 - \left(\frac{x}{2.84a_{catenary}}\right)^2}$ We referred to this function as the catenary-closest ellipse. By scaling of both x- and y-coordinates with $a_{catenary}$, any catenary-closest ellipses commonly converge to a unique function ($Y = 10.0\sqrt{1 - \left(\frac{X}{2.84}\right)^2}$, $X = x/a_{catenary}$, $Y = y/a_{catenary}$).

These quantitative comparisons were performed by S. Tsugawa.

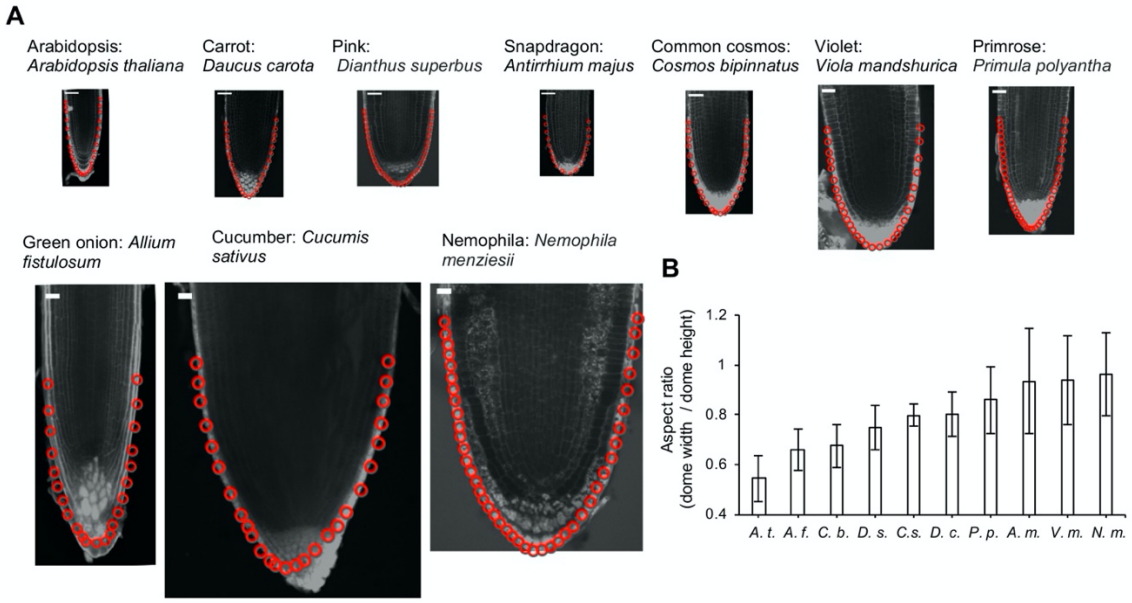

C

Initial of species name	*A. t.*	*A. f.*	*C. b.*	*D. s.*	*C. s.*	*D. c.*	*P. p.*	*A. m.*	*V. m.*	*N. m.*
Meristem type	Close	Open	Close	Close	Open	Close	Close	Close	Close	Close
Grand-tissue cell layers	2	2	3	2	5	3	3	2	2	4

Fig. S2.5. PR tip outlines in ten angiosperm species.

(A) Root tip outline (red circles) of each species. Scale bars indicate 50 μm.

(B) The aspect ratio (dome width / dome height) of the root tip for each species (n = 5 for each species).

(C) The cellular organization of root tips among species. The meristem types and the number of ground-tissue cell layers appeared to be species-dependent.

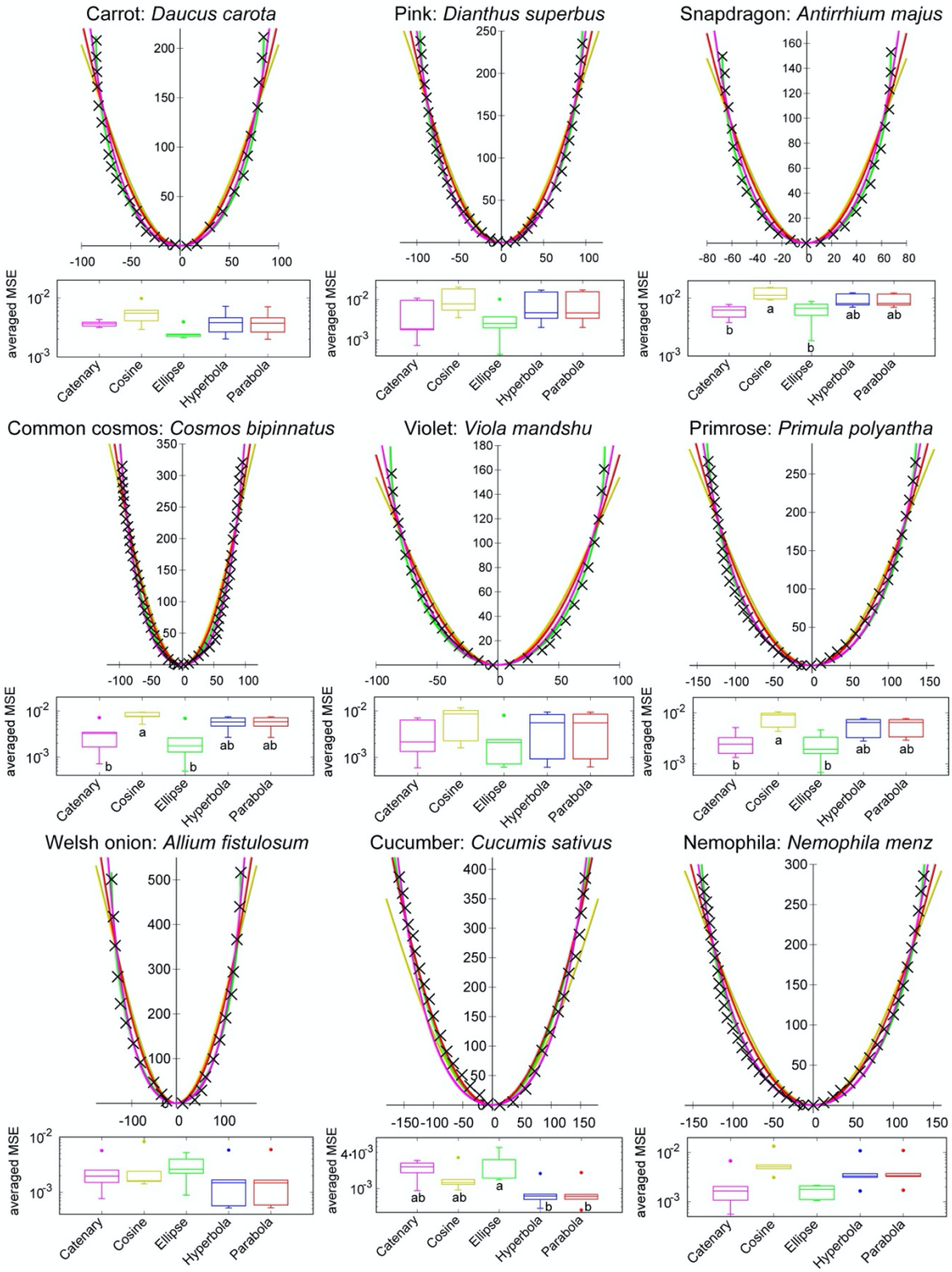

Fig. S2.6. Average MSE of PR tip shape in nine angiosperm species.

The average MSE from a cross validation test with the five functions for each species (n = 5 for each species). Different letters (a, b, c) denote statistically significant differences ($P < 0.05$) among means by Tukey's honestly significant difference (HSD) test.

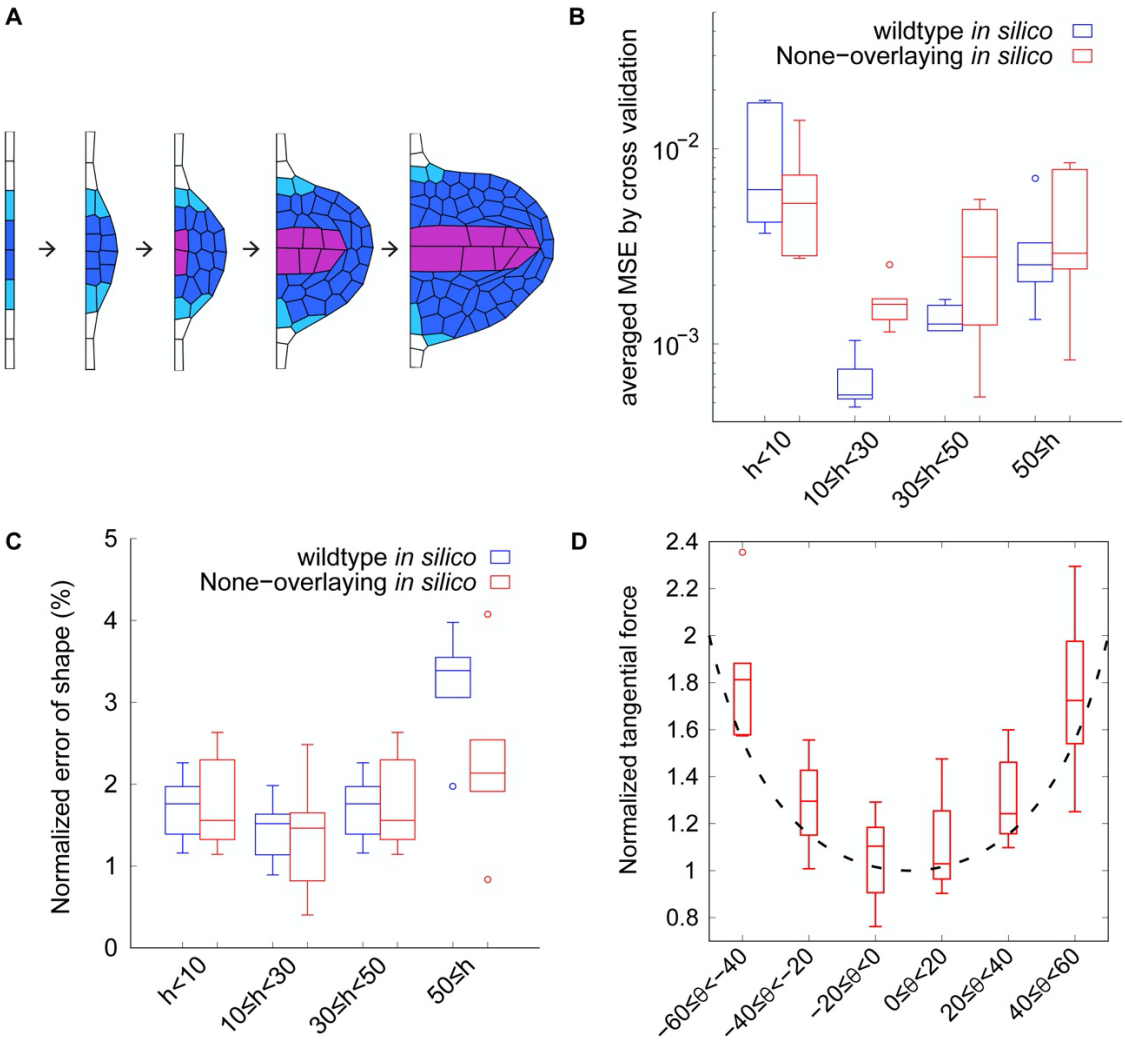

Fig. S2.7. LRP development *in silico*.

(A) Simulation without a giant imaginal cell (none-overlaying cell model).

(B, C) average MSE from the cross validation test with a catenary curve (B; Eqn. 2.12) and the shape reproducibility indicator (C; Eqn. 2.9) of tip outline during simulations (*in silico*) of the wild type (blue; identical with Fig. 2.4C, red) and the non-overlaying cell (red; n = 5 for each dome height range, h < 10, 10 < h < 30 and 30 < h < 50) models.

(D) Tangential force on the LRP surface. The magnitude of tangential force (black arrow in Fig. 2.4I bottom panel) after cell expansion. Vertex model simulations (box plot) and theoretical prediction based on a catenary-curved chain ($T/T_0 = 1/cos\theta$ in Fig. 2.4H; dashed line). The force of each cell on the outline (red arrow in Fig. 2.4I, upper panel) was normalized by that at the dome tip and plotted as a function of θ of the x-coordinate of the dome (Fig. 2.4H). The lower and upper hinges, and the middle lines of box plots represent the 25th, 75th, and 50th percentiles, respectively. The error bars denote the SD of five independent simulations. Sample sets were identical to those of Fig. 2.4I.

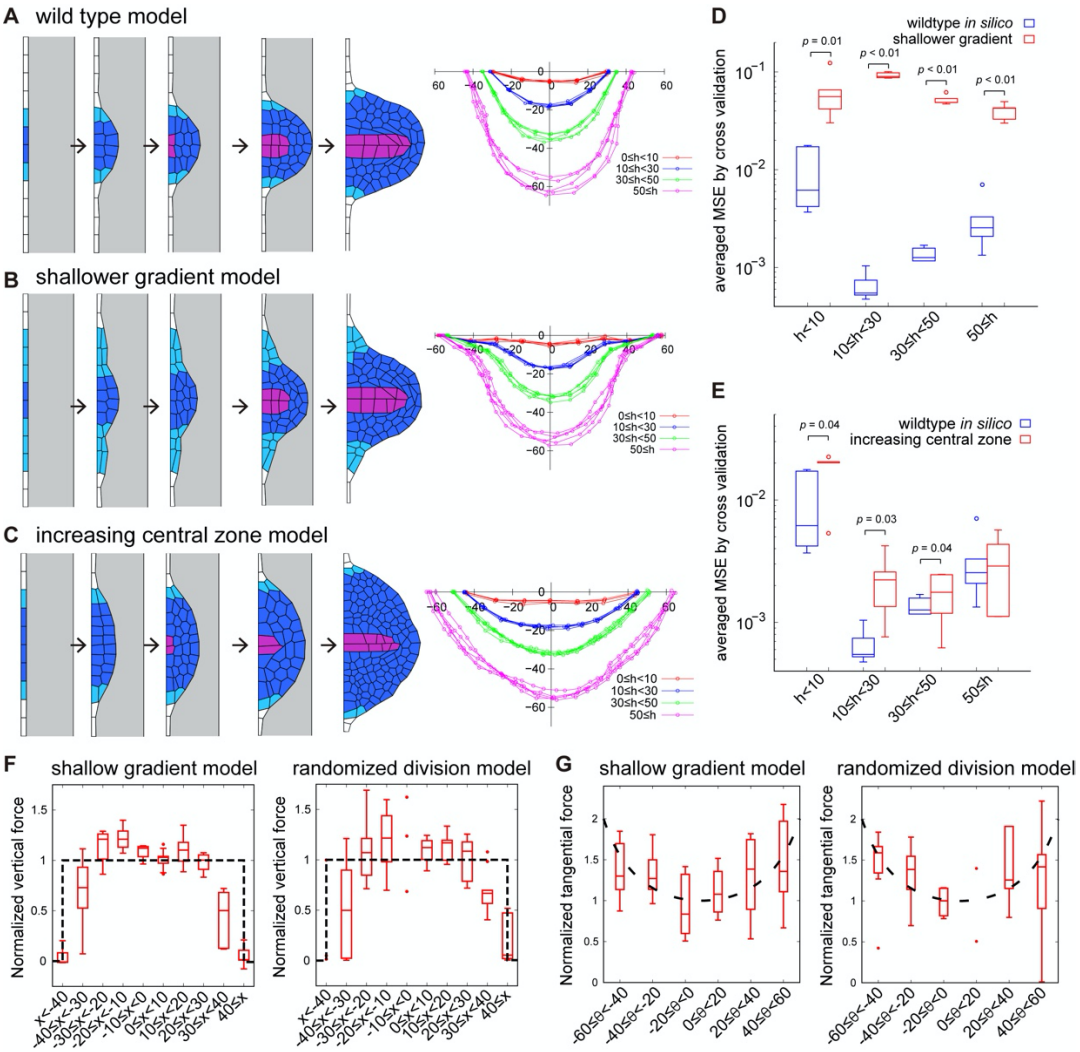

Fig. S2.8. Tissue growth rules affects its dome shape

(A-C) Developmental time course of vertex model simulations (left) and the root tip outlines (right) of the wildtype model (A; Fig. 2.4), the shallower gradient model (B) and the increasing central zone model (C). Color coding of cells (left) and outlines (right) are identical with that of Fig. 2.5A and B, respectively. **(D, E)** The average MSE from the cross validation test with a catenary curve (n = 5 for each dome height range, $h < 10$, $10 \leq h < 30$ and $30 \leq h < 50$) in wild type model (A), the shallower gradient (by increasing flanking region, light blue cells) model (B) and the increasing central region (dark blue cells) model (C). **(F, G)** The magnitude of vertical force (F) and tangential force (G) normalized by its spatial average over the dividing zone (dark blue and light blue cells in the right panel in Fig. 2.5A, F) plotted as a function of x-coordinate along the dome width in the shallow gradient model (left panel) and the randomized division model (right panel). The lower and upper hinges, and the middle lines of box plots in D, E, F and G represent the 25th, 75th, and 50th percentiles, respectively. The error bars denote the SD of five independent simulations.

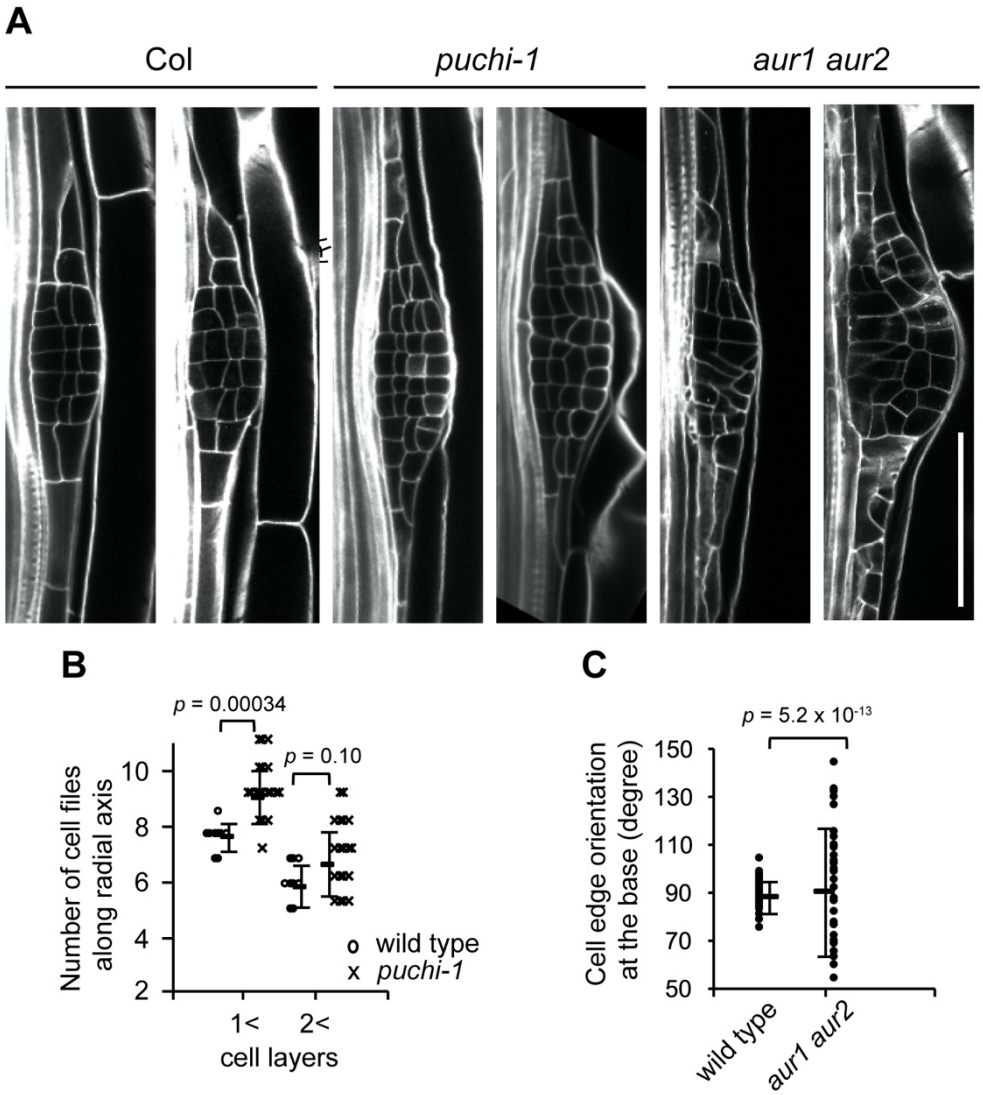

Fig. S2.9. Cell division defects of *puchi-1* and *aur1 aur2 in vivo*.

(A) Stage IV LRPs of Col, *puchi-1* and *aur1 aur2*. Scale bar = 50 μm.

(B) The number of cell files with more than one or two cell layers in the wild type (left, n = 5) and the puchi-1 mutant (right, n = 17) at stage IV.

(C) The orientation of cell division θ in the wild type (left, n = 5) and the aur1 aur2 mutant (right, n = 5) at stage IV. A t-test was performed after confirming a normal distribution by Kolmogorov-Smirnov test. The error bars in B and C indicate SD.

3. Distally localized proliferation imposes symmetric smoothing of plant vascular boundary

Some figures in this thesis were obtained in collaboration with my colleague, S. Miyashima. I clarified his contribution in each caption.

3.1. Abstract

Proliferating tissue is separated by a sharp boundary symmetrically during organogenesis (SAM;Caggiano, 2017, embryo, vascular, vertebrate neural tube). The boundary is smooth in the cell shape and arrangements by the tissue fluidity (i.e., cell migration and intercalation) in animal systems (Landsberg, 2009). Plant systems lack such fluidity due to rigid cell walls. Although regulatory molecules initially define the symmetric zonation of the boundaries (Heisler; bisymmetry by cytokinin-auxin; secondary growth; CUC), whether and how the cell arrangement is smoothed during tissue growth remains unclear. Using the cell-geometric quantification (Rudolf et al., 2015 Umetsu et al., 2014 Landsberg et al., 2009 Aliee et al., 2012) combined with cell lineage tracking in *Arabidopsis* primary root vascular tissue during cambial growth (Miyashima-2019), we show the boundary is smooth, similar to the animal epithelium. Moreover, the arrangement of vascular cells improves bisymmetry, along with the distally localized and bisymmetric proliferation surrounded by less proliferative tissue. Mechanical simulations (Hamant et al., Science 2008, Fujiwara2021) and laser cell ablation (Oikawa 2015) showed the distally localized and symmetric proliferation was decoded into a global distribution of the mechanical stress on the tissue, avoiding the local heterogeneity, thereby compressing to smoothen and symmetrize the boundary. In this process, HANABA-TARANU, a transcription factor contributing to the boundary zonation (Zhao et al. 2004), was indispensable to define the positional information of the proliferation by restricting cytokinin-PEAR1 module activity. The patterned proliferation, which tends to sustain the stress in less fluidic tissue like plants (Trinh 2021, Hamant 2012), is thus mechanically suitable to design the organ shape globally, including the symmetric smoothening of the boundaries.

3.2. Introduction

Plant bodies exhibit some form of symmetry in their shapes and arrangements, such as the radial arrangement of shoot organs, so-called phyllotaxis, and their bilateral shapes. Not only in the outward appearances, plants also establish symmetry in their internal tissue organization. At the central part of axial organs including stem and root, plants develop the vascular cylinder (so-

called stele) that consists of the vascular tissue and its surrounding layer, the pericycle (Esau, 1965). Among a vast variety in the arrangement of two conductive tissues, xylem and phloem, in the plant vascular tissues, the roots of most seed plants typically exhibit a radially symmetric vascular organization, with one or more strands of xylem extending towards the periphery, and phloem alternating with the peripheral xylems. While the number of symmetric axes varies among plant species, the *Arabidopsis* root exhibits a simple biradial symmetric (bisymmetric) anatomy (Fig. 3.1A), where a straight line of xylem strand bisects the vascular tissue with forming laterally neighboring procambium, and two phloems are established at the vascular periphery perpendicular to xylem strand (Fig. 3.1B, left).

In general, tissue symmetry is initially defined by a molecular pre-pattern present in the precursor cells, and is further refined during the subsequent growth phase involving cell proliferation and expansion. In the case of *Arabidopsis* root vascular tissue, its bisymmetry is defined at the vascular stem cells, so called initials, where a mutual interaction between two phytohormone, auxin and cytokinin, forms distinct domains for high-level hormonal signaling, which makes domains for xylem and phloem or procambium, respectively. As an output of this hormonal signaling, two functionally antagonistic transcription factors, HD-ZIP III and PEAR, determine the spatial distribution of cell proliferation. PEAR, a mobile transcription factor expressed in protophloem sieve element (PSE) cells in cytokinin-dependent manner, promotes the proliferation at two PSE and their neighboring cells, whereas HD-ZIP III, as a downstream of auxin, repress the proliferation in the inner vascular cells. Furthermore, the PEAR expression and function are restricted peripherally by HD-ZIP III, resulting in the highly centered proliferation around PSE. Despite an extensive progress in our understanding of symmetric tissue zonation coupled with localized proliferation in the vascular tissue, it remains unclear how symmetry is maintained or reinforced at the cellular level during the dynamic process of the vascular development.

In animal systems, the boundaries between different cell types, such as compartment boundaries in the Drosophila imaginal disc, play crucial roles in the pattern formation of proliferating tissues. Once the boundaries are zoned by selector genes in the early tissue, their neighboring groups of cells are kept physically separated during further developmental stages. In addition, the interface of the boundaries is maintained and smoothened at cellular level throughout the organogenesis, leading to further refinement of tissue organization (Dahmann et al., 2011). Recent studies have uncovered that the boundary smoothing is achieved by the oriented mechanical stress and fluidic cell property at the boundary, which deforms the cell geometry locally. Although cell geometrical deformation at the boundary could be assumed to regulate the

plant tissue patterning, including symmetry refinement, so far little is known about how and whether the boundary shape is determined at cellular level in plants, especially in the tissue embed in an organ including the vascular tissue.

Here, I performed geometric analysis of the vascular bundle tissue and revealed that the vascular tissue maintain biradial symmetry and form the smooth xylem-procambium boundary during tissue growth. Simulations incorporating cell proliferation drawn from vascular bundle development identified tissue growth improve the symmetry and smoothen the boundary through compression toward the boundary.

3.3. Materials and Method

Plant materials and growth conditions

We used accession Col-0 as a wild type for analysis of root vascular bundle in *Arabidopsis*. We also used *han-1, wol, wol han-1*, and overexpression HAN for analysis of root vascular bundle.

Imaging and image processing

We determined each position of tricellular junctions in root vascular tissue at the transverse section of the proliferation zone (Fig. 3.1A) by using the Fiji plugin Tissue Analyzer (Aigouy et al., 2010). We used the position of tricellular junctions (vertices) to calculate the boundary roughness, cell aspect ratio, angle of tricellular junctions (Fig. 3.1B), cell number, proliferation position (Fig. 3.3B, C), and cell area (Fig. S3.1). We obtained vascular cell number and area from the transverse sections of the pattern compilation stage (Fig. 3.1A). Since root cells are stacked longitudinally, cell proliferation position was determined by comparing a successive series of transverse sections of a root following earlier studies (Miyashima et al., 2019).

Boundary smoothness indicators

The roughness of the boundary w was quantified by the variance of the distance h_i between vertices on the XP boundary (i=1,・・・, N) and a straight line connecting both the ends (Fig. 3.1B):

$$w = \sqrt{\frac{1}{N}\sum_{i=1}^{N}\left(h_i - \bar{h}\right)^2} \qquad \text{(Eqn. 3.1)}$$

$$\bar{h} = \frac{1}{N}\sum_{i=1}^{N} h_i \qquad \text{(Eqn. 3.2)}$$

We used the normalized roughness of the XP boundary w / L (Fig. 3.1B. 3.3E, 3.4F), and L indicated the average length of cell edges (cell-cell interfaces) on the boundary. N denotes the number of vertices on the boundary (Fig. 3.1C). $\bar{h}$ denotes average distance between the vertices and the ideal boundary line. As a control, the roughness of PSE-PSE cell file was quantified by

the variance of the distance between the vertices on the cell file and a line connecting both the ends (Fig. 3.1B). For the cell aspect ratio, we first fit an approximated ellipse to the cell (Fig. 3.1B), which was defined by the inertial tensor using cell vertices (Alim 2012). The two axes of the ellipse were given by the line passing through the centroid of the cell in the direction of the eigenvector corresponding to the eigenvalue of the tensor (Fig. 3.1B). The cell aspect ratio was calculated by dividing the length of the tangential axis along the boundary by that of the other axis. The angle between three successive vertices (Rudolf 2015) (Fig. 3.1B) was measured and averaged over all of the vertices on the XP boundary or the PSE-PSE cell file.

Statistical analysis

Tukey's honestly significant difference test was performed for Fig. 3.1B, C, 3.3E, J, K, 3.4C, E, S3.4E after confirming a normal distribution by Kolmogorov-Smirnov test, using R. Different letters (a, b, c, d) denote statistically significant differences ($P < 0.05$) among means. The lower and upper hinges and middle lines represent the 25th, 75th, and 50th percentiles. The whiskers denote the minimum and the maximum.

Formulation of tissue-mechanical simulations

The cell vertex model is useful to simulate mechanical deformation of cells in tissues based on the forces acting on each cell, where the cell configurations are described as polygons whose vertices form cell junctions subjected to mechanical force (Honda, 1983; Farhadifar, 2007, Fujiwara 2021). Cells change their shape based on the force balance. The model is represented here by the ordinary differential equations of the position vector of each vertex:

$$\frac{d\vec{r}}{dt} = F_{area\ elasticity} + F_{tension} = -\frac{dE}{d\vec{r}} \qquad \text{(Eqn. 3.3)}$$

$$E = \sum_n c(A_n - A_0)^2 + \sum_{ij} \beta_{ij} L_{ij} \qquad \text{(Eqn. 3.4)}$$

The area elasticity $F_{area\ elasticity}$ is exerted on a vertex i by the cell face n to which the vertex i belongs, while the area of cell A_n approaches the preferred area of A_0. The tension $F_{tension}$ is exerted on a vertex i by the connecting edges between vertices i and j where $F_{tension}$ increases as the edge length between vertices i and j (L_{ij}) increases depending on the cell-wall extensibility β_{ij}. For all cells, we set c=1 μm^{-2}, β_{ij}=0.12 μm of the cell edge between xylem and procambium, β_{ij}=0.15 μm of the edge between PSE and pericycle, β_{ij}=0.08 μm of the edge between pericycle and pericycle or endodermis, and β_{ij}=0.1 μm of the other edge, which reproduced the cell aspect ratio of *Arabidopsis* wild-type cells (Fig. 3.1B, S3.1B). In addition, plant cells undergo plastic deformation by the irreversible cell growth, which has been formulated by multiplication of the excess turgor pressure over yield stress and the cell wall extensibility of cell edge (Lockhart,

1965). In the present model, the plastic deformation was formulated by the irreversible increase of the preferred area A_0 of cells, as described in detail below, instead of the edge length in the Lockhart model (Lockhart, 1965). We integrated the cell vertex model numerically using the Euler method.

Cell division and expansion in simulations

As the initial condition of the vertex model simulations, we used nine initial templates, which were obtained from wild-type roots *in vivo* (Fig. S3.1), for the position, area and vertices shape anisotropy of each cell. For the boundary conditions in the simulations, the vertices at the outside end of endodermis could move freely allowing the vascular tissue to expand until the size of after proliferated vascular tissue (Fig. S3.1C). During the vascular tissue growth, the orientation of the cell division plane was set in a horizontal direction to the XP boundary for PSE, in a vertical direction for PX and in the short axis direction of the approximate ellipse for the procambium cell just before division (Fig. 3.1A, S3.1) (Miyashima 2019), with a small rotational variation following the Gaussian distribution with the s.d. of 0.1 degree. The division plane was set to pass through the geometric center of the dividing cell.

The frequency of cell proliferation (division) in wild-type and han-1 mutant *in silico* was introduced from that *in vivo* (Fig. 3.3D; i.e., twice at PSE/PSE-LN and once at PX per cell in wild-type; four times at PSE/PSE-LN, twice at PX, six times at OPCs, once at IPCs per cell in han-1); The pericycle was set to proliferate once per cell (Fig. S3.1B) and endodermis did not proliferate. The enhanced proliferation in han-1 mutant simulation was additionally introduced following observation (Figs. 3.3D and S3.4B) to above cell proliferation in wild-type, twice per cell in the enhanced simulation at PSE/PSE-LN; once per cell in enhanced proliferation at PX; once per cell in enhanced proliferation at IPCs; five times per OPC cell laterally adjacent to PSE-LN in enhanced proliferation at OPCs. In the simulation of the overexpressing HAN, proliferation frequency at PSE/PSE-LN domain decreased by half that in wild-type, following observation (Fig. 3.4B). To be the same number of each cell type observed *in vivo*, the cycle of cell proliferation set T_0 (arbitrary unit) in PSE, the cycle in PSE-LN was $T_0/2$ hour, and the cycle in pericycle was $3T_0$ hour in wild-type simulation (Fig1D, S1C). In the simulation of han-1 mutant, the cycle of enhanced proliferation at OPC and IPC were set to the same one to PSE cell T_0.

For cell growth, the preferred area A_0 was initially set at the beginning of cell cycle as an average among cells for 180 μm^2 in xylem, 100 μm^2 in procambium, 180 μm^2 in pericycle and 360 μm^2 in endodermis to reproduce the wild-type *in vivo* (Fig. S3.1B). After cell proliferation, cell area grew to the preferred area. The cell area followed a linear growth, $dA_0/dT=97.2\ \mu m^2/T_0$ in vascular cell,

dA_0/dT=38.9 μm^2/T_0*0.25 in pericycle, and dA_0/dT=0, i.e., no growth in endodermis for reproducing the size of cell area *in vivo* (Fig. S3.1B).

Mechanical stress *in silico*

In the simulation, the stress within a tissue was evaluated by the stress tensors used in these papers (Ishihara and Sugimura 2012, Lee and Morishita 2017). The stress tensors are calculated by using the forces loaded on vertices of each cell from Eqn. 3.4. The stress tensor σ (defined as stress tensor σ (B) in Lee and Morishita 2017) was represented diagonalized stress $\begin{pmatrix}\sigma_1 & 0\\ 0 & \sigma_2\end{pmatrix}$, where σ1 and σ_2 ($\sigma_1 > \sigma_2$) are the principal stresses, and the direction of σ1 represented by the angle θ to the XP boundary axis ($0 < \theta < 180$, σ_2: θ+90; Fig. S3.2A). A positive stress magnitude ($\sigma_1+\sigma_2>0$) and a negative one ($\sigma_1 + \sigma_2<0$) represents compressive and a tensile stress, respectively (Fig. 3.4B; compressed (orange), and tensile (blue)). $\sigma_1 - \sigma_2$ represents the stress anisotropy. $\sigma_1 - \sigma_2 = 0$ indicates isotropic stress. The direction of anisotropic stress is the same to the direction of the maximum principal stress (θ). The stress anisotropy is denoted

$$\vec{s} = \big((\sigma_1 - \sigma_2) * cos\theta,\ (\sigma_1 - \sigma_2) * sin\theta\big).$$ $|\vec{s}|$=0 indicates isotropic stress.

The tissue stress anisotropy $\vec{S}$ in the domain is defined by the summation of the stress anisotropy of cells in the domain. Tissue stress anisotropy is denoted by the composite vector:

$$\vec{S} = \sum_i \vec{s_i} = (\sum_i(\sigma_1 - \sigma_2)_i * cos\theta_i\ ,\ \sum_i(\sigma_1 - \sigma_2)_i * sin\theta_i) \qquad \text{(Eqn. 3.5)}$$

where the angle becomes twice since the stress works in both directions. The degree of the tissue anisotropy is defined by

$$|\overrightarrow{S}|/\sum_i|\vec{s_i}| = |\vec{s_1} + \vec{s_2} + \cdots + \vec{s_n}|\ /(|\vec{s_1}| + |\vec{s_2}| + \cdots + |\vec{s_n}|),\ \sum_i|\vec{s_i}| \neq 0 \text{(Eqn. 3.6)}$$

where the magnitude of the composite vector is normalized by the sum of the magnitudes of the stress anisotropy of the cells in the domain ($i = 1 \ldots n$). If all anisotropic stress of cells is in the same direction, the tissue anisotropy is 1. The variance of the directions of cell anisotropic stress increases, the tissue anisotropy is close to 0 (isotropic). $\sum_i|\vec{s_i}| = 0$ is isotropic stress. The direction of tissue stress anisotropy is defined by an angle between the composite vector ($\tan^{-1}(\sum_i(\sigma_1 - \sigma_2)_i * sin\theta_i\ /\sum_i(\sigma_1 - \sigma_2)_i * cos\theta_i$) relative to the XP boundary. The angle 90 degree is the vertical direction of stress in the domain. The angle 0 degree is the horizontal direction of stress in the domain.

Laser ablation

Laser ablation of cell was performed by the femtosecond laser (Oikawa 2015), upon ablating a xylem, pericycle or endodermal cell *in vivo*.

3.4. Result

Arabidopsis root vascular boundary is smooth and bisymmetric at the cell level

The vascular tissue of plants is composed of three cell types, xylem, phloem, and procambium/cambium (Esau 1965). Those cells are arranged bi-symmetrically in the *Arabidopsis* primary root, where two protophloem sieve element (PSE) cells are formed at the periphery perpendicular to a single strand of xylem cell files (Fig. 3.1A). Intervening procambium tissues are established between these conductive tissues to form the distinct boundary to the xylem. To evaluate the smoothness of the xylem-procambium (XP) boundary at the cell level, we first quantified several indicators following the studies in the animal tissue boundaries (Fig. 3.1B) (Landsberg et al., 2009). Indeed, the roughness of cell arrangement at the XP boundary was significantly lower than that along the PSE-PSE cell files as a control (Fig. 3.1B), indicating a similar level (0.4-0.6) to the smooth boundaries in the animal epithelium (Rudolf et al., 2015 Umetsu et al., 2014 Landsberg et al., 2009 Aliee et al., 2012). The angle of tricellular junctions at the boundary was larger than that of the PSE-PSE cell files (Fig. 3.1B). Moreover, the shape of cells adjacent to this boundary, metaxylem cells (MXs), and procambial cells, were more anisotropic tangentially to the boundary (i.e., long horizontal) than that of the procambium cells not adjacent to the boundary (cell aspect ratio, Fig. 3.1B), together indicating a characteristic smoothness at the cellular level.

The XP boundary develops along with the vascular tissue growth, in which two PSEs and their lateral neighboring cells (PSE-LN) repeatedly proliferate in a bisymmetric pattern (Fig. S3.4B), producing the procambial cells (Miyashima et al. 2019). In contrast, the procambium nearby the XP boundary hardly proliferates, and each protoxylem cell (PX) proliferates only once tangentially to form MX inward, together indicating a distally localized and bisymmetric proliferation to the boundary (Miyashima et al. 2019). During the proliferation, notably, the MXs transited from long vertical to the long horizontal shapes (Fig. S3.1A, C). Moreover, the arrangement of the tricellular junctions on the XP boundary relative to the position of two PSEs improve the bisymmetry (Fig. 3.1C), together suggesting that the proliferation may force to smoothen and symmetrize the boundary.

Bisymmetry of mechanical stress field emerged under the patterned proliferation

The proliferative patterns produce the mechanical stress on the tissue promoting the morphogenesis (Hamant et al., Science 2008, Fujiwara 2021), whereas the role of distally localized and symmetric proliferation remains unclear. To this end, we performed a simulation of vascular tissue growth by using the vertex model in which cell growth and proliferation cause to

mechanically deform a multicellular tissue (e.g., studied in shoot (Hamant 2008) and root meristems (Fujiwara 2021); Methods). Here we used the realistic geometries of the initial cells (i.e., position, area, and vertices of each cell; Fig. 3.1A) *in vivo* as an initial template (Fig. S3.1C). Then the quantified proliferation frequency (Miyashima et al. 2019; Method) and area growth (Fig. S3.1B) during the proliferative phase *in vivo* (Fig. 3.1A) were incorporated into each vascular cell *in silico* to simulate the tissue growth within its surrounding pericycle and endodermis (Fig. 1D). Despite the variability of cell area and arrangement in the initial templates, shown *in vivo* (Fig. S3.1A, C), the incorporation of the predominant proliferation (at PSE/PSE-LN and PX; Method) developed the smooth and bisymmetric XP boundary *in silico* (Fig. 3.1B, C, S3.1C), quantitatively accounting for the roughness, angle, cell aspect ratio and tissue symmetry *in vivo* (wild type in Fig. 3.1B, C). Therefore, the mechanical simulation demonstrated that the distal and bisymmetric proliferation centered around two PSEs, the pattern observed in the wild-type root *in vivo*, is sufficient for the symmetric smoothing of the XP boundary.

Next, we investigated the mechanical stress loaded on each cell. Since vascular tissue proliferates more frequently than the surrounding pericycle and endodermis (Fig. S3.1B) (Miyashima et al., 2019), the surrounding tissue spatially confines the vascular tissue growth so that the stress appears to be compressive in simulations (Fig. S3.2A). We can indirectly measure the stress by anisotropic deformation of tissue in response to a mechanical perturbation on a cell (Sugimura et al., 2016, Trinh et al., 2021). Indeed, upon ablating a pericycle or endodermal cell *in vivo* by using the femtosecond laser (Oikawa et al., 2015; Methods), the vascular cells neighboring to the ablated cell expanded outwardly (Fig. S3A; pericycle n=9, and endodermis n=3), confirming the compression by the surrounding tissue.

Notably, as proliferation progressed in the simulation, the compression at the central domain of vascular tissue (MXs and the internal procambial cells [IPCs]) became directed vertically to the XP boundary (Fig.3.2A, S3.2D), whereas the compression at the peripheral PX was always directed tangentially to the boundary (Fig. 3.2A, S3.2D). The bisymmetric distribution of the stress was consistent with the bisymmetric pattern of proliferation (Fig. 3.1A, 3.2C, S3.4B). Upon ablating an MX *in silico*, following the vertical compression, the surrounding procambium cells selectively expanded to occupy the space left by the ablated cell, whereas the surrounding xylem cells hardly expanded (Fig. 3.2D). Upon ablating a pericycle cell adjacent to PX *in silico*, conversely, following the tangential compression at PX, the surrounding PX and procambium cells selectively expanded, but the surrounding pericycle cells hardly did (Fig. 3.2E). Intriguingly, we verified the cell-specificity of the anisotropic compression *in vivo* by the femtosecond laser ablation of a central MX (Figs. 3.2F and S3.3C; n=9) or a pericycle cell

adjacent to PX (Figs. 3.2G and S3.3B; n=3). Taken together, both *in silico* and *in vivo* results revealed the bisymmetric distribution of compression stress under the distally localized and bisymmetric proliferation.

To examine the origin and role of the bisymmetric stress distribution, we manipulated the proliferation pattern *in silico*. The reduction of proliferation centered around two PSEs weakened the vertical compression on the IPCs and even changed the direction of stress tangentially at MXs (PSE/PSE-LN↓ in Fig. 3.2B, C, S3.2C). As a result, the MXs and IPCs deformed to the long vertical shape (indicated by the low aspect ratio in Fig. 3.3J), unlike the long horizontal shape in the wild-type. The bisymmetry of the XP boundary also weakened (Fig. 3.3K). These results predicted that the distally localized and bisymmetric proliferation governs the bisymmetric distribution of the compression stress to symmetrically smoothen the boundary.

HAN is required for the distally localized and bisymmetric proliferation and symmetric smoothing of the boundary

The bisymmetric arrangement of vascular cells is roughly initiated (Fig. 3.1A, C) through a mutual interaction with auxin and cytokinin that first defines the domain of xylem or procambium and phloem laterally neighboring xylem, respectively (Fig. 3.3A) (Bert 2014, Miyashima 2019). The following proliferation centered around two PSEs is promoted by cytokinin and its downstream mobile PEAR transcription factors, which is transcribed only at PSEs (Miyashima 2019). This PEAR expression and function are restricted distal to the boundary by HD-ZIP III transcription factors, downstream of auxin signaling (Izhaki and Bowman 2007); However, it remains unclear how the proliferation and the underlying PEAR expression are suppressed in the lateral cells, such as the procambium laterally adjacent to PSE-LN.

To identify the factors determining the proliferation pattern to form the smooth boundary, we searched the transcription factors abundantly expressing the vascular stem cells and found that HANABA-TARANU (HAN), a B-GATA transcription factor, is expressed from the initial cells to the proliferative phase (Fig. 3.3B). HAN regulates the zonation of boundary in embryo and shoot (Zhao et al., 2004), but its role in root remains unknown. Compared with wild-type roots where proliferation mostly occurs at PSE and PSE-LN (Fig. 3.3D) (Miyashima2019), we found that the loss-of-function mutant han-1 significantly enhanced proliferation not only at the PSE/PSE-LN but also at other domains, including the outer procambial cell (OPC) adjacent to PSE-LN, the IPC, and PX (Fig. 33.D), resulting in the increased vascular cells (Fig. 33.C). Moreover, the normalized S.D. of PSE-LN and OPC number among four domains separated by

the XP boundary and the PSE-PSE cell file was more significant in han-1 than wild-type (Fig. S3.4B), indicating an enhanced proliferation asymmetrically.

Notably, han-1 mutant significantly increased the roughness of the XP boundary and decreased the cell aspect ratio (Fig. 3.3E, J), and weakened the tissue bisymmetry (Fig. 3.3K), despite proper specification of xylem cells (Fig. 3.3A, S3.4A). The simulation incorporating the enhanced proliferation pattern in han-1 mutant (Fig. 3.3D) quantitatively reproduced the cell geometry for both the boundary roughening and asymmetry *in vivo* (Fig. 3.3E, F, J, K). We investigated the position-specific effect of the enhanced proliferation on the boundary *in silico*; The introduction of proliferation at IPC (Fig. 3.3G), which is proximal to the boundary and is mitotically quiescent in wild-type (Fig. 3.3D), roughened the boundary (Fig. 3.3E). Additionally, the induction of the asymmetric proliferation at OPC, a defect in han-1 mutant (Fig. 3.3D and S3.4B), roughened the boundary at the side of the enhanced proliferation (Fig. 3.3E, G) and weakened the tissue symmetry (Fig. 3.3K). In both cases, the direction of compression stress became heterogeneous among the MXs and IPCs (Fig. 3.3H, S3.2C), indicating the distally localized and bisymmetric proliferation centered around two PSEs contributes explicitly to the bisymmetric compression stress directed to the XP boundary. Finally, the XP boundary in the simulation enhancing proliferation at PSE/PSE-LN domain did not affect the roughness (Fig. 3.3E), xylem cell shape (Fig. 3.3J), and bisymmetry of the stress field among the MXs and IPCs (Fig. S3.2B), while that at PX only affected the adjacent MX in the stress direction (Fig. S3.2B) resulting in the long vertical shape (Fig. 3.3J). These results indicate that HAN contributes to the bisymmetric smoothening of the XP boundary by bisymmetrically restricting the proliferation domains centered around two PSEs.

HAN defines the patterned proliferation by repressively restricting the domain of cytokinin-PEAR1 activity

To reveal how HAN regulates the proliferation pattern, we examined the expression of known regulators in han-1 mutant. Whereas one of five HD-ZIP III genes, CNA was normally expressed (Fig. S3.4C), the spatial expression of PEAR1 transcription became laterally expanded from the initial stage to the proliferative phase in han-1 mutant (Fig. 3.4A). In addition, cytokinin response reporter pARR5::RFPer, whose expression is suppressed in the xylem in wild-type (Bert 2014, Miyashima 2019), was expressed in the whole vascular initials (Fig. 3.4A). However, the expression of those reporters after proliferation became restricted into PSE and procambium, respectively (Fig. 3.4A), as observed in wild-type roots (Fig. 3.4A), suggesting the repressive role of HAN in cytokinin signaling during vascular proliferation. The intracellular signaling of

cytokinin is mediated by His-Asp phosphorelay, which culminates the phosphorylation of B-type response regulators to activate the transcription of downstream genes (Ari 2006). Our transient assay using a cytokinin reporter, TCS::LUC (Bruno 2008), demonstrated that HAN inhibits the transcriptional activity of B-type response regulator ARR1 (Fig. 3.4C) and its constitutively active form ARR1 delta DDK (Fig. S3.4E), in a dose-dependent manner, suggesting that HAN represses the cytokinin response by competing with B-type response regulators at the transcriptional level. Since both the initial tissue bisymmetry (Fig. 3.3A) and proliferation require the cytokinin signaling (Bert 2016), a severe reduction of cytokinin signaling, like a cytokinin receptor mutant wooden-leg (*wol*), leads to the radially symmetric tissue geometry without proliferation (Miyashima 2019) (Fig. 3.4A). We found that introducing han-1 mutation into *wol* restored the vascular cell number to the wild type (Fig. 3.3C, 3.4A) with the expression of PEAR at the vascular peripheral in an almost radially symmetric manner, again highlighting the repressive role of HAN in cytokinin signaling in vascular proliferation. Notably, the proliferation occurred distally but radially symmetrically in wol han-1 mutant leading to the less anisotropic shape of vascular cells (Fig. S3.4F), supporting the long horizontal shape of the central cells (IPC and MX) in wild-type (Fig. 1B) requires the distally localized and bisymmetric proliferation.

In addition, the induction of HAN-overexpression under the vascular specific CRE1 promoter immediately attenuated the cytokinin response (Fig. S3.4D), and further induction led to the lack of proliferation in the vascular tissue (Fig. 3.4D, S3.4D) similar to plants lacking cytokinin biosynthesis or signaling components (Ari 2000, Bert 2014). In this transgenic line, we found that the 48hr-induction of HAN-overexpression resulted in decreased procambium proliferation, while xylem cell number was equal to the wild-type (Fig. 3.4B). Therefore, we experimentally tested the theoretical prediction that a moderate frequency of the distally localized and bisymmetric procambium proliferation symmetrically smoothen the boundary (Fig. 3.2C) by quantifying the cell geometry in the overexpressing HAN. Due to the decreased proliferation, the MX cells consistently expanded vertically to the XP boundary, indicating a long vertical shape unlike wild-type (Fig. 3.4E). In the root possessing six cells in the xylem strand, which infrequently appeared in the wild-type, we found that the MX cells consistently further expanded vertically (Fig. 3.4E). At the same time, notably, the roughness of the XP boundary was significantly higher (Fig. 3.4E), and the bisymmetry was significantly lower than wild-type (Fig. 3.4E), verifying the theoretical prediction. Collectively, our data concluded that HAN defines the spatial pattern of proliferation frequency by restricting the activation position of the cytokinin-PEAR1 module with its repressive action on cytokinin signaling, which is indispensable for the bisymmetric smoothing of the boundary.

3.5. Discussion

In summary, our research has revealed that spatially localized proliferation produces a global order of the anisotropic stress, thereby symmetrically smoothing the tissue boundary (Fig. 3.1, 3.2). Previous works have highlighted that the dual role of cytokinin in vascular tissue formation, in which cytokinin initially defines the bisymmetric zonation by specifying procambial tissues nearby the xylem, later on, promotes the proliferation through activating the PEARs at the most distal procambial cells, PSEs (Miyashima 2019). However, whether and how the tissue bisymmetry progresses during tissue growth remains elusive. Here we have discovered that these cytokinin actions, with further spatially fine-tuned by HAN (Fig. 3.3, 3.4), are decoded into the directed compression towards the central xylem (Fig. 3.2) that promotes the bisymmetric smoothness of the XP boundary (Fig. 3.1). Since plant tissue lacks the cell rearrangement, unlike animal tissue due to the rigid cell wall, the proliferation (Fig. 3.2A) and the compaction from the surrounding tissue (Fig. S3.2A) tend to sustain the stress in tissue (Trinh 2021, Hamant 2012). Proliferation at the proximal position causes the heterogeneity of the stress direction among the neighboring cells (Figs. 3.3G-I and S3.2A, C; IPC↑), while the asymmetric proliferation at the distal one causes the asymmetric distribution of the compression (Figs. 3.3G-I and S3.2A, C; OPC↑). Although it is currently infeasible to measure the heterogeneous and asymmetric stress distribution *in vivo*, both proliferation defects, observed in han-1 (Fig. 3.3D), affected the boundary smoothness and symmetry (Figs. 3.3E, J, K). Therefore, the directed bisymmetric compression toward the boundary requires the restricted proliferation at the distal and symmetric domains to the boundary. HAN fulfills this requirement by restricting the domain of cytokinin-PEAR activity (Fig. 4.3A). Once the distal and symmetric proliferative pattern is defined, the stress compresses the boundary in a spatially homogeneous direction (Fig. 3.2A and S3.2A, C; WT). Such stress distribution is supported by the Gauss theorem in elastic mechanics that the direction and strength of the stress caused by a force perturbation at a point source (corresponding to each proliferation event at the PSE) spatially decreases and becomes homogenized as it goes away from the position of the perturbation (Fig. 3.2C) (A. E. H. Love, 1927). Therefore, the global order of the anisotropic stress (Fig. 3.2A) decoded from the distal and symmetric proliferation is mechanically suitable to smoothen and symmetrize the boundary in less fluidic tissue like plants.

The anisotropic stress at the boundary contributed to its smoothness in animal tissue, while the anisotropy locally appears due to the boundary-specific change of cell-cell adhesion strength or cell contractility (Umetsu 2014). The local production of the anisotropic stress also contributes to the plant morphogenesis (Enrico coen 2017, Hamant 2018); for example, auxin influences the cell wall extensibility via the intracellular polarization of the efflux carrier PIN and

the cortical microtubules in shoots and roots (Barro 2019, acid growth;Arsuffi 2017, Barbez 2017). Interestingly, auxin is transported towards the xylem from neighboring procambial cells (Bishopp 2011) in the same direction as the compression stress toward the boundary (Fig. 3.2). A future study is whether a boundary-specific change of the wall extensibility and the distal and symmetric proliferation contributes synergistically to smoothing the XP boundary.

The bisymmetry of the XP boundary (Fig. 3.1A, D) is transformed to a radially symmetric shape during the secondary growth, where proliferation occurs proximal to the boundary (Smetana et al., 2019; Ye et al., 2021), in an opposite manner to the primary growth (Miyashima 2019) (Fig. 3.3D). In addition, the surrounding endodermis is peeled-off from the root surface (Nieminen 2015), suggesting less compaction on the growing vascular tissue than the primary growth (Fig. 3.2F, G, S3.3). It is also curious to investigate whether the patterned proliferation in the secondary growth produced anisotropic stress, thereby smoothening the boundary. Analyzing how the patterned proliferation affects the cell geometry in many biological systems accelerates our understanding to design principles for the organ shape, including the smooth and symmetric boundary.

3.6. Figures

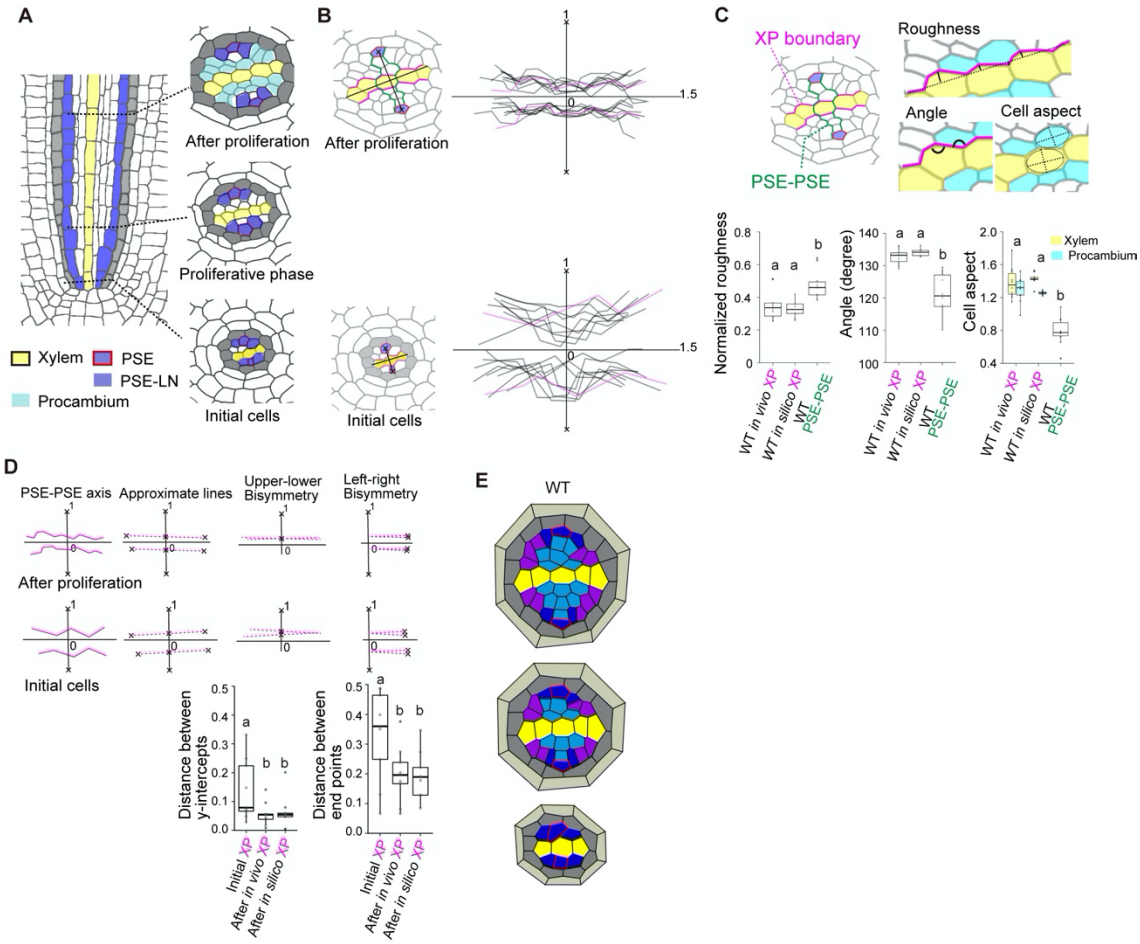

Fig. 3.1 *Arabidopsis* root vascular boundary is smooth and symmetric at the cell level

(A) Vascular tissue growth of *Arabidopsis* wild-type primary root. Transverse (left) and longitudinal sections (right).

(B) Schematic for three indicators of the cell geometry at the XP boundary (magenta line) and PSE-PSE cell files (green line; a negative control) after proliferation (upper); the roughness of the boundary, angle of the tricellular junctions on the boundary and aspect ratio of xylem (yellow; bottom right) and inner procambial cell (IPC; cyan) adjacent to the boundary. Sample number n=10 for XP boundary and PSE-PSE (control) *in vivo*. n=9 for XP boundary *in silico*. Tukey's honestly significant difference test was performed (Methods).

(C) The bisymmetry of the XP boundary relative to two PSE positions after proliferation and initial cells (left). To quantify the bisymmetric arrangement, we set a rectangular coordinate system normalized by half the distance between two PSEs; the Y-coordinate passes through the geometric center of the two PSEs whose midpoint is the origin. Then, bisymmetric transformation

relative to the Y-axis was applied to each quadrant. For the tricellular junction positions on the XP boundary on each quadrant, we performed the linear regression to get the slope and y-intercept (top panels) and calculated S.D. as indicators for the bisymmetry (bottom). Samples were identical to B.

(D) Representative time course of the mechanical simulation of tissue growth, started from an initial template measured *in vivo* (Fig. S3.1D).

Colors denote the cell types: xylem (yellow), PSE (blue with red frame), PSE-LN (blue), pericycle (gray), and endodermis (light gray); Procambium was shown in cyan in A, while IPC and outer procambial cell [OPC] were in light blue and magenta, respectively, in D.

The samples of root were prepared and imaged by S. Miyashima.

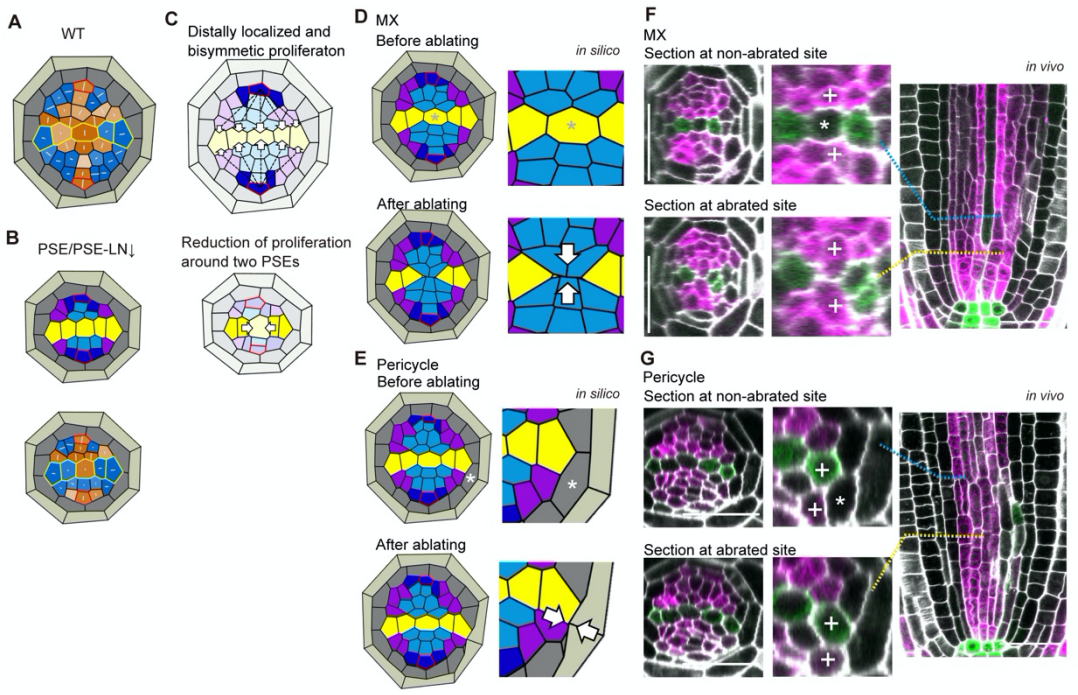

Fig. 3.2 Bisymmetry of mechanical stress field emerged under the patterned proliferation

(A) Compressive stress loaded on each vascular cell *in silico* corresponding to Fig. 1D. The strength is represented by the length of white line in each cell. Color represents the stress direction relative to the XP boundary (Method); vertical (orange) and tangential (blue), shown in the inset. **(B)** Reduced proliferation around PSE (PSE/PSE-LN↓) (top panel) and the strength and direction of compressive stress *in silico* (bottom panel).

(C) Schematic summary for stress distribution for wild-type (top) and the reduced proliferation (bottom), indicated by the stress (arrows) caused by proliferation (at PSEs [dashed line] in top; at xylem in bottom).

(D-G) Indirect measurement of the stress by ablating a MX (D, F) or pericycle cell adjacent to PX (E, G) *in silico* (D, E) and *in vivo* (F, G). Tissue (left) and the magnified view surrounding the ablated cell (right) before (top) and after the ablation (bottom) *in silico* (D, E). Transverse section (left) and the magnified view surrounding an ablated cell (center) at the ablation (bottom; yellow in the longitudinal section in right) and at an upper site (top; cyan in right) *in vivo* (F, G). Auxin (pIAA2; green) and Cytokinin (pARR5; magenta; F, G).

The samples of laser ablated root were prepared and imaged by S. Miyashima

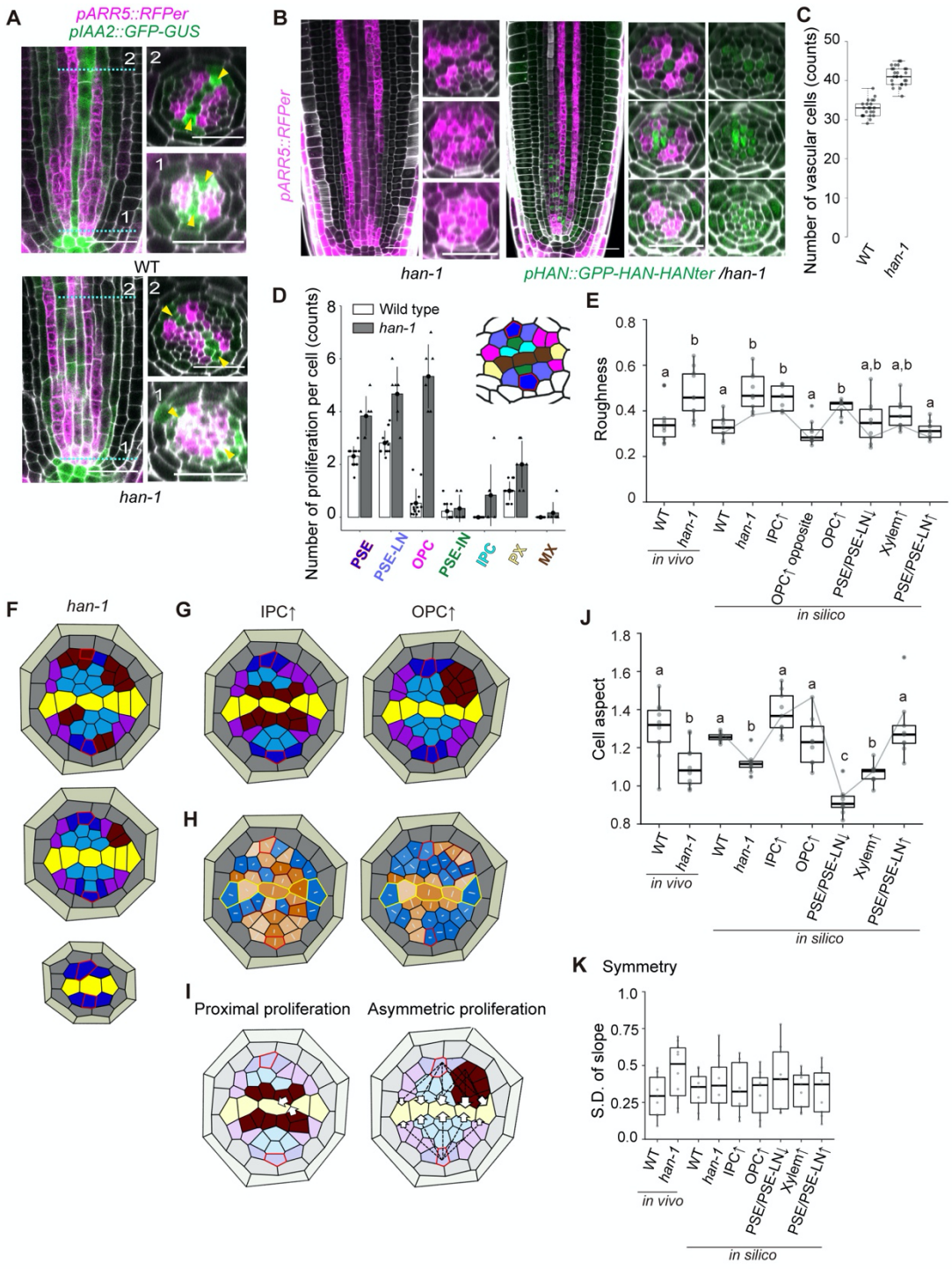

Fig. 3.3 HAN controls the boundary smoothness and proliferation pattern

(A) Auxin (pIAA2; green) and Cytokinin (pARR5; magenta) expression at the initial phase (1; right bottom) and after proliferation phase (2; right top) in wild-type (WT) and han-1. Protoxylem (yellow arrow). Scale bars: xxμm.

(B) HAN (pHAN; green, right) and Cytokinin (pARR5; magenta, left and right) expression in han-1 mutant.

(C) Number of vascular cells in wild-type (n=X), han-1 (n=X), wol (n=X), and wol han-1 mutant (n=X).

(D) Proliferation frequency at each vascular domain, indicated by colors in the inset, in wild-type (n=13) and han-1 (n=6). The error bars represent the S.D. The wild-type data was obtained from Miyashima et al. (2019) Nature.

(E) The roughness of the XP boundary *in vivo* (wild-type and han-1) and *in silico* (wild-type, han-1, and several types of enhanced or suppressed proliferation). Wild-type data set *in vivo* is identical with that in Figure 3.1B. OPC and OPC opposite *in silico* denote the either side of XP boundary in presence and absence of the enhanced proliferation, respectively. Tukey's honestly significant difference test was performed (Methods).

(F) Simulated time course for the enhanced proliferation (brown) in han-1 mutant, starting from an initial template of wild-type measured *in vivo* (Fig. S3.1C). Colors are the same as Fig. 3.1D.

(G) Each of the enhanced proliferation (denoted by IPC↑ and OPC↑; brown) observed in han-1 (D) was additionally induced into the wild-type simulations (Fig. 3.1D).

(H) The strength and direction of anisotropic on each vascular cell in simulated tissue (IPC↑ and OPC↑).

(I) Schematic summary for the stress distribution caused by the proximal (left) and asymmetric (right) proliferation (brown).

(J) Aspect ratio of xylem cells.

(K) Symmetrical indicator of the s.d. of the slope of linear regression of the XP boundary.

Sample number n=10 *in vivo* (wild-type and han-1 for each) and n=9 *in silico* (wild-type, han-1, and five types of the enhanced proliferation for each) in E, J and K. Color coding in F, G and H are identical with Figure 3.1D and Figure 3.2A, respectively.

The samples of root in wild-type and han-1 mutant were prepared and imaged by S. Miyashima

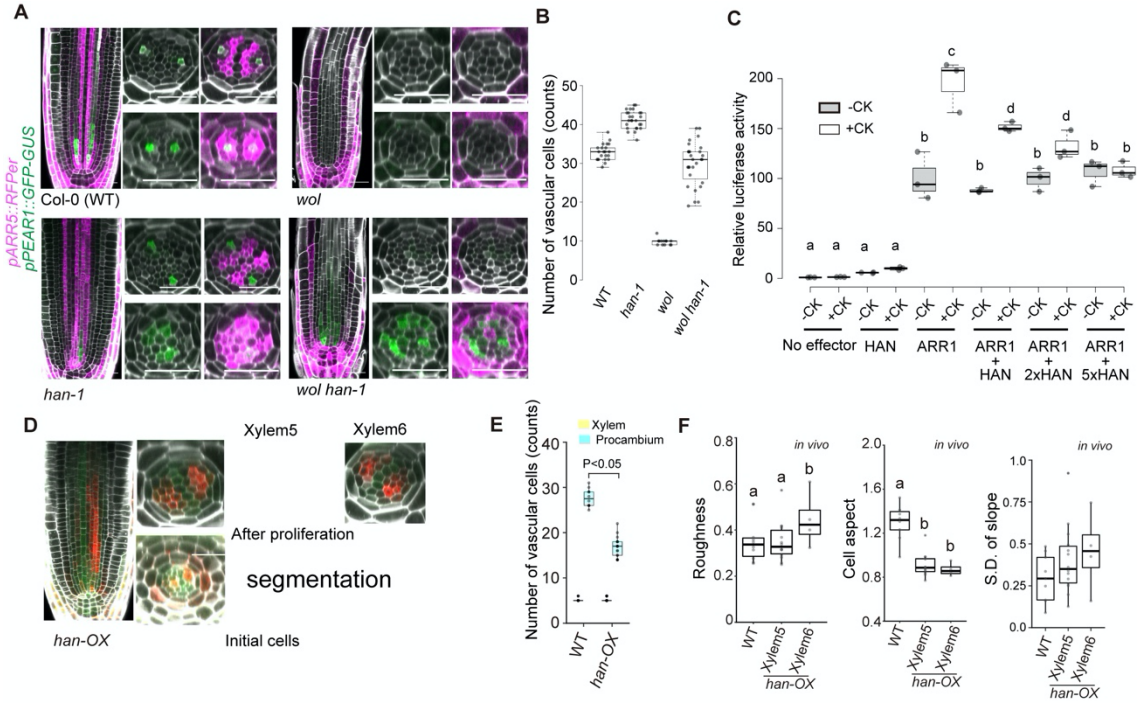

Fig. 3.4 Han defines the spatial pattern of proliferation frequency by tuning the cytokinin-PEAR distribution

(A) Cytokinin (pARR5; magenta) and PEAR1 (pPEAR1; green) expression in wild-type, han-1, wol and wol han-1 mutants.

(B) Number of vascular cells in wild-type (n=X) and overexpression HAN (han-OX;n=X) . t-test was performed after confirming a normal distribution by Kolmogorov-Smirnov tests.

(C) The relative luciferase activity.

(D) The longitudinal and transverse section of vascular tissue of overexpression HAN.

(E) The XP boundary roughness, xylem cell aspect ratio and the s.d.of slope for the bisymmetry. The overexpression HAN (han-OX) is shown for the boundary having five (Xylem5; n=14) and six (Xylem6; n=4) xylem cells. Tukey's honestly significant difference test was performed for the XP boundary roughness and xylem cell aspect ratio (Methods). Wild-type data was identical to Figure 3.1B.

The samples of root in wild-type, han-1, wol, wol han-1 mutant, and overexpression HAN were prepared and imaged by S. Miyashima

3.7. Supporting figures

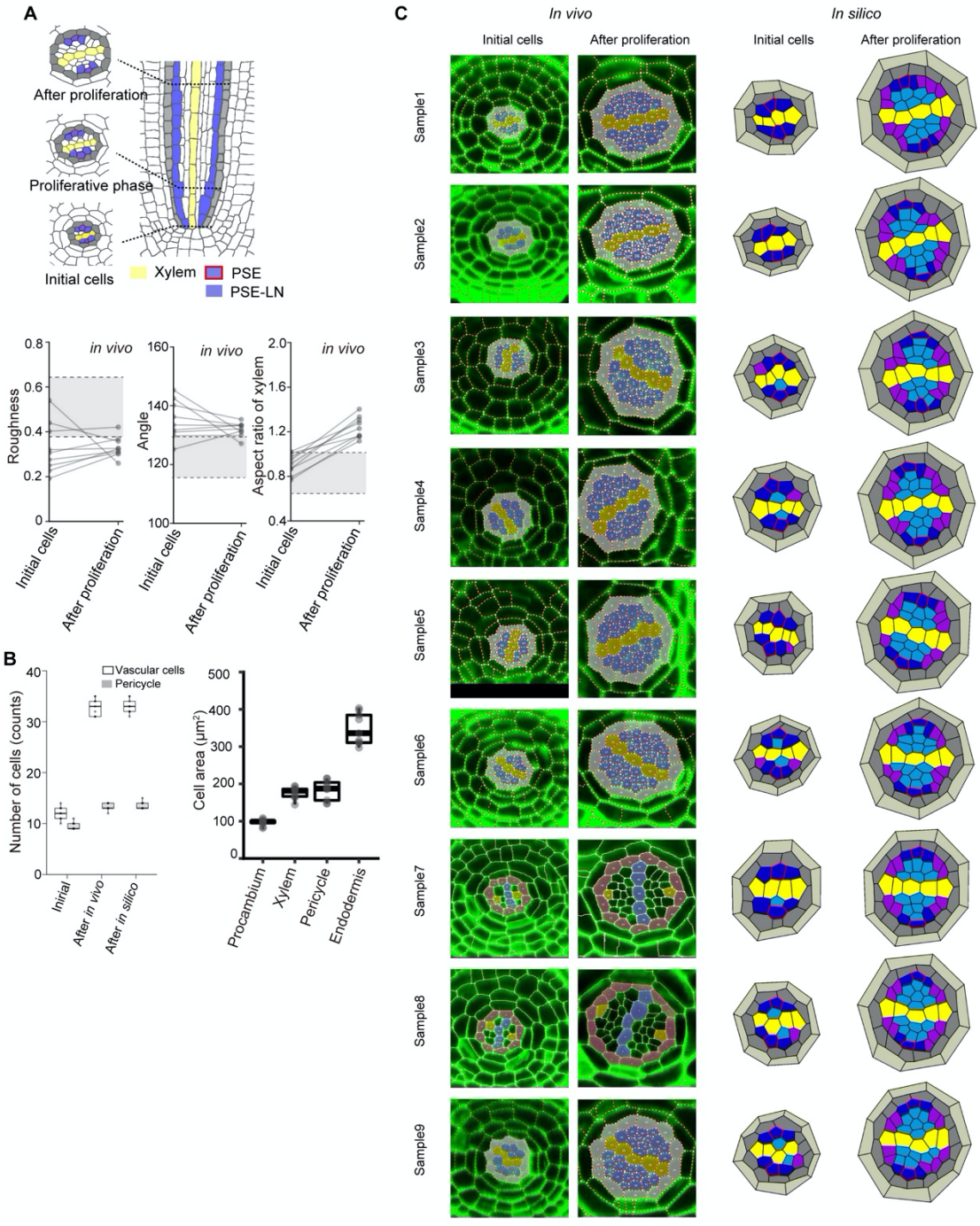

Fig. S3.1 Supporting Figure for Fig. 3.1.

(A) The roughness (left panel), tricellular angle (center panel) and xylem cell aspect ratio (right panel) at the initial cell templates (initial cells; n=9) and the pattern completion templates (after proliferation; n=9) *in vivo* shown in C. Grey region represents the value of PSE-PSE cell files

after proliferation in wild-type (Fig. 3.1C). For the roughness, fraction of the samples in the gray region decreased from 33% of the initial cells to 11% of the samples after proliferation.
(B) The number of vascular cells *in vivo* (n=9) and *in silico* (n=9). The vascular cell area *in vivo* (n=9). The angle and aspect ratio of xylem *in vivo* and *in silico*.
(C) Nine pairs of *in vivo* and *in silico* samples at the initial cell and after the pattern completion, used for A and B.
The samples of *in vivo* root were prepared and imaged by S. Miyashima

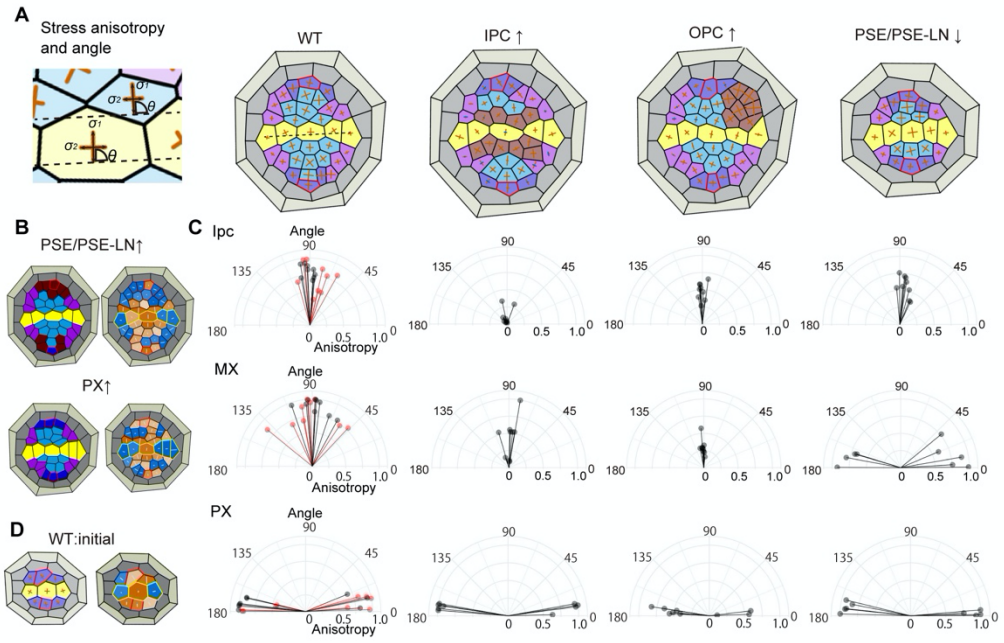

Fig. S3.2 Mechanical stress in simulated tissue

(A) Mechanical stress anisotropy (black arrow in left) and its angle (arc in left) on each cell in wild-type (WT; Fig. 3.1D), enhanced proliferation at IPC (Fig. 3.3G, left), that at OPC (Fig. 3.3G, right), and reduced proliferation at PSE/PSE-LN (B, bottom) *in silico*. Colors of line represent the stress magnitude; compressive (orange), and tensile (blue).

(B) The simulated tissue of PSE/PSE-LN↑ (top) and PX↑ (bottom) and the direction of compressive stress in each vascular cell. Color codings are identical with Figure 3.1D and Figure 3.2A, respectively.

(C) Each solid bar indicates the stress anisotropy (Eqn. 3.6; Method) and its angle averaged among IPC cells (top), among MX cells (center) and among PX cells (bottom) in a simulated tissue of WT, enhanced proliferation at IPC, that at OPC and suppressed proliferation at PSE/PSE-LN (after proliferation, black; initial cell, red).

(D) Mechanical stress anisotropy and the direction of compressive stress in wild-type initial cells.

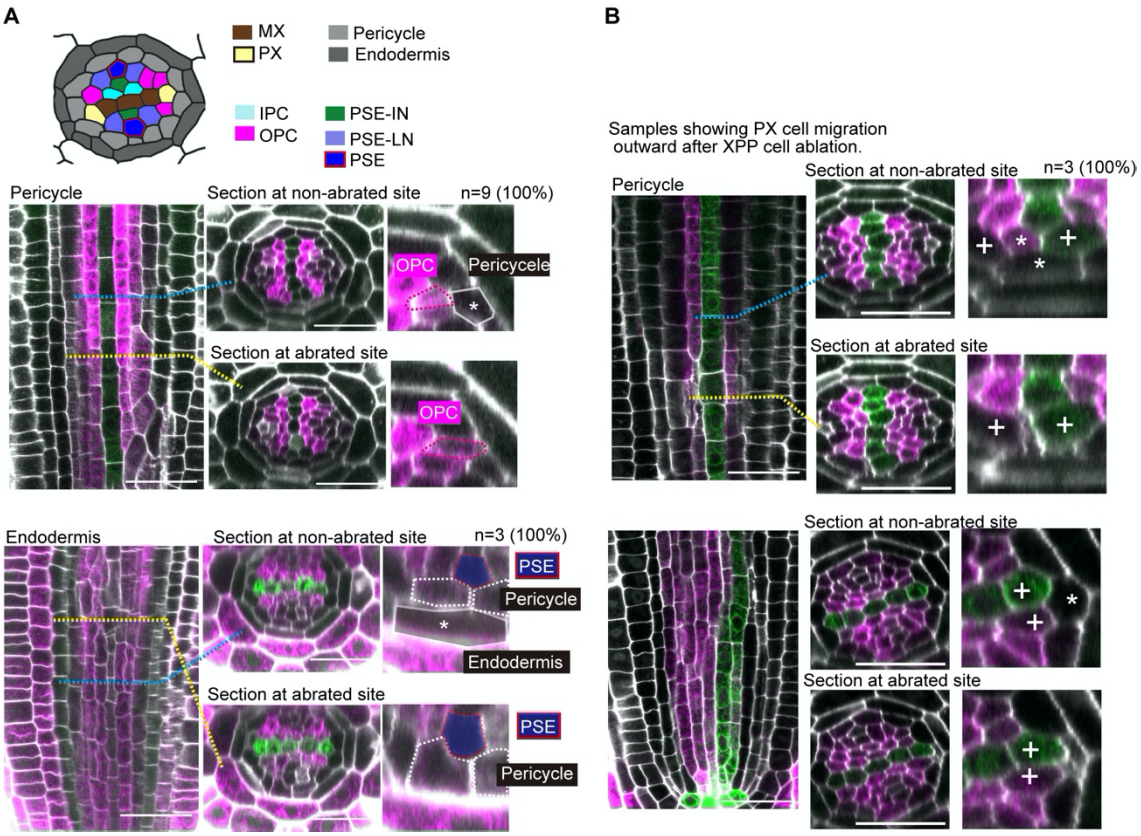
A
MX
PX
Pericycle
Endodermis
IPC
OPC
PSE-IN
PSE-LN
PSE
Pericycle
Section at non-abrated site
n=9 (100%)
OPC
Pericycele
Section at abrated site
OPC
Endodermis
Section at non-abrated site
n=3 (100%)
PSE
Pericycle
Endodermis
Section at abrated site
PSE
Pericycle
B
Samples showing PX cell migration
outward after XPP cell ablation.
Pericycle
Section at non-abrated site
n=3 (100%)
Section at abrated site
Section at non-abrated site
Section at abrated site

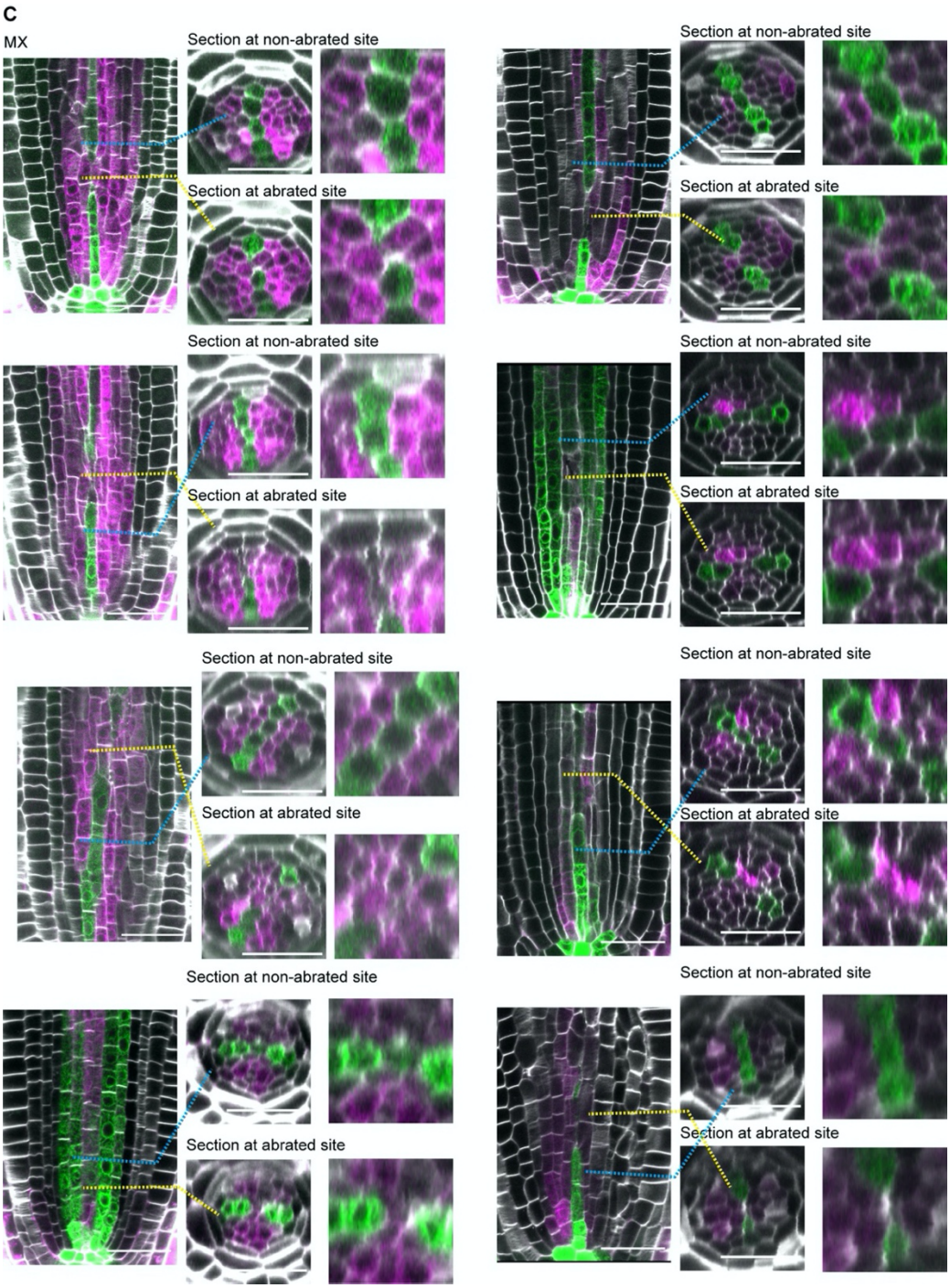

Fig. S3.3 Supporting Figure for Fig. 3.2F, G

Indirect measurement samples of stress by ablating an endodermis or pericycle not adjacent to PX (A), a pericycle adjacent to PX (XPP; B) and a MX (C), other than those shown in Figure 3.2F, G. Transverse section (center) and the magnified view surrounding an ablated cell (right) at the ablation (yellow in longitudinal section in left) and at an upper (lower) site (cyan in left). Auxin (pIAA2; green) and Cytokinin (pARR5; magenta). The samples of laser ablated root were prepared and imaged by S. Miyashima

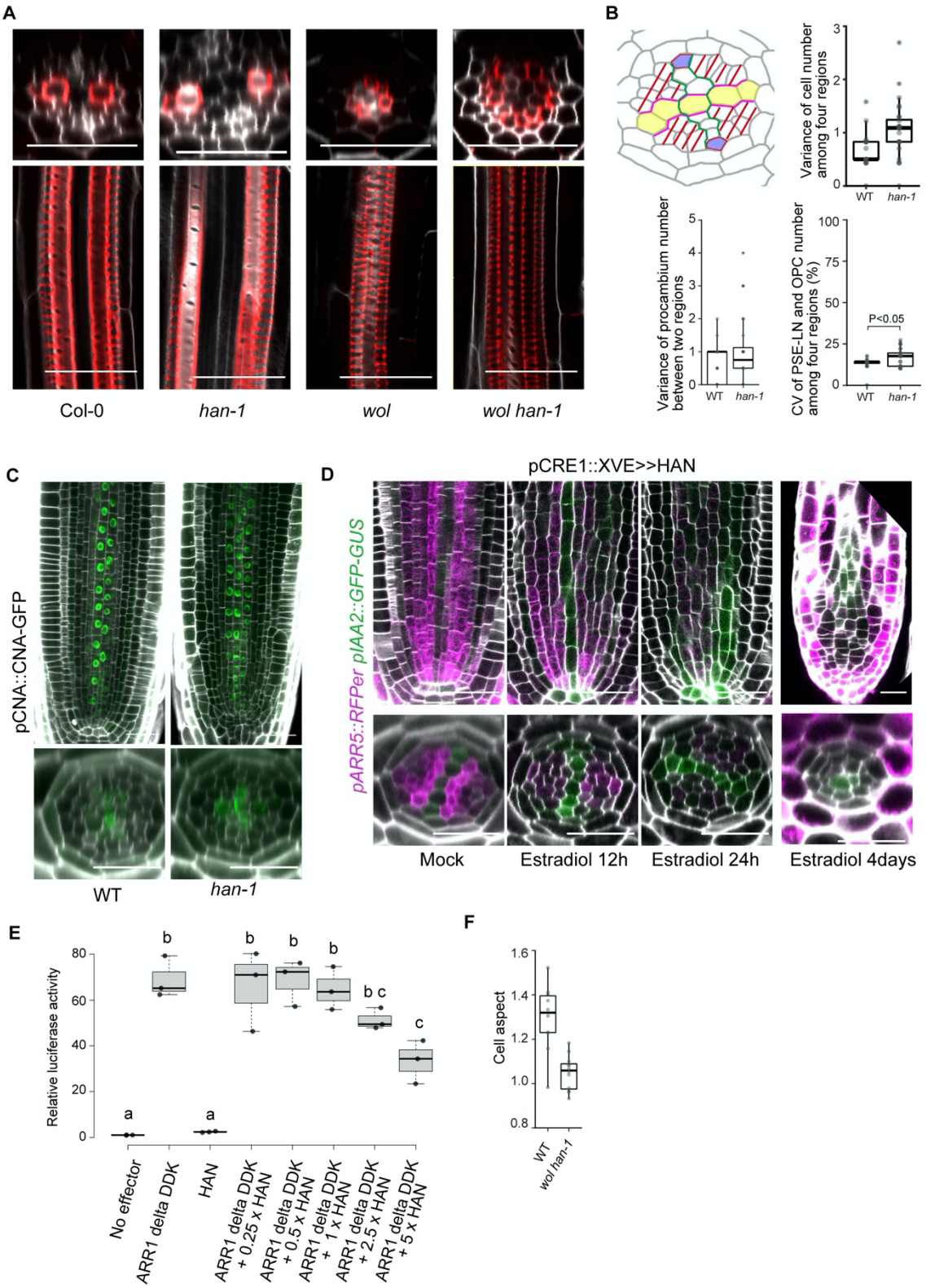

Fig. S3.4. Supporting material for Fig. 3.4

(A) Fuchsin-stained xylem (red) of wild-type, han-1, wol and wol han-1.

(B) The variance of procambium number between two regions separated by the XP boundary (left bottom panel), the variance of cell number (right top panel) and the coefficient of variation (CV, i.e, variance normalized by the mean) of PSE-LN and OPC cell number (right bottom panel) among four regions separated by the XP boundary and PSE-PSE cell files (red stripe) in wild-type (n=xx) and han-1 mutants (n=xx). t-test was performed after confirming a normal distribution by Kolmogorov-Smirnov tests.

(C) HD-ZIP III genes, CNA expression.

(D) Temporal processing with estradiol.

(E) The relative luciferase activity.

(F) Cell aspect ratio at central cells in wildtype (n=10) and *wol han-1* mutant (n=12).

The samples of *in vivo* root in A, C, D were prepared and imaged by S. Miyashima

4. General conclusion

To understand the developmental systems that realize the reproducible organ shape under less fluid plant tissue, I investigated root tip shape and vascular bundle formation. At root tip shape in Chapter 2, I identified the sharp division gradient at both root ends and directional cell division at root center form a catenary-shaped root tip through the directional and uniform forces corresponding to a catenary chain. At vascular bundle formation in Chapter 3, I identified the distal and symmetric localized proliferation to the boundary forms a symmetrically smooth tissue boundary through compression to the boundary. Therefore, spatial regulations of cell division and elongation for anisotropic tissue growth are mechanically suitable for forming the organ under less fluid tissue.

Moreover, I achieved highly quantitative consistency between mathematical modeling and plant experiments at the cellular level of accuracy. I predicted the mechanical properties in the organ by quantifying the plant organ shapes and cell behavior (i.e., cell division and elongation) and the mechanical stress in the mathematical model. Then, the corresponding mechanics led me to find the tissue growth rules that form the reproducible organ shapes. This established research approach will lead us to discover essential tissue growth and its mechanics for other plant and animal organogenesis.

Acknowledgements

I would like to thank Associate Prof. K. Fujimoto for instruction and discussion. I also deeply thank Drs. T. Goh, S. Miyashima, S. Tsugawa, K. Matsushita, H. Fukaki, K. Nakazima for their generous cooperation. I am grateful to Drs. T. Kakimoto, S. Takagi, K. Matsuno for advices and comments. I also would like to thank Drs. M. Kitazawa, H. Oda, members of Fujimoto lab. for valuable comments; Drs. H. Iida, T. Kakimoto, A. Tsuboi, D. Mashiko for technical support.

References

Abzhanov, A. (2017). The old and new faces of morphology: the legacy of D'Arcy Thompson's 'theory of transformations' and 'laws of growth'. *Development* 144, 4284-4297.

Aigouy, B., Farhadifar, R., Staple, D. B., Sagner, A., Röper, J.-C., Jülicher, F. and Eaton, S. (2010). Cell Flow Reorients the Axis of Planar Polarity in the Wing Epithelium of Drosophila. *Cell* 142, 773-786.

Akaike, H. (1974). A new look at the statistical model identification. *IEEE Trans Automat Contr* 19, 716-723.

Aliee, M., Röper, J.-C., Landsberg, K. P., Pentzold, C., Widmann, T. J., Jülicher, F. and Dahmann, C. (2012). Physical Mechanisms Shaping the Drosophila Dorsoventral Compartment Boundary. *Current Biology* 22, 967–976.

Arsuffi, G. and Braybrook, S. A. (2018). Acid growth: an ongoing trip. *Journal of Experimental Botany* 69, 137–146.

Barbez, E., Dünser, K., Gaidora, A., Lendl, T. and Busch, W. (2017). Auxin steers root cell expansion via apoplastic pH regulation in Arabidopsis thaliana. *PNAS* 114, E4884–E4893.

Bassel, G. W., Stamm, P., Mosca, G., Barbier de Reuille, P., Gibbs, D. J., Winter, R., Janka, A., Holdsworth, M. J. and Smith, R. S. (2014). Mechanical constraints imposed by 3D cellular geometry and arrangement modulate growth patterns in the Arabidopsis embryo. *Proc Natl Acad Sci USA* 111, 8685-8690.

Block, P., DeJong, M. and Ochsendorf, J. (2006). As Hangs the Flexible Line: Equilibrium of Masonry Arches. *Nexus Netw J* 8, 13-24.

Burnham, K. P., Anderson, D. R. and Burnham, K. P. (2002). *Model selection and multimodel inference : a practical information-theoretic approach* (2nd edn). New York: Springer.

Caggiano, M. P., Yu, X., Bhatia, N., Larsson, A., Ram, H., Ohno, C. K., Sappl, P., Meyerowitz, E. M., Jönsson, H. and Heisler, M. G. (2017). Cell type boundaries organize plant development. *eLife* 6, e27421.

Campas, O., Mallarino, R., Herrel, A., Abzhanov, A. and Brenner, M. P. (2010). Scaling and shear transformations capture beak shape variation in Darwin's finches. *Proc Natl Acad Sci USA* 107, 3356-3360.

Clowes, F. a. L. (2000). Pattern in root meristem development in angiosperms. *New Phytol* 146, 83-94.

Colombi, T., Kirchgessner, N., Walter, A. and Keller, T. (2017). Root Tip Shape Governs Root Elongation Rate under Increased Soil Strength. *Plant Physiol* 174, 2289-2301.

Dahmann, C., Oates, A. C. and Brand, M. (2011). Boundary formation and maintenance in tissue development. *Nat Rev Genet* 12, 43–55.

Darwin, C. (1859). *On the origin of species by means of natural selection, or, The preservation of favoured races in the struggle for life*. London: J. Murray.

De Rybel, B., Adibi, M., Breda, A. S., Wendrich, J. R., Smit, M. E., Novák, O., Yamaguchi, N., Yoshida, S., Van Isterdael, G., Palovaara, J., et al. (2014). Integration of growth and patterning during vascular tissue formation in Arabidopsis. *Science* 345, 1255215.

De Rybel, B., Mähönen, A. P., Helariutta, Y. and Weijers, D. (2016). Plant vascular development: from early specification to differentiation. *Nat Rev Mol Cell Biol* 17, 30–40.

Di Ruocco, G., Di Mambro, R. and Dello Ioio, R. (2018). Building the differences: a case for the ground tissue patterning in plants. *Proc. Royal Soc. B* 285, 20181746.

Esau, K. (1965). *Plant Anatomy*. 2nd Edition. John Wiley, New York.

Elzhov, T. V., Mullen, K. M., Spiess, A.-N. and Bolker, B. (2015). minpack.lm: R Interface to the Levenberg-Marquardt Nonlinear Least-Squares Algorithm Found in MINPACK, Plus Support for Bounds.

Eshel, A. and Beeckman, T. (2013). *Plant roots : the hidden half* (4th edn). Boca Raton, FL: CRC Press.

Farhadifar, R., Röper, J.-C., Aigouy, B., Eaton, S. and Jülicher, F. (2007). The Influence of Cell Mechanics, Cell-Cell Interactions, and Proliferation on Epithelial Packing. *Curr Biol* 17, 2095-2104.

Fritz, J. A., Brancale, J., Tokita, M., Burns, K. J., Hawkins, M. B., Abzhanov, A. and Brenner, M. P. (2014). Shared developmental programme strongly constrains beak shape diversity in songbirds. *Nat Commun* 5, 3700.

Fujiwara, M., Goh, T., Tsugawa, S., Nakajima, K., Fukaki, H. and Fujimoto, K. (2021). Tissue growth constrains root organ outlines into an isometrically scalable shape. *Development* 148,.

Geitmann, A. and Ortega, J. K. (2009). Mechanics and modeling of plant cell growth. *Trends Plant Sci* 14, 467-478.

Goh, T., Toyokura, K., Wells, D. M., Swarup, K., Yamamoto, M., Mimura, T., Weijers, D., Fukaki, H., Laplaze, L., Bennett, M. J., et al. (2016). Quiescent center initiation in the Arabidopsis lateral root primordia is dependent on the SCARECROW transcription factor. *Development* 143, 3363-3371.

Hamamoto, L., Hawes, M. C. and Rost, T. L. (2006). The Production and Release of Living Root Cap Border Cells is a Function of Root Apical Meristem Type in Dicotyledonous Angiosperm Plants. *Ann Bot* 97, 917-923.

Hamant, O., Heisler, M. G., Jonsson, H., Krupinski, P., Uyttewaal, M., Bokov, P., Corson, F., Sahlin, P., Boudaoud, A., Meyerowitz, E. M., et al. (2008). Developmental patterning by mechanical signals in Arabidopsis. *Science* 322, 1650-1655.

Handy, R. L. (1973). The Igloo and the Natural Bridge as Ultimate Structures. *Arctic* 26, 276-281.

Heimsch, C. and Seago Jr, J. L. (2008). Organization of the root apical meristem in angiosperms. *Am J Bot* 95, 1–21.

Heisler, M. G., Hamant, O., Krupinski, P., Uyttewaal, M., Ohno, C., Jönsson, H., Traas, J. and Meyerowitz, E. M. (2010). Alignment between PIN1 Polarity and Microtubule Orientation in the Shoot Apical Meristem Reveals a Tight Coupling between Morphogenesis and Auxin Transport. *PLOS Biology* 8, e1000516.

Hejnowicz, Z. (1984). Trajectories of principal directions of growth, natural coordinate system in growing plant organ. *Acta Soc Bot Pol* 53, 29-42.

Hemmi, N., Akiyama-Oda, Y., Fujimoto, K. and Oda, H. (2018). A quantitative study of the diversity of stripe-forming processes in an arthropod cell-based field undergoing axis formation and growth. *Developmental Biology* 437, 84–104.

Hervieux, N., Tsugawa, S., Fruleux, A., Dumond, M., Routier-Kierzkowska, A. L., Komatsuzaki, T., Boudaoud, A., Larkin, J. C., Smith, R. S., Li, C. B., et al. (2017). Mechanical Shielding of Rapidly Growing Cells Buffers Growth Heterogeneity and Contributes to Organ Shape Reproducibility. *Curr Biol* 27, 3468-3479 e3464.

Heyman, J. (1998). Hooke's cubico–parabolical conoid. *Notes Rec R Soc Lond* 52, 39-50.

Hirota, A., Kato, T., Fukaki, H., Aida, M. and Tasaka, M. (2007). The Auxin-Regulated AP2/EREBP Gene PUCHI Is Required for Morphogenesis in the Early Lateral Root Primordium of Arabidopsis. *Plant Cell* 19, 2156-2168.

Honda, H. (1983). Geometrical models for cells in tissues. *Int Rev Cytol* 81, 191-248.

Hong, L., Dumond, M., Tsugawa, S., Sapala, A., Routier-Kierzkowska, A.-L., Zhou, Y., Chen, C., Kiss, A., Zhu, M., Hamant, O., et al. (2016). Variable Cell Growth Yields Reproducible Organ Development through Spatiotemporal Averaging. *Dev Cell* 38, 15-32.

Hong, L., Dumond, M., Zhu, M., Tsugawa, S., Li, C. B., Boudaoud, A., Hamant, O. and Roeder, A. H. K. (2018). Heterogeneity and Robustness in Plant Morphogenesis: From Cells to Organs. *Annu Rev Plant Biol* 69, 469-495.

Houle, D., Bolstad, G. H., van der Linde, K. and Hansen, T. F. (2017). Mutation predicts 40 million years of fly wing evolution. *Nature* 548, 447-450.

Huang, L. and Schiefelbein, J. (2015). Conserved Gene Expression Programs in Developing Roots from Diverse Plants. *Plant Cell* 27, 2119-2132.

Ishihara, S. and Sugimura, K. (2012). Bayesian inference of force dynamics during morphogenesis. *Journal of Theoretical Biology* 313, 201–211.

Izhaki, A. and Bowman, J. L. (2007). KANADI and Class III HD-Zip Gene Families Regulate Embryo Patterning and Modulate Auxin Flow during Embryogenesis in Arabidopsis. *The Plant Cell* 19, 495–508.

Keller, R., Davidson, L. A. and Shook, D. R. (2003). How we are shaped: The biomechanics of gastrulation. *Differentiation* 71, 171–205.

Kennaway, R., Coen, E., Green, A. and Bangham, A. (2011). Generation of Diverse Biological Forms through Combinatorial Interactions between Tissue Polarity and Growth. *PLOS Computational Biology* 7, e1002071.

Kuchen, E. E., Fox, S., Reuille, P. B. de, Kennaway, R., Bensmihen, S., Avondo, J., Calder, G. M., Southam, P., Robinson, S., Bangham, A., et al. (2012). Generation of Leaf Shape Through Early Patterns of Growth and Tissue Polarity. *Science*.

Kumpf, R. P. and Nowack, M. K. (2015). The root cap: a short story of life and death. *J Exp Bot* 66, 5651-5662.

Kurihara, D., Mizuta, Y., Sato, Y. and Higashiyama, T. (2015). ClearSee: a rapid optical clearing reagent for whole-plant fluorescence imaging. *Development* 142, 4168-4179.

Landsberg, K. P., Farhadifar, R., Ranft, J., Umetsu, D., Widmann, T. J., Bittig, T., Said, A., Jülicher, F. and Dahmann, C. (2009). Increased Cell Bond Tension Governs Cell Sorting at the Drosophila Anteroposterior Compartment Boundary. *Current Biology* 19, 1950–1955.

Lavenus, J., Goh, T., Guyomarc'h, S., Hill, K., Lucas, M., Voss, U., Kenobi, K., Wilson, M. H., Farcot, E., Hagen, G., et al. (2015). Inference of the Arabidopsis lateral root gene regulatory network suggests a bifurcation mechanism that defines primordia flanking and central zones. *Plant Cell* 27, 1368-1388.

Lavenus, J., Goh, T., Roberts, I., Guyomarc'h, S., Lucas, M., De Smet, I., Fukaki, H., Beeckman, T., Bennett, M. and Laplaze, L. (2013). Lateral root development in Arabidopsis: fifty shades of auxin. *Trends Plant Sci* 18, 450-458.

Le Roy, C., Debat, V. and Llaurens, V. (2019). Adaptive evolution of butterfly wing shape: from morphology to behaviour. *Biol Rev Camb Philos Soc* 94, 1261-1281.

Lecuit, T. and Lenne, P.-F. (2007). Cell surface mechanics and the control of cell shape, tissue patterns and morphogenesis. *Nat Rev Mol Cell Biol* 8, 633–644.

Lee, S.-W. and Morishita, Y. (2017). Possible roles of mechanical cell elimination intrinsic to growing tissues from the perspective of tissue growth efficiency and homeostasis. *PLOS Computational Biology* 13, e1005651.

Leiboff, S., DeAllie, C. K. and Scanlon, M. J. (2016). Modeling the Morphometric Evolution of the Maize Shoot Apical Meristem. *Front Plant Sci* 7, 1651.

Leiboff, S., Li, X., Hu, H. C., Todt, N., Yang, J., Li, X., Yu, X., Muehlbauer, G. J., Timmermans, M. C., Yu, J., et al. (2015). Genetic control of morphometric diversity in the maize shoot apical meristem. *Nat Commun* 6, 8974.

Lockhart, J. A. (1965). An analysis of irreversible plant cell elongation. *J Theor Biol* 8, 264-275.

Lockwood, E. H. (1961). *Book of Curves*. Cambridge: Cambridge University Press.

Love, A. E. H. (1927). *A Treatise on the Mathematical Theory of Elasticity.* Cambridge University Press.

Lucas, M., Kenobi, K., Wangenheim, D. v., Voβ, U., Swarup, K., Smet, I. D., Damme, D. V., Lawrence, T., Péret, B., Moscardi, E., et al. (2013). Lateral root morphogenesis is dependent on the mechanical properties of the overlaying tissues. *Proc Natl Acad Sci USA* 110, 5229-5234.

Mähönen, A. P., Bonke, M., Kauppinen, L., Riikonen, M., Benfey, P. N. and Helariutta, Y. (2000). A novel two-component hybrid molecule regulates vascular morphogenesis of the Arabidopsis root. *Genes Dev.* 14, 2938–2943.

Mähönen, A. P., Higuchi, M., Törmäkangas, K., Miyawaki, K., Pischke, M. S., Sussman, M. R., Helariutta, Y. and Kakimoto, T. (2006). Cytokinins Regulate a Bidirectional Phosphorelay Network in Arabidopsis. *Current Biology* 16, 1116–1122.

Maugarny-Cales, A. and Laufs, P. (2018). Getting leaves into shape: a molecular, cellular, environmental and evolutionary view. *Development* 145, dev161646.

Mellor, N., Vaughan-Hirsch, J., Kümpers, B. M. C., Help-Rinta-Rahko, H., Miyashima, S., Mähönen, A. P., Campilho, A., King, J. R. and Bishopp, A. (2019). A core mechanism for specifying root vascular patterning can replicate the anatomical variation seen in diverse plant species. *Development* 146, dev172411.

Mishra, A. K., Tramacere, F., Guarino, R., Pugno, N. M. and Mazzolai, B. (2018). A study on plant root apex morphology as a model for soft robots moving in soil. *PLOS ONE* 13, e0197411.

Miyashima, S., Roszak, P., Sevilem, I., Toyokura, K., Blob, B., Heo, J., Mellor, N., Help-Rinta-Rahko, H., Otero, S., Smet, W., et al. (2019). Mobile PEAR transcription factors integrate positional cues to prime cambial growth. *Nature* 565, 490–494.

Moré, J. J. (1978). The Levenberg-Marquardt algorithm: Implementation and theory. (ed G. A. Watson), pp. 105-116: Springer.

Müller, B. and Sheen, J. (2008). Cytokinin and auxin interaction in root stem-cell specification during early embryogenesis. *Nature* 453, 1094–1097.

Musielak, T. J., Schenkel, L., Kolb, M., Henschen, A. and Bayer, M. (2015). A simple and versatile cell wall staining protocol to study plant reproduction. *Plant Reproduction* 28, 161-169.

Nakielski, J. and Lipowczan, M. (2013). Spatial and Directional Variation of Growth Rates in Arabidopsis Root Apex: A Modelling Study. *PLOS ONE* 8, e84337.

Niklas, K. J. (1994). *Plant allometry : the scaling of form and process*. Chicago: University of Chicago Press.

Norman, J. M. V., Xuan, W., Beeckman, T. and Benfey, P. N. (2013). To branch or not to branch: the role of pre-patterning in lateral root formation. *Development* 140, 4301-4310.

Oikawa, K., Matsunaga, S., Mano, S., Kondo, M., Yamada, K., Hayashi, M., Kagawa, T., Kadota, A., Sakamoto, W., Higashi, S., et al. (2015). Physical interaction between peroxisomes and chloroplasts elucidated by in situ laser analysis. *Nature Plants* 1, 1–12.

Okada, K. and Shimura, Y. (1992). Mutational Analysis of Root Gravitropism and Phototropism of Arabidopsis thaliana Seedlings. *Functional Plant Biology* 19, 439-448.

Ortega, J. K. (1985). Augmented growth equation for cell wall expansion. *Plant Physiol* 79, 318-320.

Péret, B., De Rybel, B., Casimiro, I., Benková, E., Swarup, R., Laplaze, L., Beeckman, T. and Bennett, M. J. (2009). Arabidopsis lateral root development: an emerging story. *Trends in Plant Science* 14, 399–408.

Petricka, J. J., Winter, C. M. and Benfey, P. N. (2012). Control of Arabidopsis Root Development. *Annu Rev Plant Biol* 63, 563-590.

Roue, J., Chauvet, H., Brunel-Michac, N., Bizet, F., Moulia, B., Badel, E. and Legue, V. (2020). Root cap size and shape influence responses to the physical strength of the growth medium in Arabidopsis thaliana primary roots. *J Exp Bot* 71, 126-137.

Rudolf, K., Umetsu, D., Aliee, M., Sui, L., Jülicher, F. and Dahmann, C. (2015). A local difference in Hedgehog signal transduction increases mechanical cell bond tension and biases cell intercalations along the Drosophila anteroposterior compartment boundary. *Development* 142, 3845–3858.

Sakamoto, Y., Ishiguro, M. and Kitagawa, G. (1986). *Akaike information criterion statistics*. Tokyo; Dordrecht; Boston; Hingham, MA: KTK Scientific Publishers ; D. Reidel ; Sold and distributed in the U.S.A. and Canada by Kluwer Academic Publishers.

Salcedo, M. K., Hoffmann, J., Donoughe, S. and Mahadevan, L. (2019). Computational analysis of size, shape and structure of insect wings. *Biol Open* 8, bio040774.

Schmidt-Nielsen, K. (1984). *Scaling, why is animal size so important?* Cambridge ; New York: Cambridge University Press.

Smetana, O., Mäkilä, R., Lyu, M., Amiryousefi, A., Sánchez Rodríguez, F., Wu, M.-F., Solé-Gil, A., Leal Gavarrón, M., Siligato, R., Miyashima, S., et al. (2019). High levels of auxin signalling define the stem-cell organizer of the vascular cambium. *Nature* 565, 485–489.

Sugimura, K., Lenne, P.-F. and Graner, F. (2016). Measuring forces and stresses in situ in living tissues. *Development* 143, 186–196.

Szymanowska-Pułka, J., Potocka, I., Karczewski, J., Jiang, K., Nakielski, J. and Feldman, L. J. (2012). Principal growth directions in development of the lateral root in Arabidopsis thaliana. *Ann Bot* 110, 491-501.

ten Hove, C. A., Lu, K.-J. and Weijers, D. (2015). Building a plant: cell fate specification in the early Arabidopsis embryo. *Development* 142, 420-430.

Thompson, D. A. W. (1917). *On Growth and Form*: Cambridge University Press.

Timoshenko, S. P. and Gere, J. M. (1961). *Theory of Elastic Stability*: McGraw-Hill.

Torres-Martinez, H. H., Rodriguez-Alonso, G., Shishkova, S. and Dubrovsky, J. G. (2019). Lateral Root Primordium Morphogenesis in Angiosperms. *Front Plant Sci* 10, 206.

Trinh, D.-C., Lavenus, J., Goh, T., Boutté, Y., Drogue, Q., Vaissayre, V., Tellier, F., Lucas, M., Voß, U., Gantet, P., et al. (2019). PUCHI regulates very long chain fatty acid biosynthesis during lateral root and callus formation. *Proc Natl Acad Sci USA* 116, 14325-14330.

Trinh, D.-C., Alonso-Serra, J., Asaoka, M., Colin, L., Cortes, M., Malivert, A., Takatani, S., Zhao, F., Traas, J., Trehin, C., et al. (2021). How Mechanical Forces Shape Plant Organs. *Current Biology* 31, R143–R159.

Tsukaya, H. (2018). Leaf shape diversity with an emphasis on leaf contour variation, developmental background, and adaptation. *Semin Cell Dev Biol* 79, 48-57.

Umetsu, D., Aigouy, B., Aliee, M., Sui, L., Eaton, S., Jülicher, F. and Dahmann, C. (2014). Local Increases in Mechanical Tension Shape Compartment Boundaries by Biasing Cell Intercalations. *Current Biology* 24, 1798–1805.

Uyttewaal, M., Burian, A., Alim, K., Landrein, B., Borowska-Wykret, D., Dedieu, A., Peaucelle, A., Ludynia, M., Traas, J., Boudaoud, A., et al. (2012). Mechanical stress acts via katanin

to amplify differences in growth rate between adjacent cells in Arabidopsis. *Cell* 149, 439-451.

Van Damme, D., Rybel, B. D., Gudesblat, G., Demidov, D., Grunewald, W., Smet, I. D., Houben, A., Beeckman, T. and Russinova, E. (2011). Arabidopsis α Aurora Kinases Function in Formative Cell Division Plane Orientation. *Plant Cell* 23, 4013-4024.

Verger, S., Long, Y., Boudaoud, A. and Hamant, O. (2018). A tension-adhesion feedback loop in plant epidermis. *eLife* 7, e34460.

Vermeer, J. E. M., Wangenheim, D. v., Barberon, M., Lee, Y., Stelzer, E. H. K., Maizel, A. and Geldner, N. (2014). A Spatial Accommodation by Neighboring Cells Is Required for Organ Initiation in Arabidopsis. *Science* 343, 178-183.

Vilches Barro, A., Stöckle, D., Thellmann, M., Ruiz-Duarte, P., Bald, L., Louveaux, M., von Born, P., Denninger, P., Goh, T., Fukaki, H., et al. (2019). Cytoskeleton Dynamics Are Necessary for Early Events of Lateral Root Initiation in Arabidopsis. *Current Biology* 29, 2443-2454.e5.

von Wangenheim, D., Fangerau, J., Schmitz, A., Smith, R. S., Leitte, H., Stelzer, E. H. K. and Maizel, A. (2016). Rules and Self-Organizing Properties of Post-embryonic Plant Organ Cell Division Patterns. *Curr Biol* 26, 439-449.

Wang, X. and Clarke, J. A. (2015). The evolution of avian wing shape and previously unrecognized trends in covert feathering. *Proc Biol Sci* 282, 20151935.

Whitewoods, C. D. and Coen, E. (2017). Growth and Development of Three-Dimensional Plant Form. *Current Biology* 27, R910–R918.

Wilson, M., Goh, T., Voß, U., Bishopp, A., Péret, B. and Bennett, M. (2013). SnapShot: Root Development. *Cell* 155, 1190-1190.e1.

Ye, L., Wang, X., Lyu, M., Siligato, R., Eswaran, G., Vainio, L., Blomster, T., Zhang, J. and Mähönen, A. P. (2021). Cytokinins initiate secondary growth in the Arabidopsis root through a set of LBD genes. *Current Biology* 31, 3365-3373.e7.

Zhao, Y., Medrano, L., Ohashi, K., Fletcher, J. C., Yu, H., Sakai, H. and Meyerowitz, E. M. (2004). HANABA TARANU Is a GATA Transcription Factor That Regulates Shoot Apical Meristem and Flower Development in Arabidopsis[W]. *The Plant Cell* 16, 2586–2600.